Coherence effects and spectroscopy in laser driven dense atomic vapour

Dissertation

zur

Erlangung des Doktorgrades (Dr. rer. nat.)

der

Mathematisch-Naturwissenschaftlichen Fakultät

der

Rheinischen Friedrich-Wilhelms-Universität Bonn

vorgelegt von

Vladimir Đokić

aus

Kruševac (Serbien)

Bonn, October 2015

Angefertigt mit Genehmigung der Mathematisch-Naturwissenschaftlichen Fakultät der Rheinischen Friedrich-Wilhelms-Universität Bonn

1. Gutachter: Prof. Dr. M. Weitz
2. Gutachter: Prof. Dr. S. Linden

Tag der Promotion: 21. Januar 2016
Erscheinungsjahr: 2016

Diese Dissertation ist elektronisch publiziert auf dem Hochschulschriftenserver der ULB Bonn: `http://hss.ulb.uni-bonn.de/diss_online`

Majci

Abstract

In this work quantum coherence effects in dense rubidium atomic vapour are investigated. Prepared in a laser driven atomic system, coherent effects, like the well-known electromagnetically induced transparency, have a remarkable ability to significantly alter optical properties of the used medium. Electromagnetically induced transparency and related phenomena like slow and stored light can be explained in terms of dark state polaritons, representing quasiparticles consisting of light and matter components. In this thesis, experiments aiming to the concept of quasiparticles are described.

Furthermore, in this thesis the concept of resonance retrieval of a stored coherence is investigated, a concept that might prove useful in metrology.

In this thesis, the focus is set on the experimental study of the particle-like nature of dark state polaritons. Therefore, a radiofrequency spectroscopy is performed on stationary and moving polaritons with an internal level structure. To this end, an experimental setup is described that allows for the existence of two state dark polaritons in a tripod level scheme. The internal level structure of these polaritons is then probed by a radiofrequency field and a transfer of population between two dark states is observed. The measured population transfer, though with a limited contrast, strongly indicates that dark state polaritons can be considered as quasiparticles with an internal level structure.

Since the dark state polaritons exhibit features of an effective magnetic dipole moment, the existence of the Aharonov-Casher phase effect for these quasiparticles is investigated experimentally. It is predicted by a known Aharonov-Casher effect that taking two particles with a finite magnetic dipole moment around a line of charge causes an accumulated phase difference between them. In this work, a detection system with a phase sensitivity of 10^{-5} rad is described, which sets the upper boundary on the experimentally detectable Aharonov-Casher phase for the hot rubidium gas system.

In the last part of this thesis experiments on storage and resonant retrieval of an atomic coherence are described. To this end, an RF field creates an atomic coherence which is stored and subsequently read out with an optical field. The retrieved field is shown to be frequency locked to the optical field. The difference frequency is, within the limits of experimental sensitivity, at the atomic resonance frequency independently on the amplitude and frequency variations of the radiofrequency excitation field.

Parts of this thesis have been published in the following paper:

- V. Djokic, G. Enzian, F. Vewinger and M. Weitz, *Resonance retrieval of stored coherence in an rf-optical double resonance experiment*, Phys. Rev. A **92**, 063802 (2015)

Acknowledgements

First of all, I would like to thank Prof. Dr. Martin Weitz for the given opportunity to work on my PhD thesis in his research group. Special thanks goes to Dr. Frank Vewinger. Without his support this work would not be possible. Vielen Dank to Dr. Anne Saß. She has been nothing but a good colleague and a great friend since my first days in Bonn. To my friend, Dr. Stavros Christopoulos, efcharistó polí for his generous support and long discussions.

I would also like to extend my thanks to all the members of the Quantum Optics group for creating a friendly working environment. Special thanks go to the master and the bachelor students that contributed to my work, Georg Enzian, Stephan Hüwe, and Lukas Sitta. It was a pleasure to work with them. Ich bedanke mich ganz herzlich to all staff members of the Institute for Applied Physics, Ilona Jaschke, Fien Latumahina, Dietmar Haubrich, and Annelise von Rudloff-Miglo, as well as to all members of the mechanical and electrical workshop. I am grateful to Anne Saß, Stavros Chirstopoulos, and Christopher Grossert, who proofread my thesis.

Of course, I would like to express my gratitude to my whole family and my friends for their constant support in the past years. Also, I'd like to thank my previous professors Dragana Milićević and Branislav Jelenković and his Photonics group in the Institute of Physics in Zemun. Without their help I wouldn't be here today. Veliko hvala svima na ogromnoj podršci tokom svih mojih studija.

Contents

1 Introduction

Quantum coherence effects, the main subject of this thesis, have been a topic of intense scientific research in the past decades. Induced by light-matter interactions, these coherent effects have a remarkable capability of being able to alter optical properties of atomic media. A real milestone, not only in the investigation of the coherent effects, but also in scientific research in general and above all in our everyday lives, represents the invention of the laser [1], as a coherent source of optical radiation. The laser invention provoked a modified theory of the quantum nature of light [2], confirmed up to this day in a series of remarkable experiments [3,4]. The previous decades have seen enormous improvements in the field of metrology, where by laser spectroscopy of atomic media one could determine the relative position of atomic energy levels with unprecedented precision [5, 6]. Recent impressive examples of improvements in metrology techniques represent high-precision measurements of the frequency of light [7] or a newly developed superradiant laser [8] with a potential application in the measurement of gravitational waves and fundamental constants. Another important landmark was the development of laser cooling techniques of atoms [9–11], allowing for the creation of Bose-Einstein condensates [12, 13] and for major improvements in the field of atomic clocks [14]. Whether it is the creation of squeezed light [15], of entangled photons [16] or of a Bose-Einstein condensation of photons [17], an astonishing world of light induced effects never stops to amaze us.

A huge contribution to the development of many research fields gave quantum interference effects, namely coherent population trapping (CPT) [18] and the closely related phenomenon of electromagnetically induced transparency (EIT) [19, 20], capable of making an otherwise opaque medium transparent through the presence of so-called dark states. For example, dark states played a well known role in the development of laser cooling techniques for atoms, with the technique of velocity selective coherent population trapping [11], allowing for first experiments achieving laser cooling below the atomic recoil temperature. Also, the fields of nonlinear optics [21, 22] and atomic interferometry [23] have benefited from dark states techniques. Other applications of dark states include optical propagation effects in media, an effect well described in terms of electromagnetically induced transparency. In parallel to a strong reduction of the absorption near an atomic resonance, is the existence of a spectrally very steep dispersion, followed at the same time by a rise of the nonlinear susceptibility [24]. Moreover, due to the modified dispersion, the group velocity of a light pulse can be significantly lowered compared to the vacuum speed of light, an effect well described by the term "slow light" [25], which is used for instance in quantum communication protocols [26]. A comprehensive review of the properties of these optical coherence effects in media can be found in [27].

Of crucial importance in many fields, e.g. in quantum information, is the ability to coherently manipulate atomic states and retrieve previously mapped photon states. EIT and CPT effects are widely used tools that allow for reversible storage of light in atomic ensembles [28, 29], where stored photonic information can be controlled in a coherent manner [30]. Based on the EIT effect, it has been reported that non-classical states of light, like squeezed and single-photon states, or entangled photons can be reversibly stored in atomic ensembles [31–34]. Application of EIT in quantum devices and generation

of photonic qubits has also been proposed [35, 36], as well as the use of EIT in quantum teleportation between light and matter [37]. Besides the EIT phenomenon, many different storage techniques have been suggested, such as off-resonant Raman interaction [38] or gradient echo memories [39] schemes in both gaseous atomic samples [40, 41] and in ion-doped crystals [42].

The possibility to prepare narrow resonances using EIT [43, 44] makes it a valuable tool for magnetometry [45–47] and optical clocks. State-of-the-art magnetometry that surpasses the precision of superconducting quantum interference devices (SQUIDs) has been reported [48]. Of further interest is the application of coherent population trapping in the measurement of the frequency difference between two hyperfine atomic states allowing for miniature atomic clocks [49, 50]. While many experiments use continuous signal read out, other work has used free spin precessing for atomic magnetometry, resulting in a Ramsey-like scheme [51].

Since the slow light and storage of light effects can be explained in the formalism of dark state polaritons (DSPs) that show bosonic commutation relations, a realization of Bose-Einstein condensate for dark state polaritons was proposed [52, 53].

Very interesting theoretical considerations show that the propagation of the DSPs can be seen as a motion of Dirac particles with a tunable effective mass [54, 55]. It was shown by Leon Karpa that dark state polaritons possess an effective magnetic dipole moment [56]. In his previous work, Karpa also demonstrated a resonance retrieval of stored optical fields at an atomic transition frequency [57].

This thesis investigates quantum coherence effects, like electromagnetically induced transparency and related slow and storage of light effects, which arise from coherently prepared atomic ground state superpositions in hot atomic rubidium vapour. Considered in terms of dark state polaritons (DSPs), these coherence effects show a particle-like nature. Studying this quasiparticle concept is one of the main goals of this thesis. Furthermore, a resonant retrieval of a stored atomic coherence is investigated in an optical-radiofrequency double resonance experiment.

The thesis is arranged as follows. In chapter 2, a general theoretical introduction on the effects of electromagnetically induced transparency in the formalism of dark state polaritons is presented. Also, the operational principle of optical-radiofrequency double resonance spectroscopy is given.

The following third chapter gives an overview of the basic properties of the used experimental setup and calibration measurements. In the calibration measurements, the experimentally observed EIT effects, which underline the work performed in this thesis, are going to be presented. The EIT resonances in different atomic configurations and their limiting factors are discussed. Measurements of closely related effects of slow/stopped light are also shown.

Spectroscopic measurements on the internal states of dark state quasiparticles, investigating a matter-like nature of polariton systems, are discussed in chapter 4. The preparation of multilevel dark state polaritons in a tripod level scheme and their probing by radiofrequency (RF) field is described. Measurements of RF spectroscopy on both stationary and moving DSP are presented and compared with calculations.

In the next chapter, the study of particle-like properties of the DSP will be continued by searching for an experimental evidence on the existence of Aharonov-Casher effect for DSPs. A brief overview of the existing theoretical considerations for the Aharonov-Casher effect for DSPs is given and a current state of the experiment is discussed.

The sixth chapter describes a demonstration of resonance retrieval of an atomic coherence in an optical-radiofrequency double resonance experiment. An experimental and theoretical results show that after the retrieval of stored coherence, a beating that corresponds to the atomic eigenfrequency is observed. The detected beat frequency is, within the limits of the reached experimental uncertainty, insensitive to the amplitude and frequency variations of the driving RF field, making it a possible candidate for precision measurements.

This thesis is concluded by an outlook in chapter 7 discussing future prospects of the experimental setup.

2 Theoretical Background

A general theoretical overview of the most relevant phenomena is given in this section. Starting with a three-level Λ-interaction scheme, a concept of electromagnetically induced transparency and dark states is introduced. A formalism of dark state polaritons is widely used in this thesis and consequently, it's basic properties are discussed here. After that, a semi-classical model is described, which is used for all later theoretical considerations of a laser driven atomic system. An optical-radiofrequency double resonance spectroscopy, used in chapter 6, is also explained.

2.1 Dark state in a three-level Λ-scheme

When an atomic system with a Λ - configuration level scheme (Fig. 2.1) interacts with coherent optical fields, several physical phenomena can occur. Namely, a creation of a coherent superposition of the lower states of the three-level system can lead to a coherent population trapping (CPT) [58] if the allowed optical transitions interfere destructively. It follows that the entire population of the system remains trapped in the coherent superposition state despite the presence of the optical driving fields [59]. A closely related effect to CPT is electromagnetically induced transparency (EIT) [19], where no initial preparation of the coherent state is needed and a coherent non-absorbing dark state is created by a combination of strong and weak optical coupling fields. The basic features of the EIT phenomenon can be understood by considering the simple three-state model (shown in Fig. 2.1) interacting with optical control and signal fields in the dressed-state formalism [60].

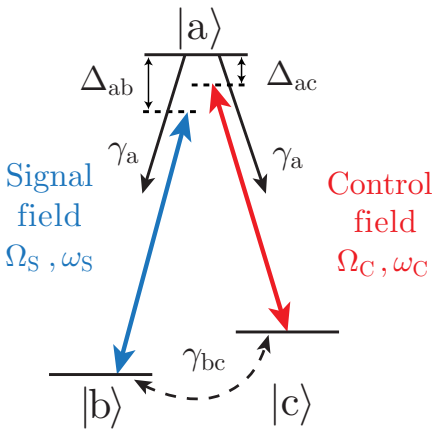

Figure 2.1: Simplified three-level scheme with two ground states $|b\rangle$ and $|c\rangle$ and one excited state $|a\rangle$. Optical signal field with Rabi frequency Ω_S couples the states $|b\rangle$ and $|a\rangle$, whereas optical control field with Rabi frequency Ω_C connects the states $|c\rangle$ and $|a\rangle$. Δ_{ab} and Δ_{ac} represent detuning of signal and control field. The relaxation rates of the excited state and the ground state are denoted by γ_a and γ_{bc}, respectively.

The derivation of the Hamiltonian for the three-level system, with the rotating wave approximation (RWA) implemented for the optical couplings, is presented in Appendix A and here only the final result is given as:

$$H = \frac{\hbar}{2}\begin{pmatrix} 0 & \Omega_{\mathrm{S}} & \Omega_{\mathrm{C}} \\ \Omega_{\mathrm{S}} & 2\Delta_{\mathrm{ab}} & 0 \\ \Omega_{\mathrm{C}} & 0 & 2\Delta_{\mathrm{ac}} \end{pmatrix}, \tag{2.1}$$

where Ω_{C}, Δ_{ac} and Ω_{S}, Δ_{ab} represent the Rabi frequencies and one-photon detunings of the optical strong control field and optical weak signal field, respectively. The one-photon detunings are defined as $\Delta_{\mathrm{ab}} = \omega_{\mathrm{ab}} - \omega_{\mathrm{S}}$ and $\Delta_{\mathrm{ac}} = \omega_{\mathrm{ac}} - \omega_{\mathrm{C}}$, with ω_{S} and ω_{C} being the frequencies of optical signal and control fields. Solving the eigenproblem of the dressed-system reveals an eigenstate of an eigenvalue zero that is of a particular interest for the discussion. Here, it can be expressed as a superposition of the ground states $|\mathrm{b}\rangle$ and $|\mathrm{c}\rangle$ in the following way:

$$|\psi_{\mathrm{D}}\rangle = \cos(\theta)|\mathrm{b}\rangle - \sin(\theta)|\mathrm{c}\rangle \tag{2.2}$$

with the mixing angle θ given as $\tan(\theta) = \Omega_{\mathrm{S}}/\Omega_{\mathrm{C}}$. Since there is no contribution of the excited state $|\mathrm{a}\rangle$ in Eq. (2.2), this eigenstate is also called a *dark state*. In the ideal case, atoms in the dark state do not absorb any optical radiation. When arranging the optical Rabi frequencies in such a way that $\Omega_{\mathrm{C}} = \Omega_{\mathrm{S}}$, one obtains a dark state of the form $|\psi_{\mathrm{D}}\rangle = \frac{1}{\sqrt{2}}(|\mathrm{b}\rangle - |\mathrm{c}\rangle)$.

The behavior of the atomic ensemble, when probed by the signal field, can be expressed by linear susceptibility [27] for $\Delta_{\mathrm{ac}} = 0$ as:

$$\chi(\Delta_{\mathrm{ab}}) = \frac{2g^2N}{\omega_{\mathrm{ab}}}\frac{i\gamma_{\mathrm{bc}} + 2\Delta_{ab}}{\Omega_{\mathrm{C}}^2 + (\gamma_{\mathrm{bc}} + 2i\Delta_{\mathrm{ab}})(\gamma_{\mathrm{a}} + 2i\Delta_{\mathrm{ab}})} \tag{2.3}$$

where N is the total number of atoms, γ_{a} is the population decay rate of the state $|\mathrm{a}\rangle$, γ_{bc} the decoherence rate between the states $|\mathrm{b}\rangle$ and $|\mathrm{c}\rangle$, and ω_{ab} is the transition frequency between the states $|\mathrm{a}\rangle$ and $|\mathrm{b}\rangle$. The atom-signal field coupling constant g is given by $g = \mu_{\mathrm{ab}}\sqrt{\frac{\omega_{\mathrm{ab}}}{\hbar\epsilon_0 \mathrm{V}}}$, where μ_{ab} is the $|\mathrm{a}\rangle - |\mathrm{b}\rangle$ dipole matrix element, ϵ_0 is the permitivity of the system, and V the quantization volume. The susceptibility of the system under EIT conditions ($|\Omega_{\mathrm{C}}|^2 \gg \gamma_{\mathrm{a}}\gamma_{\mathrm{bc}}$, $\gamma_{\mathrm{a}} \gg \gamma_{\mathrm{bc}}$) is shown in Figure 2. The imaginary part of the susceptibility χ (Fig. 2.2(a)) corresponds to the absorption of the medium, while the real part (Fig. 2.2(b)) can be connected with the refractive index $n = \sqrt{1 + Re(\chi)}$ of the signal field. It is evident from Eq. (2.3) that on the atomic transition resonance ($\Delta_{\mathrm{ab}} = 0$) the absorption of the signal field vanishes due to the quantum interference. The existence of the EIT resonance [20] makes the opaque system transparent to the signal field propagation.

Another interesting EIT feature arises due to the behavior of the refractive index when the signal field frequency approaches the atomic transition frequency (Fig. 2.2(b)). A rapid linear change of the refractive index n, in the transparency window close to the atomic resonance, modifies the group velocity at which the signal field propagates through the medium [61, 62]:

$$v_g = \frac{c}{1 + g^2N/|\Omega_{\mathrm{C}}|^2} \tag{2.4}$$

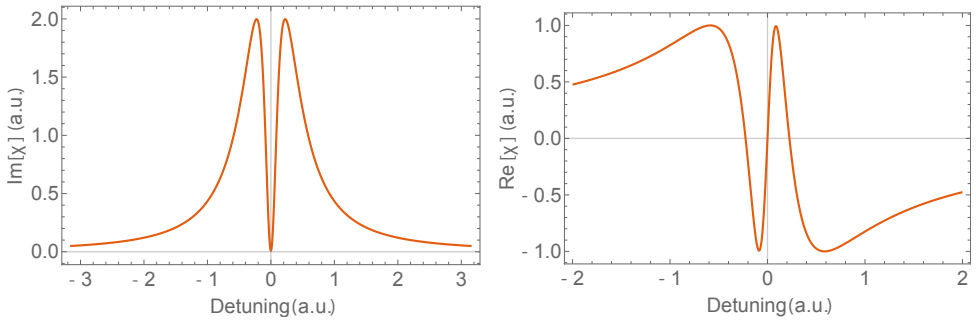

(a) (b)

Figure 2.2: (a) Imaginary part of the susceptibility χ of the system as a function of the detuning under EIT conditions shows the decrease of the absorption on the atomic resonance. (b) Real part of the linear susceptibility χ approaches zero value with the very steep slope as the frequency of the signal field is closer to the atomic resonance. The parameter values used in obtaining the shape of the susceptibility are: $\Omega_{\mathrm{C}} = 0.45$, $\gamma_{\mathrm{bc}} = 0.001$, and $\gamma_{\mathrm{a}} = 1$.

In this way, the group velocity v_g can be significantly reduced, compared to the vacuum speed of light c, by increasing the atomic density N or reducing the Rabi frequency Ω_C of the control field [21, 25]. The effect of lowering the group velocity of the resonant signal pulse to values much smaller than the speed of light is known as slow light effect. On the other hand, the phase velocity v_{ph} of the signal field is at the same time very close to the vacuum speed of light.

2.2 Properties of the Dark State Polaritons

Previously described properties of the EIT phenomenon, such as slow light propagation in the atomic medium, can be considered using the quasiparticle picture [61, 63]. In this approach, form-stable coupled excitations of light and matter are associated with the propagation of the quantum light pulses. Using this formalism the signal field pulse is described by slowly varying quantum operator $\hat{E}_S(z,t)$, whose propagation is given by:

$$\left(\frac{\partial}{\partial t} + c\frac{\partial}{\partial z}\right)\hat{E}_{\mathrm{S}}(z,t) = -\frac{g^2 N}{\Omega_{\mathrm{C}}(t)}\frac{\partial}{\partial t}\frac{\hat{E}_{\mathrm{S}}(z,t)}{\Omega_{\mathrm{C}}(t)}. \tag{2.5}$$

If the decoherence rate γ_{bc} is negligible, one can introduce a coupled superposition $\hat{\Psi}_{\mathrm{D}}(z,t)$ of photonic and spin wave-like excitations, called *dark state polariton* (DSP), and express it as:

$$\hat{\Psi}_{\mathrm{D}}(z,t) = \cos\theta(t)\hat{E}_{\mathrm{S}}(z,t) - \sin\theta(t)\sqrt{N}\hat{\sigma}_{\mathrm{bc}}(z,t). \tag{2.6}$$

where $\hat{\sigma}_{\mathrm{bc}}(z,t)$ is the collective atomic operator describing the quantum properties of the medium, in general expressed as:

$$\hat{\sigma}_{\mu\nu}(z,t) = \frac{1}{N_z}\sum_{j=1}^{N_z} |\mu_j\rangle \langle\nu_j| \, e^{-\omega_{\mu\nu}t}, \tag{2.7}$$

and averaged over small but macroscopic volumes containing $N_z \gg 1$ particles at position z. The mixing between light and matter components is defined here by the mixing angle θ in the following way:

$$\cos\theta(t) = \frac{\Omega_{\mathrm{C}}(t)}{\sqrt{\Omega_{\mathrm{C}}^2(t) + g^2 N}}, \quad \sin\theta(t) = \frac{g\sqrt{N}}{\sqrt{\Omega_{\mathrm{C}}^2(t) + g^2 N}}. \tag{2.8}$$

The dark state polariton $\hat{\Psi}_{\mathrm{D}}(z,t)$ obeys the equation of motion:

$$\left[\frac{\partial}{\partial t} + c\cos^2\theta(t)\frac{\partial}{\partial z}\right]\hat{\Psi}_{\mathrm{D}}(z,t) = 0, \tag{2.9}$$

and is propagating with the group velocity $v_g(t) = c\cos^2\theta(t)$, which can be controlled by the modification of the control field Rabi frequency Ω_{C}. It is notable that the rotation of the mixing angle $\theta(t)$ from 0 to $\pi/2$ can lead to the full stopping of the signal light pulse, making the polariton completely atomic in nature (see Fig. 2.3). Note that for a

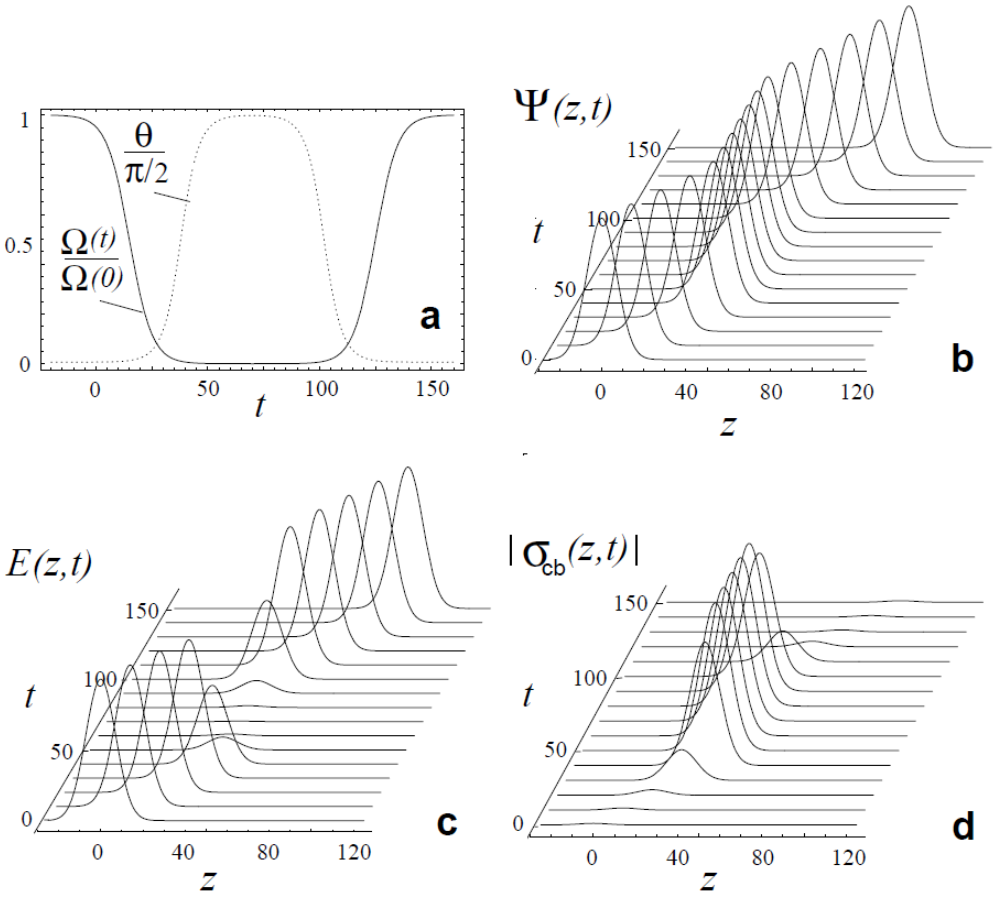

Figure 2.3: Form-stable propagation of dark state polariton (b). Rotation of mixing angle θ for $\pi/2$ (a), induces a transition from light-like (c) to spin wave-like propagation (d) of dark state polariton that at all times preserves its shape. Axes are in arbitrary units with $c = 1$. Figure from [61].

finite value of the control field Rabi frequency, the signal field pulse cannot be completely halted, as in this case the width of the EIT window (see Eq. 2.10) vanishes and the pulse is correspondingly not affected. However, this can be achieved by adiabatical reduction of the control field intensity to zero, with the condition that the spectral width $\Delta\omega_{\mathrm{S}}$ of the signal field pulse obeys the following relation [27]:

$$\Delta\omega_{\mathrm{S}}(t) = \Delta\omega_{\mathrm{S}}(0)\frac{v_g(t)}{v_g(0)}. \tag{2.10}$$

Then, the photonic quantum state can be mapped and stored onto the atomic spin system. The stopped dark state polariton can easily be reaccelerated by turning the control field back on, at the same time coherently retrieving stored quantum state of the signal field pulse [61].

2.3 Semiclassical model

In order to describe an atomic driven system in more detail, a semi-classic model will be adopted, in which the atoms are treated as quantum mechanical particles, while the electromagnetic fields are seen as classical fields. This model will be used throughout this thesis in the theoretical considerations of the system.

The time-domain properties of the quantum mechanical system are conveniently expressed by a density operator ρ. The density operator can be written in a matrix form, which has to be Hermetian ($\rho^*_{nm} = \rho_{nm}$) and normalized ($Tr(\rho) = 1$). The physical meaning of the density matrix can be understood by considering its matrix elements $\rho_{nm} = \langle n|\rho|m\rangle$. The diagonal elements ρ_{nn} represent the probabilities of occupying the states $|n\rangle$ and therefore are referred to as populations. Since the off-diagonal elements ρ_{nm} describe the evolution of the coherent superpositions, they are considered as coherences. The dynamics of the atomic ensemble driven by electromagnetic fields is governed by the Liouville equation:

$$\frac{\partial\rho}{\partial t} = -\frac{i}{\hbar}[H,\rho] - \Gamma\rho, \tag{2.11}$$

where H is the Hamiltonian of the system, for example the Hamiltonian given in Eq. (2.1) for the three-level system. The superoperator Γ incorporates all relaxation rates, which are in this thesis introduced in a phenomenological way.

The equations of motion for the populations and coherences for the optically driven three-level Λ system, shown in Fig. (2.1), can be derived from Eq. 2.11, and after applying a slowly-varying amplitude approximation [59] on the density matrix $\hat{\rho} = \widetilde{\rho}e^{-i\omega t}$, expressed as:

$$\frac{\partial\widetilde{\rho}_{\mathrm{aa}}}{\partial t} = i\Omega_{\mathrm{S}}(\widetilde{\rho}_{\mathrm{ba}} - \widetilde{\rho}_{\mathrm{ab}}) + i\Omega_{\mathrm{C}}(\widetilde{\rho}_{\mathrm{ca}} - \widetilde{\rho}_{\mathrm{ac}}) - 2\gamma_{\mathrm{a}}\widetilde{\rho}_{\mathrm{aa}} \tag{2.12}$$

$$\frac{\partial\widetilde{\rho}_{\mathrm{bb}}}{\partial t} = i\Omega_{\mathrm{S}}(\widetilde{\rho}_{\mathrm{ab}} - \widetilde{\rho}_{\mathrm{ba}}) + \gamma_{\mathrm{a}}\widetilde{\rho}_{\mathrm{aa}} + \gamma_{\mathrm{bc}}(\widetilde{\rho}_{\mathrm{cc}} - \widetilde{\rho}_{\mathrm{bb}}) \tag{2.13}$$

$$\frac{\partial\widetilde{\rho}_{\mathrm{cc}}}{\partial t} = i\Omega_{\mathrm{C}}(\widetilde{\rho}_{\mathrm{ac}} - \widetilde{\rho}_{\mathrm{ca}}) + \gamma_{\mathrm{a}}\widetilde{\rho}_{\mathrm{aa}} + \gamma_{\mathrm{bc}}(\widetilde{\rho}_{\mathrm{bb}} - \widetilde{\rho}_{\mathrm{cc}}) \tag{2.14}$$

$$\frac{\partial\widetilde{\rho}_{\mathrm{ab}}}{\partial t} = -(i\Delta_{\mathrm{ab}} + \gamma_{\mathrm{a}})\widetilde{\rho}_{\mathrm{ab}} + \Omega_{\mathrm{S}}(\widetilde{\rho}_{\mathrm{bb}} - \widetilde{\rho}_{\mathrm{aa}}) + i\Omega_{\mathrm{C}}\widetilde{\rho}_{\mathrm{cb}} \tag{2.15}$$

$$\frac{\partial\widetilde{\rho}_{\mathrm{ac}}}{\partial t} = -(i\Delta_{\mathrm{ac}} + \gamma_{\mathrm{a}})\widetilde{\rho}_{\mathrm{ac}} + i\Omega_{\mathrm{C}}(\widetilde{\rho}_{\mathrm{cc}} - \widetilde{\rho}_{\mathrm{aa}}) - i\Omega_{\mathrm{S}}\widetilde{\rho}_{\mathrm{cb}} \tag{2.16}$$

$$\frac{\partial\widetilde{\rho}_{\mathrm{cb}}}{\partial t} = -(i\delta + \gamma_{\mathrm{bc}})\widetilde{\rho}_{\mathrm{cb}} + i\Omega_{\mathrm{S}}\widetilde{\rho}_{\mathrm{ca}} + i\Omega_{\mathrm{C}}\widetilde{\rho}_{\mathrm{ab}}, \tag{2.17}$$

where δ is a two-photon detuning, defined as $\delta = \Delta_{\mathrm{ac}} - \Delta_{\mathrm{ab}}$. The equations (2.12-2.17) are usually regarded as the optical-Bloch equations for the three-level Λ system and their expanded versions for the six and the eleven-level system are to be used in the theoretical considerations in chapters 4 and 6. The solution of the above system of equations can be found by numerical integration, and the steady-state $\partial_t\widetilde{\rho}_{ij} = 0$, can be found analytically.

Of interest for the action of the atomic medium onto the light fields is the macroscopic polarization P of the atomic medium, which can be expressed as the dipole moment μ of an individual atom averaged over the ensemble per unit volume V:

$$P = \frac{N}{V}\langle\mu\rangle = -e\frac{N}{V}\langle r\rangle\,, \tag{2.18}$$

where $\langle\mu\rangle$ is the dipole moment, e is the electron charge, and r is the electron position operator. Using the density matrix formalism, $\langle\mu\rangle$ can be written as:

$$\langle\mu\rangle = \sum_{n,m}\rho_{nm}a_{nm}, \tag{2.19}$$

defining $a_{nm} = -e\langle m|r|n\rangle$ as the electronic dipole moment of the $|n\rangle \rightarrow |m\rangle$ electronic transition. Now, by inserting Eq. 2.19 into Eq. 2.18, the atomic polarization P for the Λ-system has the following form :

$$P = \frac{N}{\mathrm{V}}\Big[\mu_{\mathrm{ab}}\widetilde{\rho}_{\mathrm{ab}}e^{-i\omega_{\mathrm{S}}t} + \mu_{\mathrm{ac}}\widetilde{\rho}_{\mathrm{ac}}e^{-i\omega_{\mathrm{C}}t}\Big]. \tag{2.20}$$

This expression reveals that the polarization of the medium is proportional to the off-diagonal elements coupled with the dipole moment of the particular electronic transition. This property of the atomic polarization will be used when calculating the response of the medium on a specific optical transition.

2.4 Optical-radiofrequency double resonance technique

A three-level interaction scheme with the two ground levels $|m\rangle$ and $|k\rangle$ and one excited level $|n\rangle$ (Fig. 2.4) is considered. Levels $|m\rangle$ and $|n\rangle$ are coupled via the optical laser field Ω_{C}, effectively transferring the population from one ground state to the other. If the states $|m\rangle$ and $|k\rangle$ are now resonantly coupled with a radiofrequency (RF) field, then the optical laser field and the RF field are simultaneously in resonance with the atomic transitions, which is called optical-RF double resonance technique [64].

Turning on the RF field modifies the absorption of the optical laser beam, which can be monitored in general by detecting the laser-induced fluorescence. This applies equally

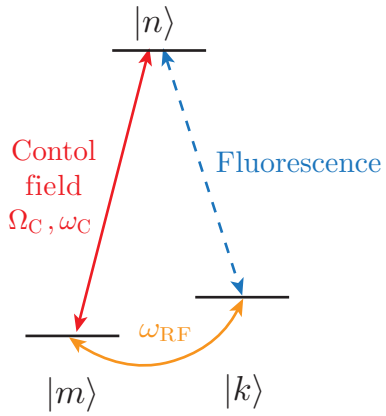

Figure 2.4: Simplified three-level scheme for which an optical-radiofrequency double resonance effect can be realized. The levels $|m\rangle$ and $|n\rangle$ are coupled by control field with the Rabi frequency Ω_C while RF field at frequency ω_{RF} couples the ground levels $|m\rangle$ and $|k\rangle$. The effect can be observed by detecting the fluorescence occurring between the levels $|n\rangle$ and $|k\rangle$.

for a system consisting of one ground and two excited states. The main advantage of the optical-RF double-resonance technique is its high spectral resolution. In the case of a Doppler-broadened optical transition, the optical-RF double-resonance signal is measured at the frequency ω_{RF}, reducing the Doppler-width by a factor $\omega_{\mathrm{RF}}/\omega_{\mathrm{C}}$. When there are no additional broadening mechanisms, the width of the double resonance, for the RF transition between the ground states, is determined by the life time of the corresponding ground levels.

However, this thesis will not focus on the spectroscopic properties of this effect. It will rather be seen from a perspective of an induced two-photon coherences. Simultaneous coupling of the optical and RF transition, creates coherence between the states $|n\rangle$ and $|k\rangle$, that in turn produces coherent optical transition. This coherence will be stored in a process similar to the storage of light and its properties studied for different set of parameters. The three-level scheme presented in Fig. 2.4, can be achieved for the Zeeman sublevels of the electronic states, where the allowed RF transitions are magnetic dipole transitions.

3 Experimental setup and Characterization

In this chapter, the experimental setup used in this work is discussed. The spotlight is set on the general elements used in each experimental investigation. The preparation of the electromagnetic fields and their control is described, as well as the experimental conditions of the medium with which they are interacting. Detailed description of the measurement and detection procedures of each performed experiment is given in their respective chapters.

3.1 Rubidium atomic vapour apparatus

The medium, in which all of the experiments were performed, is a thermal ensemble of atomic rubidium vapour. Rubidium is an element of the alkali metal group, used here with the natural abundance of its isotopes (72.2 % of ^{85}Rb and 27.8 % of ^{87}Rb). Only the D1-line transition in ^{87}Rb between the states $5S_{1/2}$ and $5P_{1/2}$ (see Fig. 3.1) is used experimentally (for more details on ^{87}Rb D1 transition see App. B). On this transition, two different level configurations - Zeeman and hyperfine configuration - allow for the preparation of a simple Λ-like level schemes (Fig. 3.1). The so-called Zeeman configuration uses degenerate Zeeman levels of the same hyperfine level to act as the ground state of the Λ-scheme, whereas for the hyperfine configuration, Zeeman states of the two different ground hyperfine states are used to serve as the ground state levels.

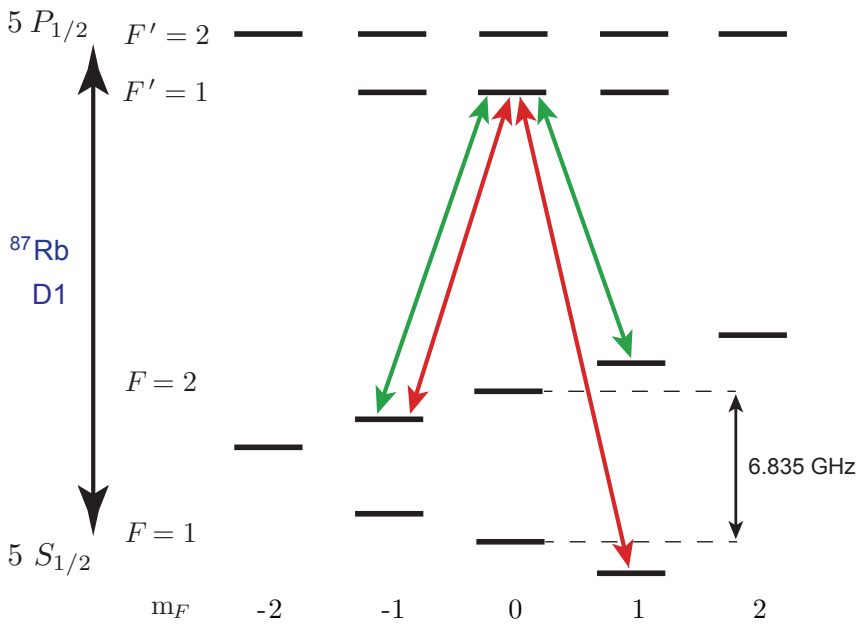

Figure 3.1: Rubidium energy level scheme based on D1-line transition. Both hyperfine (red solid lines) and Zeeman (green solid lines) configuration are used for the creation of a Λ- scheme.

A cylindrical 50 mm long, 26 mm wide rubidium glass cells is used, filled with the buffer gas depending on the experimental requirements. The buffer gas is added to change from ballistic to diffusion motion, increasing the coherence time by elastic collisions with the rubidium atoms and simultaneously increasing the interaction time of the traversing optical fields with the ensemble. The glass cell containing rubidium is placed on an aluminum holder that supports a long aluminum tube used for heating of the cell (see Fig. 3.2). In the experiments, the temperature is controllably held in the range between 50°C and 80°C by the application of resistive cartridge heaters (HT15W).

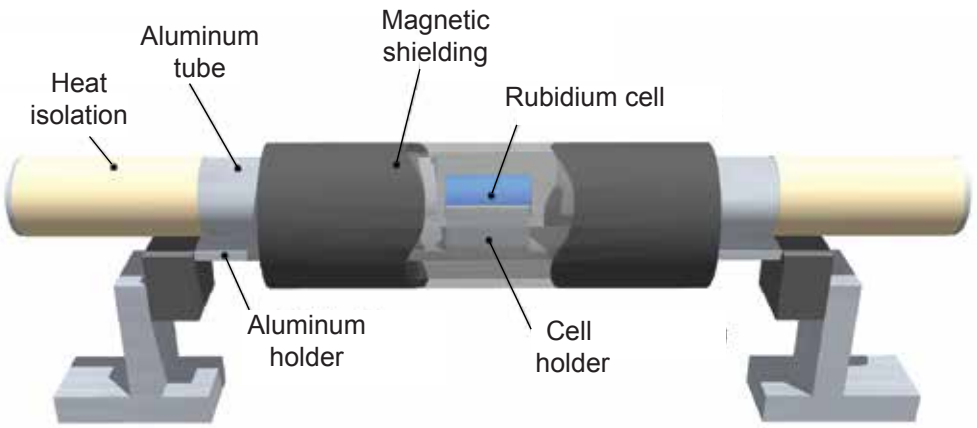

Figure 3.2: Scheme of rubidium atomic vapour apparatus consisting of the rubidium cell, the aluminum support component, the heating system, and the magnetic shielding. Two pair of coils producing longitudinal and transversal magnetic fields are placed inside the magnetic shielding (not shown). Schematic adopted from [65].

A magnetic bias field, which lifts Zeeman degeneracy of the ground state levels, is applied using coils wounded around the rubidium cell. The apparatus shown in Fig. 3.2 contains two such coils, one long coil producing the magnetic field parallel with the optical axis and a pair of coils producing transversal magnetic field. For these two coils, the following relation between the achieved value of the Zeeman spitting $\Delta\nu$ and the applied current I is obtained experimentally, for the longitudinal coil $\Delta\nu_{\parallel}(I) = 8.32$ kHz/mA $\cdot\, I$ and for the transversal coil $\Delta\nu_{\perp}(I) = 0.75$ kHz/mA $\cdot\, I$. In order to protect the atomic system from the influence of any stray magnetic fields, a μ-metal shielding is necessary. For this, a double layer μ-metal shield encloses the rubidium cell.

3.2 Preparation of the optical fields

In order to obtain a coherent superposition of the ground state levels of the atomic system, a coherent electromagnetic excitation of the atomic medium is required. The dark states, created in the three level Λ-scheme in the alkali atoms, require two coherent optical fields, the control and the signal field. For a source of coherent optical light fields, self-built external cavity diode lasers (ECDL) in a so-called Littrow configuration [66] (see Fig. 3.3) are used. Two different laser diode types - QPhotonics QLD-795-150S;

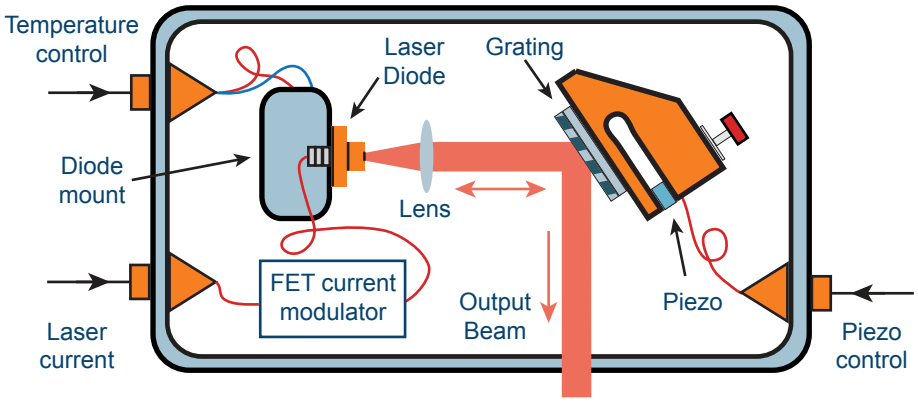

Figure 3.3: Sketch of the external cavity diode laser in Littrow configuration.

Toptica DL-0800-0100-1 - were experimentally available. With the use of extended cavities and a grating to select the desired mode, the comparatively large linewidth of the free running diode laser is reduced to about 1 MHz and single mode operation of the laser is ensured. The external cavity here consists of the diffraction grating and one end facet of the laser diode. The blaze angle of the grating is chosen in such a way to reflect the -1 order back into the diode and to subsequently optically seed the gain medium amplifying at the frequency of the injected light. The zeroth reflection order is coupled out and subsequently used in the experimental apparatus.

The output frequency of the laser can be scanned by modifying the length of the external cavity by changing the grating position with the piezoelectric transducer mounted on the grating itself. In this way, laser frequency tunability of several GHz with a bandwidth of several kHz can be achieved. Since temperature changes of the laser diode cause slow drifts of the laser frequency, the temperature has to be actively controlled and monitored by a Peltier element and a temperature sensor (IC AD590).

In the experiments, the used ECDLs are tuned to the rubidium D1-line near 795 nm wavelength. Rubidium atomic vapour is used as the optical medium in the experiments conducted in the framework of this thesis. The lasers are actively stabilized on the hyperfine transitions in ^{87}Rb, typically on the $5S_{1/2}\ F = 1 \rightarrow 5P_{1/2}\ F' = 1$ and $5S_{1/2}\ F = 2 \rightarrow 5P_{1/2}\ F' = 1$ transitions (see Fig. 3.1). The laser frequency stabilization technique, used in most of the experiments, is a dichroic atomic vapour laser lock (DAVLL) procedure [67]. The DAVLL technique, without going into the details, gives a dispersion-like voltage error signal (black solid line Fig. 3.4) that can be applied to the piezo stack controlling the grating position through an active feedback PID controller. The frequency locking point of the laser can be set and continuously scanned around the atomic resonance frequency in a range of several hundred MHz. To monitor required hyperfine transitions in ^{87}Rb in parallel with the obtained error signal, a setup allowing for a Doppler-free saturated absorption spectrum (red solid line Fig. 3.4) is realized.

For the Zeeman configuration (see Fig. 3.1), the same laser source is used for the creation of the optical control and signal beams. Both the amplitude and the frequency of the control and the signal fields can readily be controlled by two different acousto-optical

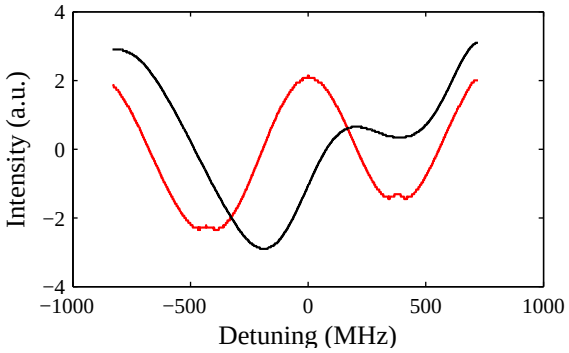

Figure 3.4: Doppler-free saturation absorption spectrum (red line) and the corresponding DAVLL error signal (black line). From left to right, absorption resonances with Lamb dips for ^{87}Rb D1-line hyperfine transitions $F = 2 \rightarrow F' = 1$ and $F = 2 \rightarrow F' = 2$ (red line).

modulators (AOMs). The optical fields creating the dark states need to have a constant phase relationship between each other, which is here easily fulfilled by driving the AOMs with the same frequency generator.

To use different ^{87}Rb hyperfine levels for the creation of the dark states, two different diode lasers are needed since the hyperfine splitting between the levels $5S_{1/2}$ $F = 1$ and $5S_{1/2}$ $F = 2$ is 6.834 GHz. Also, a phase lock between the two separate diode lasers has to be achieved, which is realized by an optical phase locked loop (OPLL), where a reference oscillator (a master laser) forces a local oscillator (a slave laser) to track its phase and frequency, maintaining a constant phase relation (Fig. 3.5). The master laser itself is frequency stabilized by the DAVLL technique.

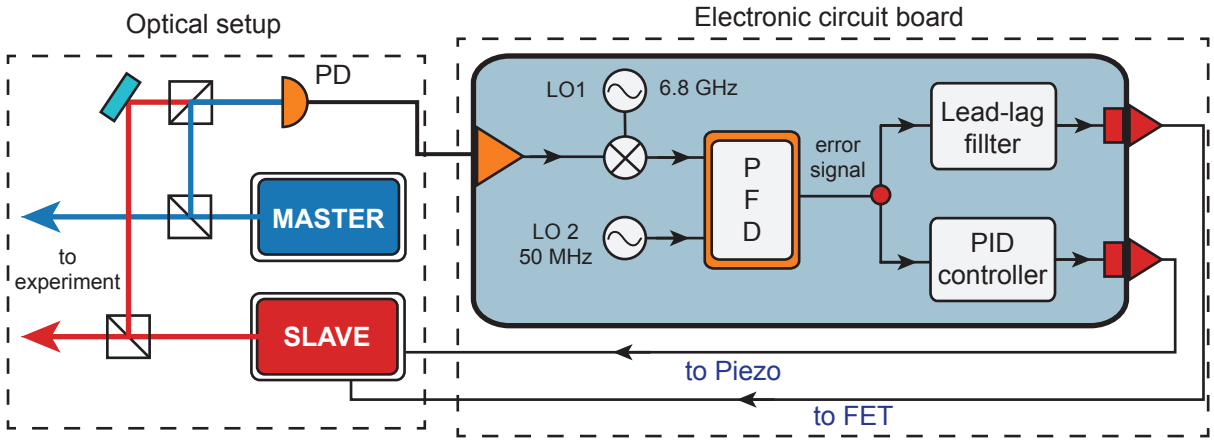

Figure 3.5: Diagram of the optical phase locked loop. In the optical setup (left-hand side), the AC component of the beat signal between master and slave laser is passed from the photodiode (PD) to the electronic part of the feedback (right-hand side). There it is shifted to 50 MHz and connected together with a stable local oscillator (LO) to phase frequency detector (PFD), which gives an error signal proportional to the phase difference of two inputs. The error signal is then fed back to the slave laser.

Firstly, the portion of the master and slave laser light is interfered and detected on a fast photodiode (Hamamatsu G4176), producing a beat signal near the frequency of the aforementioned hyperfine splitting. Later, the beat note signal is shifted down with a frequency mixer to approximately 50 MHz and together with another reference oscillator operating at 50 MHz connected on the inputs of a phase frequency detector (PFD) [68,69]. The PFD contains both an analog and digital phase and frequency detector combining advantages of both techniques. The analog detector inside the PFD corrects the phase deviations in the range between $-\pi$ and π, whereas the digital detector counteracts higher phase deviations bringing them back in the operating range of the analog detector. Ideally, the PFD produces an error signal changing linearly with the phase shift. The low frequency components of the error signal are sent to the piezo stack modulating the ECDL's grating position. In parallel, the fast frequency components are fed to the diode laser injection current through a modulation circuit. Before being sent to the injection current modulation stage, high frequency error components are corrected for the phase drifts by lead-lag filter. These phase drifts stem from a time delay Δt of signal propagation through both optical and electrical components and for high frequencies, they are very critical since the acquired phase difference becomes $\Delta\phi = \omega\Delta t$.

With the applied OPLL, a typical phase lock beat spectrum between the master and the slave laser is recorded on the spectrum analyzer (Fig. 3.6). A narrow peak at the frequency of the hyperfine splitting of 6.835 GHz is observed, together with two servo bumps approximately 1 MHz away from the central peak. From the observed spectrum, one can calculate the percentage η of the total power contained in the carrier (in this case

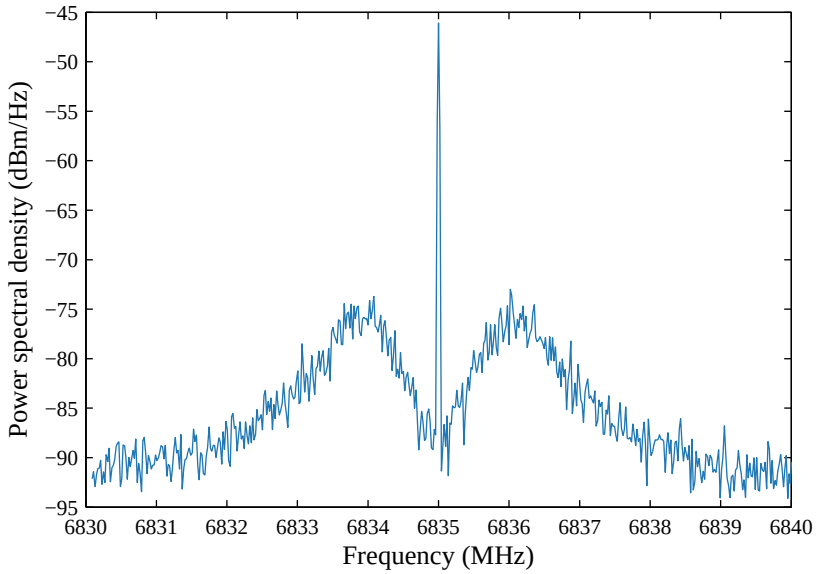

Figure 3.6: Beat signal between two diode lasers with active optical phase lock loop, recorded on a spectrum analyzer. A typical narrow peak at the frequency of the hyperfine splitting is clearly observable. The bandwidth of the feedback loop can be deduced from servo-bumps that lay approximately 1 MHz away from the narrow peak.

approximately 90 %) and from that also the rms phase error σ_ϕ as [70, 71]:

$$\sigma_\phi = \sqrt{-\ln(\eta)} = (18.2 \pm 1.0)^\circ, \tag{3.1}$$

which is comparable with the values previously reported in quantum optics experiments [72].

3.3 The optical setup

The choice of the atomic level configuration, besides imposing conditions on the number and the design of the stabilization of the optical sources, requires also careful planning of the optical setup. In this section, only a brief overview of the dark state experiment in the Λ-scheme is given (see Fig. 3.7). The Λ-scheme is realized in the Zeeman level configuration.

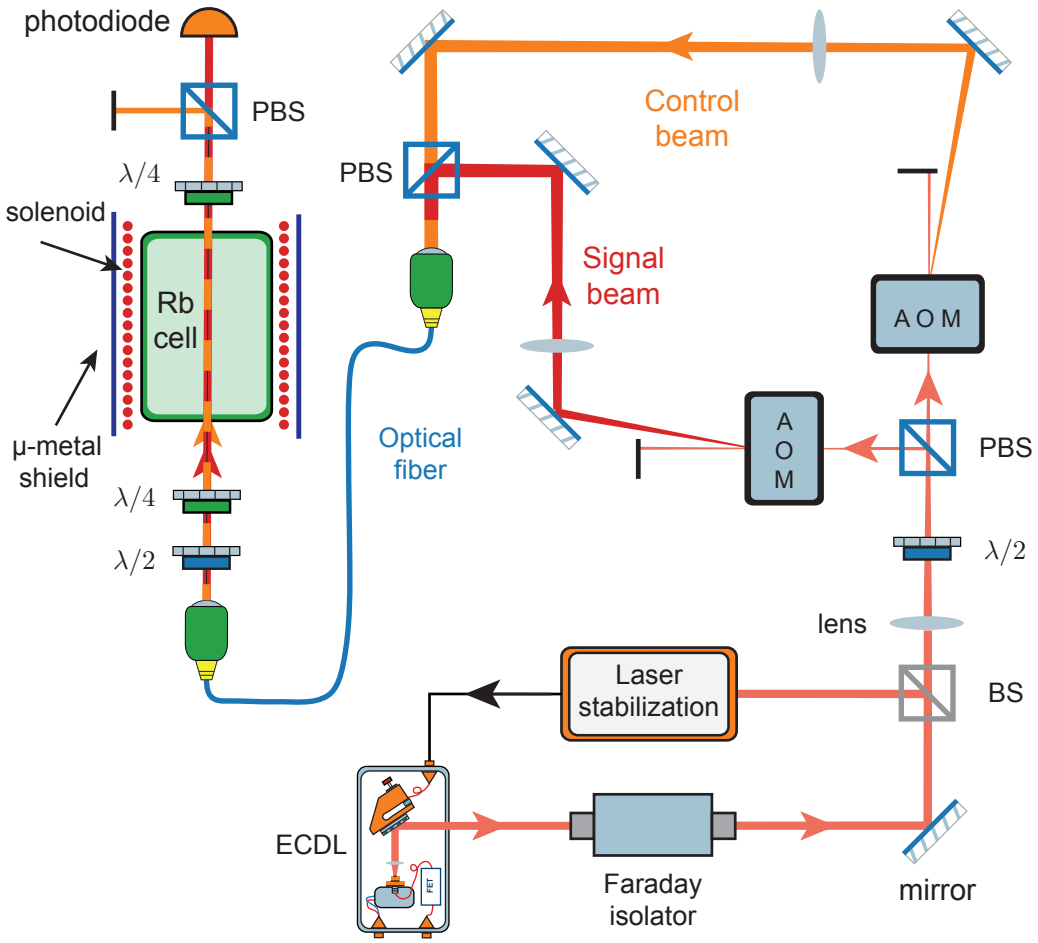

Figure 3.7: Scheme of the optical setup used in the EIT experiment in Λ-configuration. BS stands for beam splitter, PBS for polarizing beam splitter, and AOM for acousto-optic modulator. $\lambda/2$ indicates a half-wave plate, and $\lambda/4$ a quarter-wave plate.

After leaving the external cavity diode laser and passing through the Faraday isolator, which prevents potentially harmful reflections going back into the diode laser, a small fraction of the laser power is taken for the laser stabilization setup and the rest of it is coupled to the experimental optical setup. To produce the two optical fields, the control and the signal laser beam, the initial laser beam is split into the two parts with the use of a $\lambda/2$-wave plate and a polarizing beam splitter (PBS). Each of these two linearly polarized laser beams is then focused on acousto-optic modulators (models used: Crystal Technology AOM 3200-121 and Gooch & Housego R23080-2-LTD) allowing for the separate control of the amplitude and the frequency of the optical beams. The light fields, after being collimated, are then overlapped on the PBS and coupled into the polarization maintaining single mode fiber leading to their spatial mode matching. The control and the signal beam leaving the optical fiber are expanded to typically 5 mm beam diameter and with a $\lambda/4$-wave plate transformed into the σ^+ and σ^- polarized light fields. Such collinear laser beams are then passed through the rubidium vapour apparatus. Afterwards, both beams are converted into initial linear polarizations with another $\lambda/4$-wave plate. Linearly polarized control and signal beams can now be separated with a PBS, after which the signal beam is detected on a photo-diode.

In order to secure resonant excitation of the medium by the applied optical fields, the frequency of the light field in the frequency stabilization setup is additionally shifted with the acousto-optic modulator for the same amount as the optical fields used in the experimental setup.

3.4 Detection

The typical analysis of the light fields leaving the rubidium cell consists of the detection of the transmitted light intensity with a photodiode (Perkin Elmer FFD 100) and observing the corresponding detection signal on the oscilloscope. Besides this method, the experimental analysis relies also on the detection of a beat note signal with a fast photodiode. In general, the beat note stems from the interference of the two co-propagating light fields that are impinging on the photodiode. For example, two experimentally used optical signal fields $E_{S1} = E_{\mathrm{S}10}e^{\omega_{\mathrm{S}1}t}$ and $E_{\mathrm{S}2} = E_{\mathrm{S}20}e^{\omega_{\mathrm{S}2}t}$ create a photodiode output signal proportional to $|E_{\mathrm{S}1}^2 + E_{\mathrm{S}2}^2|$. The recorded intensity I then has the following form:

$$I \propto |E_{\mathrm{S}1}|^2 + |E_{\mathrm{S}2}|^2 + 2|E_{\mathrm{S}1}E_{\mathrm{S}2}|\cos(\Delta\omega t). \tag{3.2}$$

In this way, a signal is detected, whose AC component is proportional to the frequency difference $\Delta\omega$ of the two signal fields, which can later be studied. The optical setup allows also for a beat note between the zeroth AOM order and the optical signal fields to be observed by heterodyne beat detection (Fig. 3.8). From this, a signal proportional to the amplitudes $E_{\mathrm{S}1,2}$ of the signal field is obtained, which can be frequency separated and monitored independently.

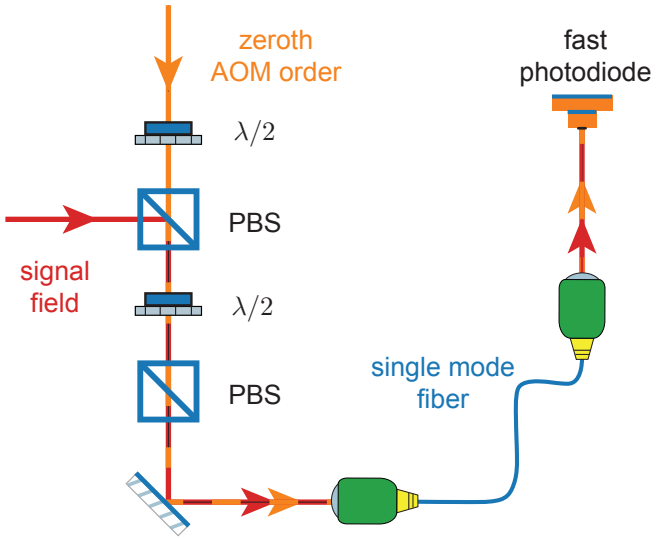

Figure 3.8: Scheme of the heterodyne beat detection setup. The measured signal is proportional to the amplitudes $E_{S1,2}$ of two signal fields. The polarizations of the zeroth AOM order and the signal field are first projected onto each other. Mode matching of the two fields is achieved by coupling them into the single mode fiber and subsequently, they are detected on a fast photodiode. The same beat detection setup is used for the optical phase lock loop.

3.5 Characterization measurements

The coherent effects studied in the framework of this thesis, particularly the ones studied in chapters 4 and 5, rely on the existence of the electromagnetically induced transparency and the phenomena closely related to it, like slow light and storage of light effects. In the following subsections, typical results for the EIT and slow/stored light experiments are shown and used to characterize the experimental system.

3.5.1 Measurements of electromagnetically induced transparency

The well-known electromagnetically induced transparency was originally observed in 1991 in strontium atoms [19]. In the following, measurements of EIT resonances are described, as a first step towards the later discussed experiments, recorded for two different atomic level configurations.

Firstly, the Λ-scheme realized in the hyperfine configuration is considered, for which the two phase locked lasers are needed to generate the optical couplings. One of the lasers, producing the optical control field, is tuned to the optical transition $5S_{1/2}\ F = 2 \rightarrow 5P_{1/2}\ F' = 1$, whereas the laser that produces the optical signal field, couples the transition between the $5S_{1/2}\ F = 1$ and $5P_{1/2}\ F' = 1$ hyperfine states. The control field and the signal field are σ^+ and σ^- polarized, respectively and after their interaction with the rubidium atoms in the buffer gas cell, only the transmission of the signal beam is detected on the

photodiode. The frequency of the signal field is scanned in order to observe the EIT resonance, exhibiting maximal transparency at the zero frequency detuning (Fig. 3.9). This resonance is achieved in the Λ-scheme that involves the two-photon transition between the states $|F = 2, m_F = -1\rangle$ and $|F = 1, m_F = 1\rangle$ and is in the first order insensitive to variations in the magnetic bias field. Another EIT resonance, not shown here, can be realized for the following two-photon transition $|F = 2, m_F = -2\rangle \leftrightarrow |F = 1, m_F = 0\rangle$ that is magnetic field sensitive (see Fig. 3.1). The frequency difference between the magnetically nonsensitive and sensitive resonances respectively is here used to calculate the applied magnetic field and calibrate the bias field coils. The width of the EIT resonance, shown in Fig. 3.9, is obtained from the fit of the Lorentzian function to the measured data points and is calculated to be 13 kHz. The data set is taken for the Rabi frequencies of the control and signal fields of $\Omega_C = 1.87$ MHz and $\Omega_S = 0.65$ MHz, respectively (calculated for the respective optical powers of $P_C = 500$ μW and $P_S = 180$ μW in a beam diameter of 5 mm). The temperature of the rubidium gas cell was held at 80°C.

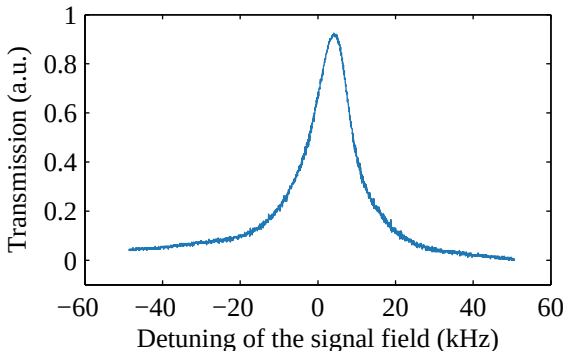

Figure 3.9: Electromagnetically induced transparency measured in hyperfine configuration as a function of the detuning of the signal field. The FWHM is approximately 13 kHz.

The EIT measurements are also performed for the Λ-scheme in the Zeeman configuration using the optical setup described in the section 3.3. The diode laser, that provides the optical control and signal fields, is locked on the $5S_{1/2}$ $F = 2 \rightarrow 5P_{1/2}$ $F' = 1$ hyperfine transition, and the optical fields are coupled with the corresponding Zeeman ground sublevels to form the Λ-interaction scheme. The EIT resonance (Fig. 3.10) is taken for 2 mm laser beam diameter and the Rabi frequencies of the optical control and signal beams of approximately $\Omega_C = 3.5$ MHz and $\Omega_S = 1.8$ MHz. For this measurements, a rubidium cell without buffer gas is used, heated up to 75°C, where the atomic motion is entirely ballistic and the atomic coherence depends on the time that atoms need to pass the laser beam. Since the atoms lose their ground state coherence in collisions with the cell walls, the EIT resonance width in the vacuum Rb cells is broader than the width measured in the buffer gas cells. The width of the resonance shown in Fig. 3.10 is approximately 55 kHz.

The dependency of the EIT width on the control beam optical power is also recorded, from which one can determine the decoherence rate of the system [73]. Main decoherence mechanisms of the experimentally used system can be attributed to atom-atom and atom-wall collisions, to finite interaction time of atoms with the laser beam, and to magnetic

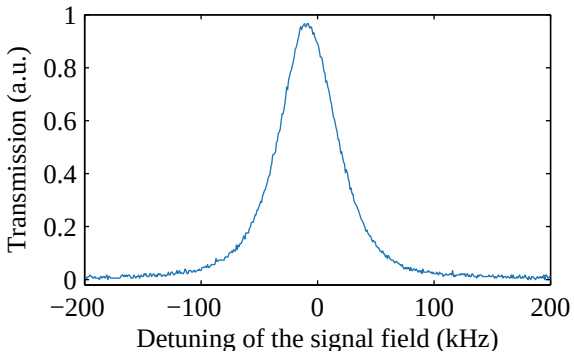

Figure 3.10: Electromagnetically induced transparency signal meversus detuning of the signal field, measured in Zeeman configuration. The FWHM of the dark resonance is approximately 55 kHz.

field inhomogeneity. The FWHM of the dark resonance can be calculated from:

$$\mathrm{FWHM} = 2\gamma_{\mathrm{bc}} + \frac{4|\Omega_{\mathrm{C}}|^2}{2W_{\mathrm{d}} + \gamma_{\mathrm{a}}}, \tag{3.3}$$

where W_{d} is the width of the Doppler broadened resonance. Since $|\Omega_{\mathrm{C}}|^2$ is proportional to the laser beam intensity, it follows from the previous equation Eq. 3.3 that the EIT linewidth scales linearly with the control beam power, allowing the decoherence rate γ_{bc} to be determined from the linear fit results. The data presented in Fig. 3.11, after being fitted with the linear function, reveal a decoherence rate of the ground state of 4 kHz. Consequently, the time scale, on which the coherent dynamics of the system can be studied, is in the order of milliseconds.

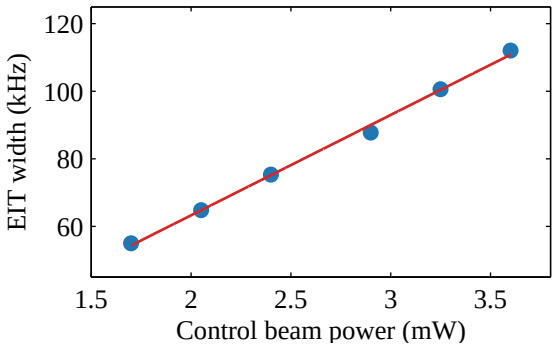

Figure 3.11: EIT linewidth versus a control beam optical power for six different measurements in Λ configuration.

3.5.2 Slow light

Slowing of light in EIT medium was first observed in 1999 in a BEC [25] and in hot rubidium vapour [21, 74]. The basic properties of the slow light effect are described in chapter 2. To characterize the system, here slow light measurements using both Zeeman and hyperfine configuration are performed. The experimental conditions for the slow light measurements are similar to the ones given in the above section except that signal field pulses have to be created. This is accomplished by sending the time-varying Gaussian shaped voltage signal to the AOM, which controls the behavior of the signal field, producing the signal light pulses of Gaussian envelope. The light pulses are then sent through the heated rubidium cell and recorded on the photo-diode. On their way through the EIT medium, light pulses acquire a certain time delay, which is determined by comparing the center of the Gaussian light pulse with the falling edge of the trigger pulse (Fig. 3.12 black line) of the device that creates the time-varying voltage signal. The precise position of the center of the Gaussian pulse is obtained from the Gaussian fit of the recorded data points. For a signal beam pulse of approximately 100 μs duration, and the optical control and signal beam powers of 240 μW and 70 μW, respectively, the time delay of 4.7 μs is measured for the hyperfine configuration in the rubidium buffer gas cell held at temperature of 80 °C (Fig. 3.12(a) solid red line).

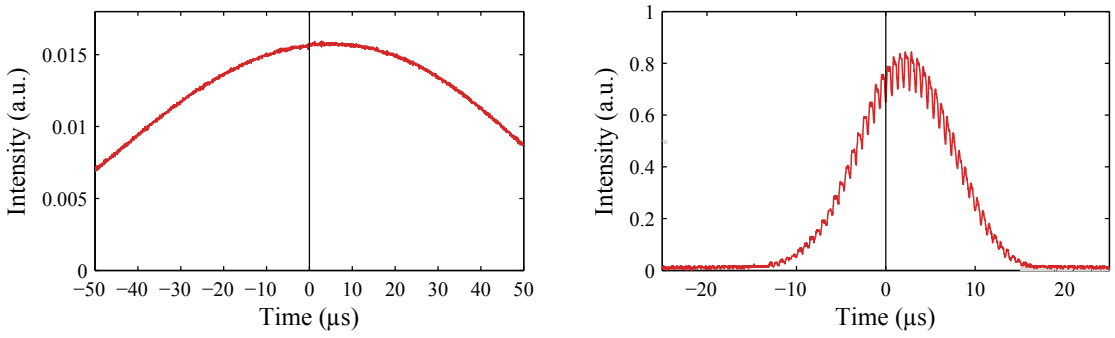

Figure 3.12: Slow light pulse for: (a) hyperfine configuration in the rubidium buffer gas cell, and (b) Zeeman configuration in the rubidium vapour cell with no buffer gas present. The black vertical lines represent the position of the pulse maximum in the absence of the rubidium vapour cell in each case.

From the delay time τ_d and cell length L of 5 cm, the group velocity v_{gr} can easily be calculated:

$$v_{gr} = \frac{L}{\tau_d}, \tag{3.4}$$

which, for the $\tau_d = 4.7\mu$s, corresponds to the group velocity of 11 km s^{-1}.

The signal light pulse is also detected in the Zeeman configuration for the rubidium vapour cell without the presence of the buffer gas. The cell is heated up to 50 °C and control and signal beam optical powers are 800 μW and 300 μW respectively. The measured

time delay of the signal field pulse for such system is approximately 2.2 μs (solid red line in Fig. 3.12(b)), leading to a group velocity of 23 km s^{-1}. In the formalism of the dark state polaritons (see section 2.2), measuring the group velocity of the slow signal light pulse actually means determining the propagating velocity of the dark state polariton. Knowledge on the exact value of the polartion velocity is of the crucial importance in later evaluation the experimentally available Aharonov-Casher phase in chapter 5.

3.5.3 Storage of light

A reversible transfer of the photonic quantum state to the collective atomic spin coherences can be done in a storage of light procedure, by adiabatically reducing the intensity of the control field to zero. The stored information can later be coherently retrieved by turning the control field back on. This phenomenon is well-explained in terms of dark state polaritons [61] and demonstrated for the first time in 2001 in atomic vapour [29]. Here, the storage of light is achieved experimentally by pulsing the optical fields with the help of the AOMs. A digital pulse delay generator sends tailored pulses through RF switches to the AOMs, which in turn control the behavior of the optical fields. The pulse sequence is repeated continuously with the period of 200 μs (see Fig. 3.13). To store the signal

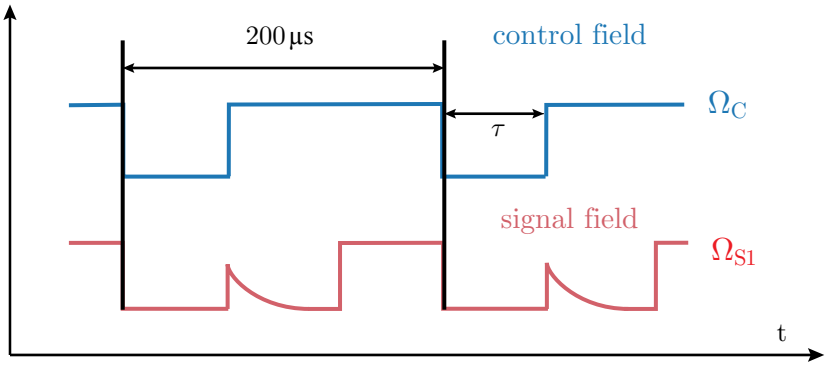

Figure 3.13: Typical experimental pulse sequence for storage of light measurement with a period of 200 μs. The control and the signal field are simultaneously switched off at the beginning of the pulse cycle. After the storage time τ, only the control field is switched back on.

light field, both the control and the signal field pulses are simultaneously turned off for a certain storage period. After a storage time τ up to 30 μs, only the control field is switched on, causing the retrieval of the stored light. The signal field is turned on 100 μs after the start of the storage procedure and together with the control field, kept on until the end of the whole cycle (Fig. 3.13).

The result of storage of light measurement for a Λ-scheme in a hyperfine configuration is shown in Fig. 3.14. The optical powers of the control and the signal field are set to 350 μW and 90 μW, respectively. The storage time is 15 μs and the size of the Zeeman splitting 600 kHz.

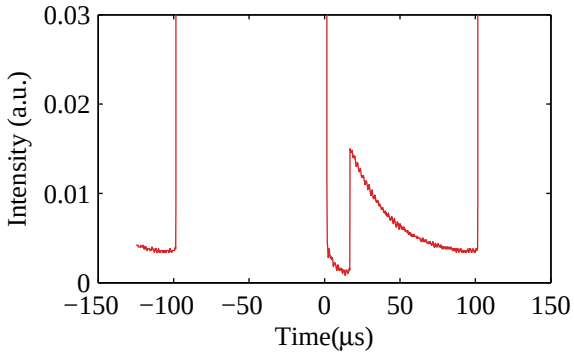

Figure 3.14: Typical signal of storage of light measurement in the hyperfine configuration, detected on a photodiode. The optical fields are both turned off at $t = 0$. After the storage time of 15 μs only the control field is turned back on and the signal field is restored.

The experimental decoherence rate of the system can also be obtained from storage of light measurements [73], by measuring the intensity of the retrieved light as function of the duration of storage time. The decoherence rate between the ground states γ_{bc} can be found by fitting the measured data (see Fig. 3.15) with an exponential function $f(t) = a \cdot e^{-b \cdot t}$. From the fit parameter b, one can calculate the decoherence rate to be $\gamma_{\mathrm{bc}} = b/(2\pi) = (4.6 \pm 0.4)$ kHz.

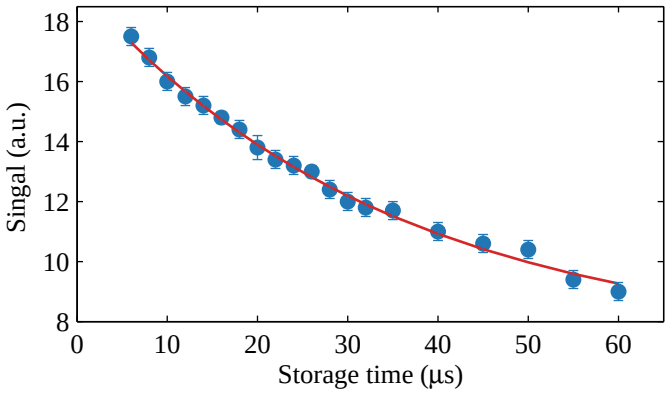

Figure 3.15: Signal of the retrieved light versus storage time in the hyperfine configuration. The blue dots represent experimental data, while the red line represents a fit. The error bars show estimated uncertainty of the signal field intensity measurement.

4 RF-spectroscopy of dark state polaritons

In the formalism of dark state polaritons, the slow/stored light effects in the EIT regime can be attributed to moving quasiparticles consisting of an atomic and a photonic contribution (Sec. 2.2). Here, the particle-like properties of the DSP are investigated by aiming to demonstrate the first spectroscopic experiments on dark state quasiparticles. To this end, a four level tripod interaction scheme in the atomic rubidium vapour is realized, providing quasiparticles with an internal state structure. The tripod configuration is originally considered in both theoretical [75, 76] and experimental work [77, 78] regarding coherent population transfer by stimulated adiabatic Raman passage followed with the controllable creation of a coherent superposition of two atomic states. This previous work revealed the existence of two orthogonal, adiabatic and degenerated states for the tripod level scheme. It was also shown that in such four-level atoms two slowly propagating optical modes co-exist [79].

The following section gives a theoretical introduction to the properties of dark states in the tripod scheme accompanied by experimental measurements of the dark resonances. Later, both experimental and theoretical results of the RF-spectroscopy of the DSPs are discussed.

4.1 Theoretical and experimental introduction

In this section, a four-level atomic system, as shown in Fig. 4.1., with one spontaneously decaying electronically excited state $|a\rangle$ and three stable ground states $|b\rangle$, $|c\rangle$, and $|d\rangle$ is considered. The atomic system interacts with three optical fields, two of which represent the signal fields with their respective Rabi frequencies Ω_{S1} and Ω_{S2}, and the third field being the optical control field with the Rabi frequency Ω_C. The two signal fields Ω_{S1} and Ω_{S2} couple the excited state $|a\rangle$ with the ground states $|b\rangle$ and $|d\rangle$, respectively, whereas the control field Ω_C couples the transition between the states $|c\rangle$ and $|a\rangle$ of the tripod linkage scheme.

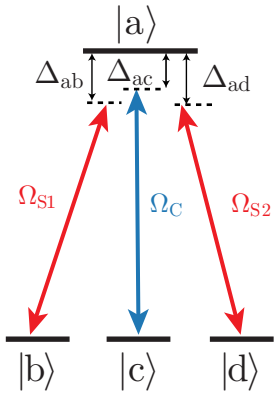

Figure 4.1: Simplified tripod-level scheme with one excited state $|a\rangle$, coupled with three ground states $|b\rangle$, $|c\rangle$, and $|d\rangle$ by light fields of Rabi frequencies Ω_{S1}, Ω_C, Ω_{S2}.

The interaction Hamiltonian of the tripod system can be written as:

$$H(t) = \frac{\hbar}{2}\begin{pmatrix} 0 & \Omega_{\mathrm{S1}}(t) & \Omega_{\mathrm{C}}(t) & \Omega_{\mathrm{S2}}(t) \\ \Omega_{\mathrm{S1}}(t) & 2\Delta_{\mathrm{ab}} & 0 & 0 \\ \Omega_{\mathrm{C}}(t) & 0 & 2\Delta_{\mathrm{ac}} & 0 \\ \Omega_{\mathrm{S2}}(t) & 0 & 0 & 2\Delta_{\mathrm{ad}} \end{pmatrix}, \tag{4.1}$$

where Δ_{ab}, Δ_{ac}, and Δ_{ad} are the one-photon detunings of the optical fields, as denoted in Fig. 4.1. The adiabatic instantaneous eigenstates of $H(t)$ can be defined for a special case where all optical fields are resonant with their respective transitions, together with the condition that the optical signal fields have the same Rabi frequency $\Omega_{\mathrm{S}}(t)$, and $\Omega_{\mathrm{S}}(t) \ll \Omega_{\mathrm{C}}(t)$. Two of the eigenstates are degenerate, with no contribution from the excited state $|\mathrm{a}\rangle$ and therefore, they are called dark states [75]:

$$|\Phi_1(t)\rangle = \frac{1}{\sqrt{2}}\Big(|\mathrm{b}\rangle + |\mathrm{d}\rangle\Big) - \sqrt{2}\Big(\frac{\Omega_{\mathrm{S}}(t)}{\Omega_{\mathrm{C}}(t)}\Big)|\mathrm{c}\rangle\,, \tag{4.2}$$

$$|\Phi_2(t)\rangle = \frac{1}{\sqrt{2}}\Big(|\mathrm{b}\rangle - |\mathrm{d}\rangle\Big). \tag{4.3}$$

The energy of the two dark states here is zero. Further, the two other bright eigenstates that contain state $|a\rangle$ are given as:

$$\Phi_{\mathrm{B}\pm} = \frac{\Omega_{\mathrm{S}}(t)\Big(|\mathrm{b}\rangle + |\mathrm{d}\rangle\Big) + \Omega_{\mathrm{C}}(t)\,|\mathrm{c}\rangle \pm |\mathrm{a}\rangle}{\sqrt{2{\Omega_{\mathrm{S}}}^2 + {\Omega_{\mathrm{C}}}^2}}. \tag{4.4}$$

For the above conditions, the group velocity of both signal fields [80] can be expressed:

$$v_{gr} \approx \frac{4\hbar c\epsilon_0}{\omega_{\mathrm{S}}|\mu_{\mathrm{ab}}|^2}\Big(|\Omega_{\mathrm{C}}|^2 + |\Omega_{\mathrm{S}}|^2\Big). \tag{4.5}$$

Evidently, in the tripod system, two different dark modes with the same group velocity can exist, which can be treated as a quasiparticle with internal structure.

4.1.1 Quasi-particle picture

To find the polariton representation of the EIT effects in the ensemble of tripod atoms, one starts by considering two signal beams as quantum fields $\hat{E}_{\mathrm{S1,2}}(z,t)$ and the control beam as a classical field of Rabi frequency $\Omega_{\mathrm{C}}(t)$ (as defined in Sec. 2.2). For the pulse propagation of the signal fields through the tripod medium, two assumptions need to be fulfilled. Firstly, the low-intensity approximation, for which the Rabi frequency of the quantum signal field is much smaller than the one in the classical case and the number density of atoms N is much bigger than the number density of photonic excitations n. Secondly, a slowly-varying amplitude of the Rabi frequencies has to be assumed as well, i.e. the adiabatic limit. Then the propagation equations of the two quantum signal fields are [81]:

$$\left(\frac{\partial}{\partial t} + c\frac{\partial}{\partial z}\right)\hat{E}_{\mathrm{S1}}(z,t) \cong -\frac{g^2 N}{\Omega_{\mathrm{C}}(t)}\frac{\partial}{\partial t}\left[\frac{\hat{E}_{\mathrm{S1}}(z,t)}{2\Omega_{\mathrm{C}}(t)} + \frac{\hat{E}_{\mathrm{S2}}(z,t)}{\Omega_{\mathrm{C}}(t)}\rho_{\mathrm{bd}}\right] \tag{4.6}$$

$$\left(\frac{\partial}{\partial t}+c\frac{\partial}{\partial z}\right)\hat{E}_{\mathrm{S2}}(z,t)\cong-\frac{g^2N}{\Omega_{\mathrm{C}}(t)}\frac{\partial}{\partial t}\left[\frac{\hat{E}_{\mathrm{S2}}(z,t)}{2\Omega_{\mathrm{C}}(t)}+\frac{\hat{E}_{\mathrm{S1}}(z,t)}{\Omega_{\mathrm{C}}(t)}\rho_{\mathrm{db}}\right], \tag{4.7}$$

where the symmetry between the propagation of the signal fields $\hat{E}_{\mathrm{S1}}(z,t)$ and $\hat{E}_{\mathrm{S2}}(z,t)$ is visible. Also the coupling between the slow signal fields is equal to zero and both fields propagate through the atomic system independently. Defining a rotation in the space of variables $\hat{E}_{\mathrm{S1,2}}$ and the atomic spin coherences $\rho_{\mathrm{bc,dc}}$, as in expression 2.8, introduces a new set of quantum fields :

$$\hat{\Psi}_{\mathrm{D1,2}}(z,t)=\cos\theta(t)\hat{E}_{\mathrm{S1,2}}(z,t)-\sin\theta(t)\sqrt{N}\hat{\rho}_{\mathrm{bc,dc}}(z,t) \tag{4.8}$$

$$\hat{\Psi}_{\mathrm{B1,2}}(z,t)=\cos\theta(t)\hat{E}_{\mathrm{S1,2}}(z,t)+\sin\theta(t)\sqrt{N}\hat{\rho}_{\mathrm{bc,dc}}(z,t). \tag{4.9}$$

For the first pair of fields, a plain-wave decomposition $\hat{\Psi}_{\mathrm{D1,2}}(z,t)=\sum_k\hat{\Psi}_{\mathrm{D1,2k}}(t)e^{ikz}$ is introduced, which reveals bosonic commutation relations between mode operators $\hat{\Psi}_{\mathrm{D1,2k}}$ and $\hat{\Psi}^{\dagger}_{\mathrm{D1,2k'}}$. Consequently, the new fields can be associated with bosonic quasiparticles [82]. All number states created by $\hat{\Psi}^{\dagger}_{\mathrm{D1,2k}}$ are dark states, because they do not contain the excited state $|a\rangle$, for example:

$$|n\rangle_k=\frac{1}{\sqrt{n!}}(\hat{\Psi}^{\dagger}_{\mathrm{D2k}})\,|0\rangle\,|d_1...d_{\mathrm{N}}\rangle\,, \tag{4.10}$$

where $|0\rangle$ denotes the photonic state with the number of photons equal to zero or simpler, the field vacuum. The states $|n\rangle_{\mathrm{k}}$ are also eigenstates of the interaction Hamiltonian $H(t)$ with the eigenvalue zero. Therefore, the quasi-particles $\hat{\Psi}_{\mathrm{D1,2}}$ are called dark state polaritons. A similar procedure is applicable to the fields given in Eq. 4.9, which correspond to the bright state polaritons. Both of the polaritons $\hat{\Psi}_{\mathrm{D1}}$ and $\hat{\Psi}_{\mathrm{D2}}$ obey the equation of motion (see Eq. 2.9) and in general, the two component tripod polariton can be written as:

$$\hat{\Psi}_{\mathrm{D}}(z,t)=\alpha\hat{\Psi}_{\mathrm{D1}}(z,t)+\beta\hat{\Psi}_{\mathrm{D2}}(z,t). \tag{4.11}$$

The propagation of the two optical signal fields in the tripod medium under EIT conditions can now be seen as a propagation of a quasi-particle with two internal orthogonal states. The question is whether it is possible to observe the transition between the internal states of DSPs by applying a radio-frequency excitation on the tripod ground states and effectively change the occupation number of the co-existing dark states (Fig. 4.2).

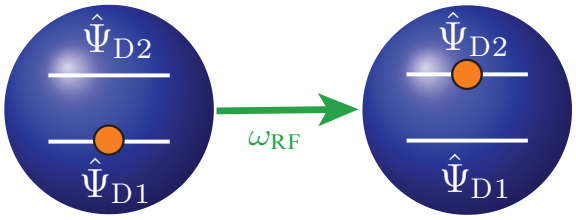

Figure 4.2: RF spectroscopy of dark state polaritons inducing population transfer between internal polariton states.

4.1.2 Experimental setup and basic RF measurements

In the course of the investigation of the radio-frequency switching between the internal states of DSP, the Zeeman configuration (Fig. 3.1) was initially used, since its experimental realization is less demanding than the hyperfine configuration. Although the Zeeman configuration on the rubidium transition $5S_{1/2}\ F = 2 \rightarrow 5P_{1/2}\ F' = 1$ provides an eight-level tripod-like linked scheme with two orthogonal dark states [83], no transitions between the polariton substates could be experimentally detected for this configuration. Theoretical calculations on the RF-spectroscopy of the DSP for the eight-level system, done by Stephan Hüwe [84] within his master thesis, confirmed this experimental findings and pointed out the necessity of using the hyperfine configuration for the tripod scheme. If not stated otherwise, all measurement discussed in this chapter are performed in the eleven-level system realized in the hyperfine configuration (see Fig. 4.3).

The RF spectroscopy measurements of the dark state polaritons in the hyperfine configuration were performed in a collaboration with the master student Georg Enzian [71]. To work in the hyperfine configuration, one needs to achieve a phase lock of two diode lasers, tuned at two different ^{87}Rb hyperfine transitions. The master laser in the OPLL, used as a source of the optical control beam, is locked at the $5S_{1/2}\ F = 2 \rightarrow 5P_{1/2}\ F' = 1$ transition, whereas the slave laser serves as a signal field source operating at the $5S_{1/2}\ F = 1 \rightarrow 5P_{1/2}\ F' = 1$ transition (Fig. 4.3). Compared to the Λ-scheme, for the

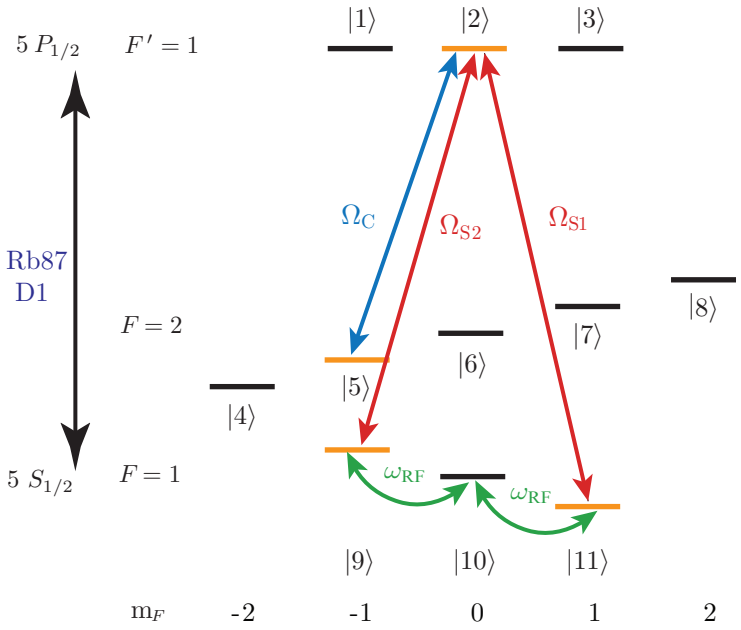

Figure 4.3: ^{87}Rb energy level scheme on the D1-line transition, used for the realization of the tripod level scheme (orange color). Optical signal fields (red solid lines) with the Rabi frequencies Ω_{S1} and Ω_{S2} couple the $F = 1 \rightarrow F' = 1$ hyperfine transition, whereas an optical control field (blue solid line) with the Rabi frequency Ω_C couples the $F = 2 \rightarrow F' = 1$ hyperfine transition. The green solid lines indicate RF field, which couples the Zeeman ground states.

tripod-scheme two signal fields are needed, created here from the same laser source by simply dividing the laser beam in two paths with a beam splitter. The two optical fields are afterwards coupled through AOMs to control their frequency and amplitude independently.

Creating the tripod linked scheme, as shown in Fig. 4.3, also demanded careful polarization preparation of the optical couplings, in which the control and one signal field would have a σ^+-polarization, whereas the other signal field would be orthogonally σ^- polarized. Hence, one of the signal beams and the control beam are first overlapped and then projected onto the same linear polarization with the help of two polarizing beam splitters (PBS). The remaining signal beam is polarized orthogonally with respect to the other two beams by overlapping all beams on the second PBS. Such linearly polarized beams are then coupled into a polarization maintaining fiber to ensure their mode matching and after leaving the fiber, expanded to a 3 mm beam diameter. Before being sent through the rubidium vapour apparatus, their polarization is converted into the desired circular polarizations via a $\lambda/4$-wave plate.

In the hyperfine configuration, the Zeeman ground state sublevels $|F = 1, m_F = -1\rangle$, $|F = 2, m_F = -1\rangle$, and $|F = 1, m_F = 1\rangle$ correspond to the states $|b\rangle$, $|c\rangle$, and $|d\rangle$ of the tripod model scheme and together with the prepared optical couplings, form the experimentally used tripod-level configuration. In general, additional two-photon transitions are allowed in this hyperfine configuration, like $|F = 2, m_F = -2\rangle \leftrightarrow |F = 1, m_F = 0\rangle$ and $|F = 2, m_F = 0\rangle \leftrightarrow |F = 1, m_F = 0\rangle$, which are off-resonant in this setup.

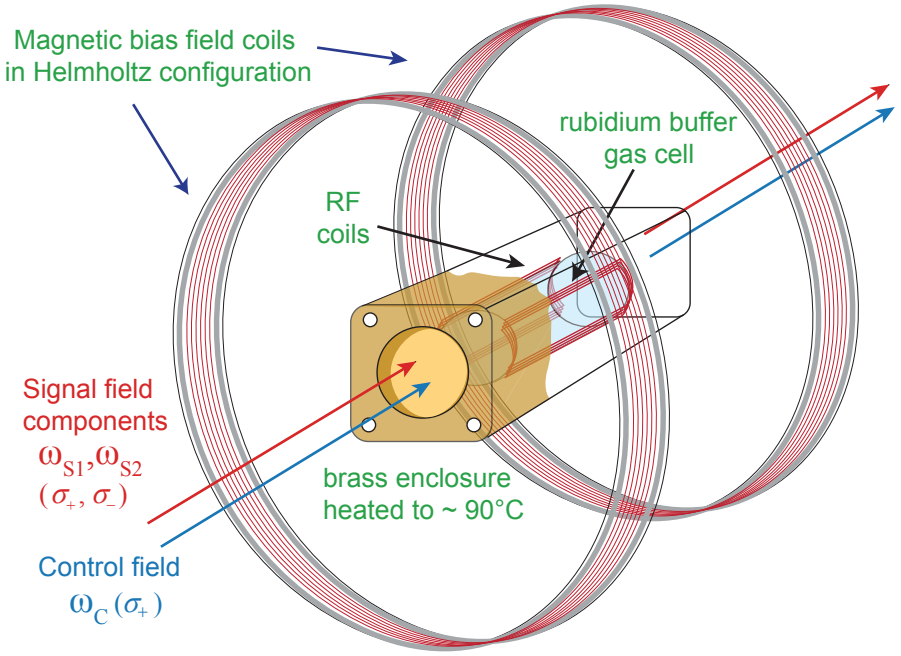

Figure 4.4: Rubidium atomic vapour apparatus used for RF spectroscopy on dark state polaritons. The glass cell containing a mixture of rubidium vapour and xenon buffer gas is placed inside brass heated enclosure. RF coils are mounted close to the rubidium cell. A longitudinal magnetic bias field is created by pair of Helmholtz coils.

The rubidium atomic vapour apparatus is a modified version of the one presented in section 3.1. The rubidium cell with xenon buffer gas is placed inside the brass enclosure (Fig. 4.4), which is heated up to 80 °C with the resistive heaters. To couple the Zeeman sublevels of the hyperfine ground states, an RF coil is mounted between the heating enclosure and the gas cell and driven by an RF power amplifier (LZY-22+ Minicircuits), capable of delivering up to 30W into a 50 Ω load. The impedance of the RF coil, for the frequency corresponding to the splitting of the Zeeman sublevels, is matched to 50 Ω resistance. The energy difference between the Zeeman ground state sublevels is typically set to 1 MHz by a pair of Helmholtz coils, which define the quantization axis in the longitudinal direction. From the calibration of the magnetic bias field coils, the Zeeman splitting for the current I up to 1 A can be calculated from the relation $\Delta\nu_{\mathrm{Zeeman}}(I) = (2.31 \pm 0.02)\mathrm{MHz} \cdot I/\mathrm{A}$. The whole rubidium apparatus is covered with the rectangular shaped, 2 mm thick μ-metal sheet (not shown in Fig. 4.4 for clarity reasons).

In order to successfully observe a transition between the internal polariton components, it is necessary to distinguish between the two signal fields in the detection procedure and monitor independently their behavior with the applied RF excitation. This is accomplished by detecting the beat note of the two signal fields and the light field from the slave laser, which is provided by the zeroth order of the AOM. The beat signal is detected on a fast photo-diode, amplified and observed on a spectrum analyzer. The signal fields are monitored on separate channels of the spectrum analyzer, which are centered on the field's respective AOM modulation frequencies and operated in zero span mode. The resolution bandwidth of the two channels has to be sufficiently narrow to isolate the beat signal components, but at the same time has to allow for the observation of the fast processes. In the experiments, the resolution bandwidth in a range of 100 kHz to 300 kHz is used. As an example, Fig 4.5. shows storage of light of two signal fields, obtained using the beat detection procedure and recorded on the spectrum analyzer. One signal field component is pulsed with 100 μs period and the pulse duration of 100 μs and detected at the beat frequency of 80 MHz (Fig. 4.5(a)). The other field component, at the beat corresponding

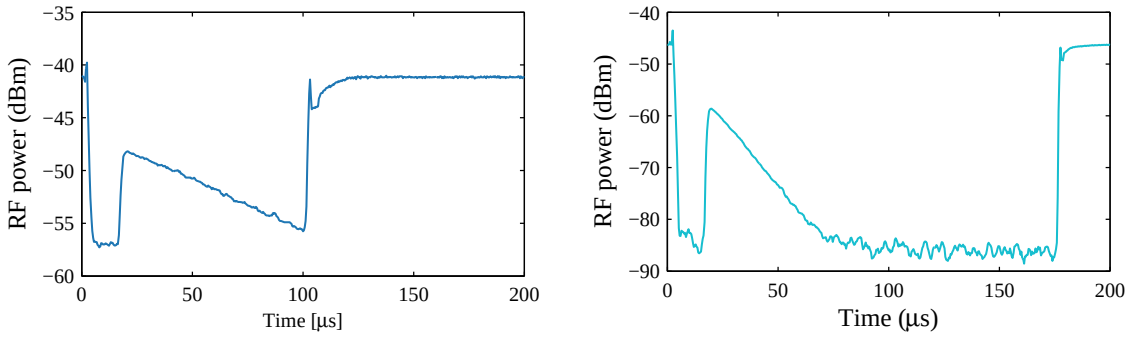

Figure 4.5: Detected storage of light for heterodyne beat spectroscopy: (a) Storage of the first signal field component at a beat frequency of 80 MHz, and (b) the second signal field at 81.2 MHz. The difference between the two beat frequencies corresponds to twice the Zeeman splitting.

to the modulation frequency of 81.2 MHz, is irradiated only for 25 μs before being turned off together with the control field (Fig. 4.5(b)). By comparing the height of the restored signal fields, it becomes obvious that the signal retrieved at 80 MHz is roughly 10 dBm higher than the signal retrieved at 81.2 MHz, which is connected with the much shorter pulse duration of the second signal field (Fig. 4.5(b)). Different interaction times of the two signal fields with the rubidium atoms are realized to create two dark states with an initial population difference for the subsequent RF spectroscopy experiment.

The influence of the RF excitation on the EIT resonance is studied by simply monitoring the intensity of the transmitted signal field on the photo-diode while scanning the frequency of the RF field. This measurement is done in the simple Λ-configuration, with the signal field frequency kept exactly at the zero two-photon detuning and the Zeeman splitting set to roughly 600 kHz. The recorded measurement (Fig. 4.6) shows a decrease in the signal field transmission at the frequency corresponding to the value of a single Zeeman splitting. This behavior is attributed to the depopulation of the dark state caused

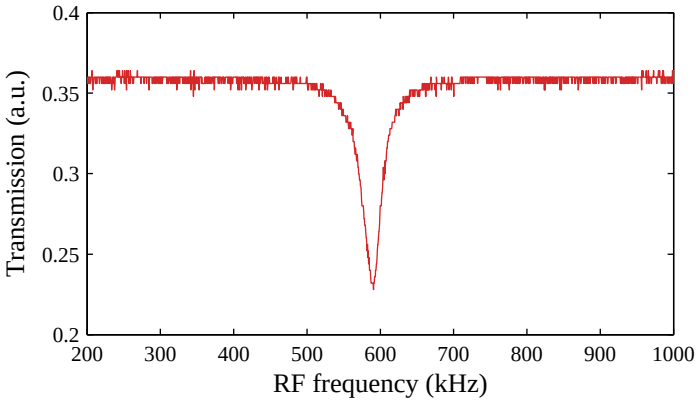

Figure 4.6: Radio-frequency resonance for EIT conditions. Transparency of the signal field is reduced at the RF frequency equal to the size of the Zeeman splitting. The optical control and signal beam powers were set to 300 μW and 130 μW respectively.

by the RF excitation. The experimental Rabi frequency of the RF field, used also in theoretical considerations, can be found from the RF power broadening of the observed transmission dip. The measured Rabi frequency of the RF field is determined to be $\Omega_{RF}/I_{RF} = (2.6 \pm 0.1)$ MHz A^{-1}.

4.1.3 Initial theoretical calculations

Before presenting the measurements regarding polariton spectroscopy, the basic properties of theoretical calculations, performed to complement the experimental findings, should be noted. In the calculations, the time evolution of the atomic system interacting with the optical and RF excitation fields is simulated. An eleven-level atomic system is considered, mimicking the experimentally used ^{87}Rb hyperfine levels subjected to an external magnetic bias field. All considerations are done in the semi-classical regime (Sec. 2.3), where the density matrix ρ gives the full description of the system in the time-domain.

For this, solving the Liouville equation (2.11) for the experimental set of parameters is the primary goal. The density matrix ρ contains 121 elements, from which the diagonal and off-diagonal elements give the information about the atomic populations and transitions, respectively. The interaction Hamiltonian $H(t)$ and the relaxation superoperator Γ, defined in the Eq. 2.11, are represented by 121×121 dimensional matrices. The initially performed simulations in MATLAB, tested whether the theoretical model behaves as one would expect for different starting conditions. In that sense, the simulation results regarding the spontaneous decay of the excited state, the RF transfer of the population between the Zeeman ground states, and storage of light are presented in this subsection.

The time evolution of the system prepared in the excited state $|1\rangle$ (for this state notation see Fig. 4.3) with no couplings present is shown in Fig. 4.7. The time scale in the calculations is set in the units of the inverse relaxation rate γ. In all simulations, the decoherence rate G is considered to be equal to 0.0001γ, which is comparable with the decoherence rate value obtained from the Eq. 3.3.

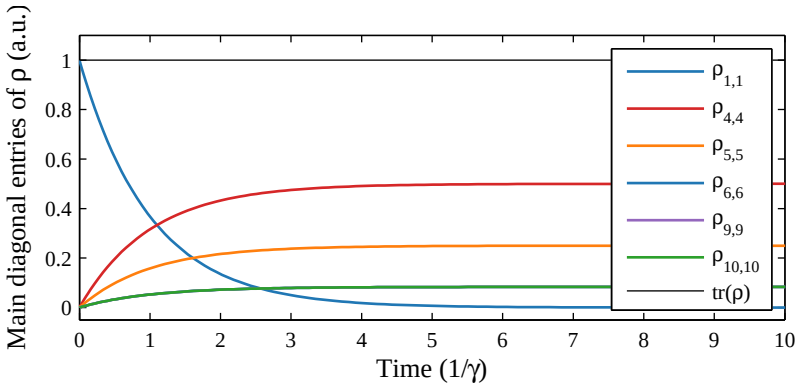

Figure 4.7: Spontaneous decay of the excited state $|1\rangle$ with the decay rate γ. The population of the state $|1\rangle$ can decay to particular ground states and only the evolution of their respective diagonal density matrix elements is shown here.

Evidently, for the initial conditions $\rho_{1,1}(t=0) = 1$ and $\Omega_C = \Omega_{S1,2} = 0$, the excited state $|1\rangle$ decays at the time rate $\tau = \gamma^{-1}$, as theoretically expected. The black line in Fig. 4.7 represents the trace of the density matrix ρ. As predicted, it is equal to unity during the time evolution of the system.

The population transfer between the Zeeman states of one hyperfine ground state (Fig. 4.8) is also simulated by setting the total population into the state $|9\rangle$ ($\rho_{9,9}(t=0) = 1$) and introducing the RF coupling B_{RF} of the Zeeman ground states as:

$$B_{\mathrm{RF}} = \Omega_{\mathrm{RF}} \cos \omega_{\mathrm{RF}} t \cdot e^{-i(B_Z+\delta)t}, \tag{4.12}$$

where Ω_{RF} is the Rabi frequency of the RF field, ω_{RF} the RF frequency, B_Z is the size of the Zeeman splitting, and δ two-photon detuning. It should be noted, that hyperfine ground states $5S_{1/2}F = 1$ and $5S_{1/2}F = 2$ have the same absolute value of the Zeeman splitting and therefore, the RF field couples the Zeeman states of both hyperfine ground levels. Compared to the optical couplings, the rotating-wave approximation for the RF

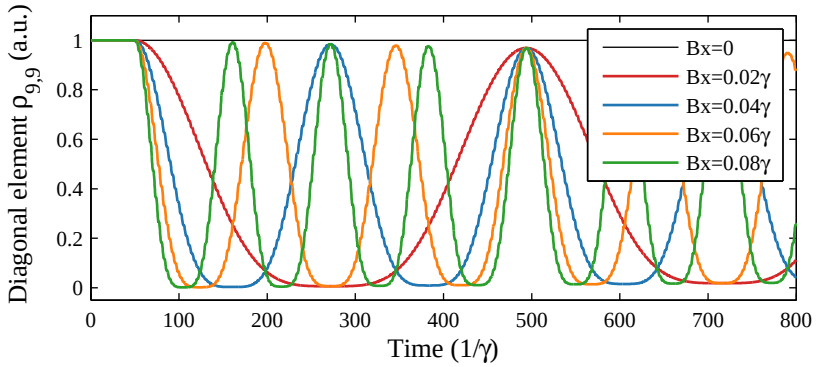

Figure 4.8: Time evolution of the density matrix element $\rho_{9,9}$ describing changes in the population of the state $|9\rangle$ for different RF excitation amplitudes. Both the size of the Zeeman splitting ω_Z and RF frequency ω_{RF} are set to γ.

interaction cannot be applied, since the counter-rotating terms are not negligible. Fig. 4.8 shows the simulated population transfer among the Zeeman ground states for different RF amplitudes.

The storage of light process for the eleven-level system and the optical control and signal field couplings is modeled as well (blue solid curve in Fig. 4.9). Since the signal field Ω_{S1} couples the states $|2\rangle$ and $|11\rangle$, the time evolution of the imaginary part of the non-diagonal element $\rho_{2,11}$ is of interest here. In the beginning, the system is prepared into the dark state, leading to the vanishing polarization. Then by simultaneous switching off of the control and signal field, the photonic state of the signal field is mapped on to the spin coherences for a certain period of time (denoted by vertical black lines in Fig. 4.9). Turning only the control field on causes the oscillation of the polarization, which leads to an emission of the signal field light with an intensity depending on the amplitude of the oscillating polarization.

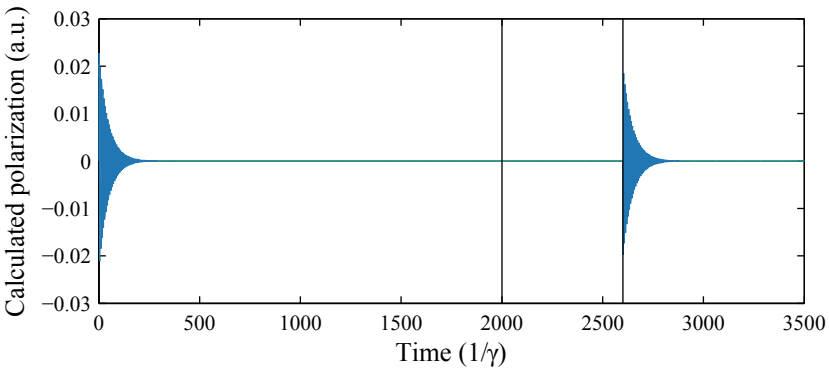

Figure 4.9: Simulation of the storage of light process. The Rabi frequencies of the control and signal fields are $\Omega_{\mathrm{C}} = 2\gamma$ and $\Omega_{\mathrm{S1}} = 0.5\gamma$, respectively. The second signal field is set to zero intensity ($\Omega_{\mathrm{S2}} = 0$) and the expected polarization on its transition is also equal to zero (green solid line).

4.2 Experimental results

4.2.1 Influence of RF excitation on stored light

After the action of the RF field on the dark state in the Λ-configuration has already been studied and the separation of two signal field components is enabled in the detection setup, the behavior of the stopped polariton under the influence of the RF excitation can be investigated. For this measurements, only one signal field component is stored and the RF field is applied during the storage time (experimental pulse sequence is shown in Fig. 4.10).

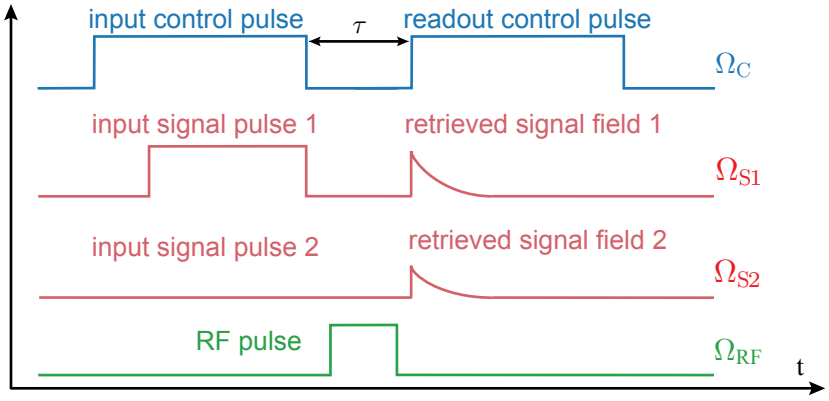

Figure 4.10: Pulse sequence used for testing influence of RF excitation on stored light. Only one signal field component is stored, while the RF pulse is applied during the storage time τ.

The RF field transfers the population trapped in the dark state, here in the Zeeman substate $|F = 1, m_F = 1\rangle$, to the Zeeman state $|F = 1, m_F = -1\rangle$ of the same hyperfine manifold, causing at same time also the retrieval of the second field component (Fig. 4.10). Both retrieved signal fields are monitored on the spectrum analyzer at their respective AOM modulation frequencies.

A typical measurement of the amplitude of the reaccelerated signal fields as a function of the different RF amplitudes is shown in Fig. 4.11. An RF frequency pulse of a 9 μs duration length and a 3 μs delay to the falling edge of the optical pulses is irradiated during the storage time of 15 μs. Obviously, the amplitude of the stored signal field (orange dots in Fig. 4.11) is reduced under the influence of the RF field, causing the appearance of the second signal field (blue dots in Fig. 4.11). The frequency of the RF pulse matches the value of the Zeeman splitting of 1.2 MHz. Optical light powers for the control and signal field are set to 300 μW and 130 μW. The RF amplitude is considered in the units of the current applied through the RF coils. Although the experimentally obtained data show limited contrast (the retrieved amplitude of the second signal field is by a factor of 25 smaller), the Rabi-like oscillation pattern between two signal field components is observable.

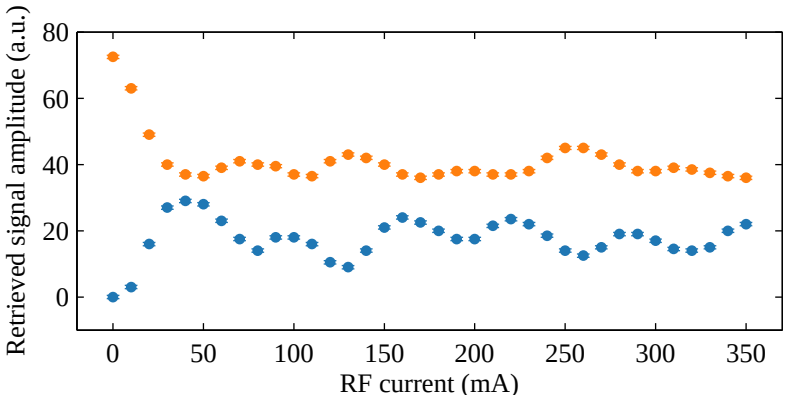

Figure 4.11: Retrieved amplitude of the stored signal field components versus the RF current. Although only one signal field is being stored (orange dots), the RF field induces the retrieval of the second non-applied signal field (blue dots), causing a Rabi-like oscillations with a limited contrast between the retrieved signal field components. To compare the amplitudes of the detected signal fields, the amplitude of the second signal field had to be magnified by a factor of 25.

A similar oscillatory behavior, again with a limited contrast of the retrieved signal light is observed for the RF pulses of the different duration lengths (Fig. 4.12). Again, only one signal field of optical power of 200 μW is stored for 15 μs (orange dots in Fig. 4.12). As in the previous case, the RF pulse excitation induces the rise of the second signal field (blue dots in Fig. 4.12).

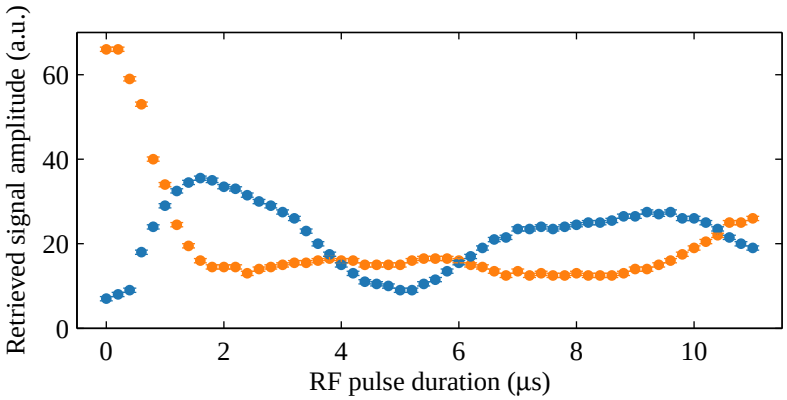

Figure 4.12: Retrieved amplitude of the stored signal field components versus the RF pulse duration. The RF field induces the retrieval of the non-applied signal field (blue dots), reducing in parallel the amplitude of the originally stored signal field component (orange dots). The RF current is kept constant at 230 mA and the control field has 500 μW of optical power.

The behavior of the stored light field is further examined by comparing the retrieved amplitudes of the induced second signal field component for two different RF pulse lengths, scanning at the same time the RF power (Fig. 4.13). For the same set of the experimental parameters, the RF pulse of duration of 6 μs (red dots in Fig. 4.13) and 9 μs (blue dots

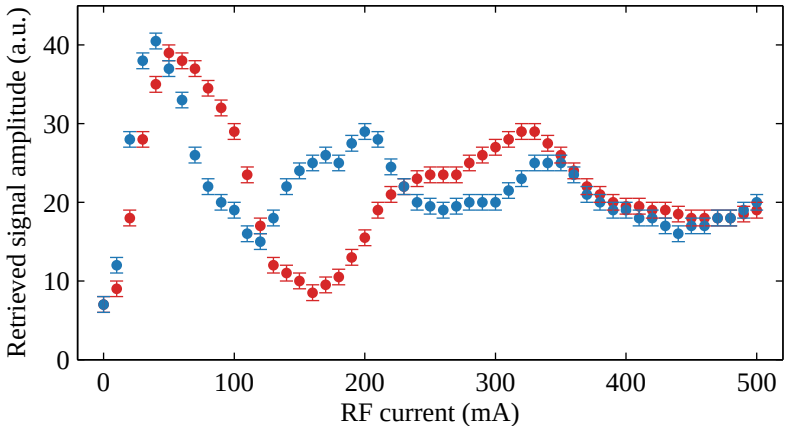

Figure 4.13: Amplitude of the retrieved signal field for 6 μs (red dots) and 9 μs (blue dots) long RF pulse. The measured data points correspond to the population of the RF induced polariton component as a function of the different RF amplitudes. The oscillation period is longer for the shorter RF pulse. The error bars correspond to the estimated measurement uncertainty of the retrieved signal amplitude.

in Fig. 4.13) is applied during the storage time. The increased oscillation period for the 6 μs RF pulse can clearly be observed, which confirms the Rabi-like oscillatory population transfer despite the limited contrast of the recorded amplitudes.

Moreover, a clear RF resonance is observable when the frequency of the RF field excitation is scanned during the storage time of 15 μs (Fig. 4.14). A 9 μs long, frequency variable RF pulse induces the population transfer among Zeeman ground states, which is detected through the initially non-present, restored second signal field component. Despite of the very small amplitudes of the RF induced restored light field, it can be concluded from the measurements performed on the stopped polaritons that distinguishing between the two polariton components of the tripod DSP is possible.

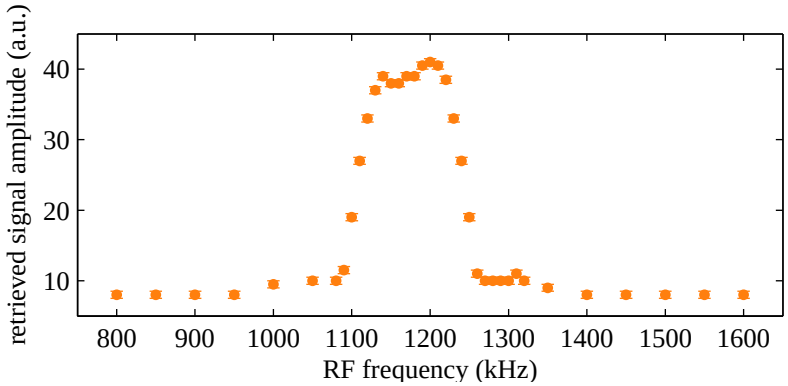

Figure 4.14: Radio-frequency resonance, observable as a rise of the amplitude of the stored light at the frequency of the non-used signal field component. The frequency of the RF pulse is scanned around the value of the Zeeman splitting of 1.2 MHz, while its amplitude is fixed at 46 mA.

4.2.2 RF spectroscopy of moving polaritons

Although the population transfer between the two states of the stationary polariton is detectable, it cannot be claimed yet that an RF spectroscopy experiment on dark state polariton has been performed. For stationary polaritons, only the atomic component of the polariton is present and the RF excitation of the system resembles usual atomic radio-frequency spectroscopy, where the prepared atomic coherences are manipulated. Therefore, a transition between the internal states of the moving polariton has to be realized.

For such an experiment, as in the previous measurements, the amplitude of the restored light is used to read out the desired information, with a difference that the RF pulse is irradiated during the presence of the optical control and two signal fields, which ensure the existence of the slowly moving polariton. Also, the two dark polariton modes are initially prepared with a certain population difference by applying one of the signal fields for a shorter period of time (see Fig. 4.15).

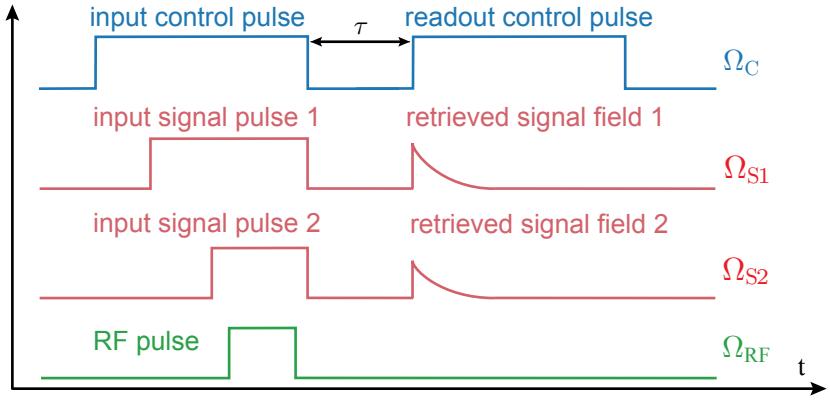

Figure 4.15: Pulsed sequence used in RF spectroscopy of moving polaritons. The RF field is irradiated during the presence of optical couplings. The duration of the two signal field pulses is different in order to prepare a population difference between two polariton components.

The signal fields of the same optical power of 150 μW are stored for 6 μs and afterwards, resolved in the heterodyne beat detection. The amplitude of the stored signal fields is recorded on the spectrum analyzer as a function of the applied RF pulse length (see Fig. 4.16). The initially high-populated internal state of the DSP (red dots in Fig. 4.16) evidently loses its population with the increased duration of the RF pulse, whereas the originally low-populated DSP state gains population for longer RF pulses (blue dots in Fig. 4.16).

A comparable behavior is observable when the frequency of the RF field is varied under the same experimental conditions. For an RF pulse of duration of a 13 μs and a constant RF current of 46 mA, a depopulation of the initially high-populated internal state is measured (red dots in Fig. 4.17). At the same time, a peak in the intensity of the restored

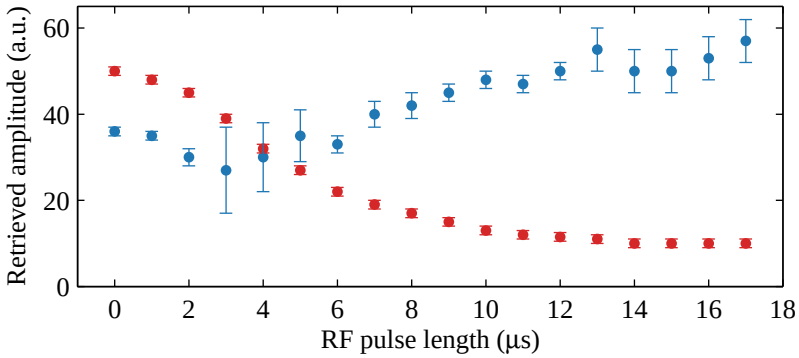

Figure 4.16: Population transfer for a moving dark state polariton as a function of the RF pulse duration. Retrieved amplitude of the initially high-populated polariton component is indicated by red dots, whereas blue dots represent the second polariton component. The error bars correspond to the estimated measurement uncertainty of the retrieved signal amplitude.

light was detected for the low-populated second field component (blue dots in Fig. 4.17). This indicates population transfer between the internal states of the moving polariton, at the frequency of the Zeeman splitting (1.2 MHz). On the other hand, the contrast of the experimental data is limited.

So far, all measurements indicate that the representation of the dark state polariton in the tripod scheme as quasi-particle with the internal state structure is valid. The additional theoretical confirmation of the experimental findings is desirable and therefore, the behavior of the eleven-level atomic system subjected to the optical and RF couplings

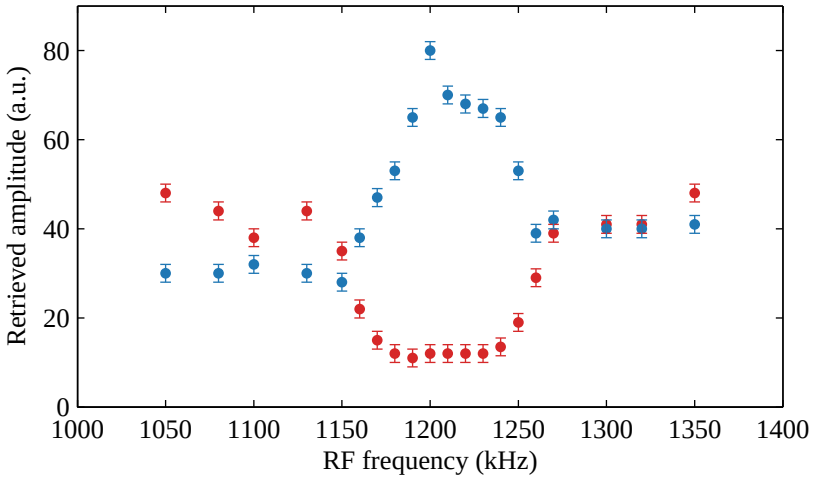

Figure 4.17: Amplitude of the retrieved signal fields versus the frequency of the irradiated fields shows a spectroscopic measurement on moving dark state polaritons. The population of one polariton component (red dots) is transfered to the other (blue dots) at the resonance RF frequency transition. The error bars indicate the estimated measurement uncertainty of the retrieved signal amplitude.

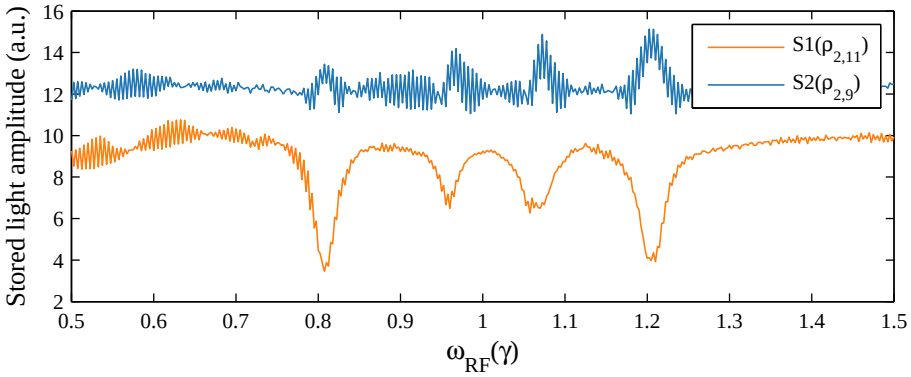

Figure 4.18: Calculated amplitude of the retrieved light fields versus frequency of the RF field. Orange and blue lines denote the amplitudes of the two restored signal fields corresponding to the mean values of their respective non-diagonal elements.

is simulated. The initial calculation results corresponded well with the expectations (as explained in Sec. 4.1.3). However, current calculations predict transition between the two polariton components (blue and orange solid lines in Fig. 4.18) only for the parameters that are experimentally not available, as the RF Rabi frequency Ω_{RF}, which is several orders higher than experimentally used one. The amplitude of the stored light is calculated as the mean value of the absolute imaginary part of the corresponding off-diagonal density matrix element, after the storage period. Moreover, for the size of the Zeeman splitting set to $B_{\mathrm{Z}} = \gamma$, the transition between the two dark states occurs at the RF frequencies ω_{RF} different from γ (see Fig. 4.18).

This calculation result is obtainable only when the interaction of the RF field with the hyperfine ground state $5S_{1/2}$ $F = 2$ is considered as a non-existing, for all other cases the calculations show no transitions between the dark polariton modes. The reason for this is understood as the RF field being also expected to cause transitions between Zeeman states of the $F = 2$ manifold, i.e. not only between the desired Zeeman components of the F=1 manifold. Due to the complexity of the experimentally used system, more careful theoretical considerations are needed to achieve better agreement with the measurement results.

The possibility of achieving the first radio-frequency spectroscopic measurement on a two level dark state polariton has been considered. The experimental demonstration of a transition between two internal polariton states would confirm particle-like properties of this quasi-particles. The two state dark polariton is realized in hot rubidium atoms in a tripod scheme and probed by an radio-frequency field.

The measurements, performed on both stationary and moving polaritons, give a strong indication that a population transfer between the internal polariton states is possible. However, the absolute detectable value of the transfered population is quite small and requires a reliable optimization of the experimental setup. A theoretical model of the

experimentally used interaction system simulated well the basic properties of the eleven-level EIT medium, yet its theoretical predictions regarding the RF-switching between the two polariton modes do not fully correspond to the experimental findings. Therefore, further improvements of the theoretical model as well as the experimental apparatus are desirable.

5 Aharonov-Casher effect for dark state polaritons

If two charged particles are taken around a solenoid they will experience different influence of the electromagnetic potential that can be measured as a phase shift between them. This is the well-know prediction of the Aharonov-Bohm effect [85]. A similar topological effect considering neutral particles with a finite magnetic dipole moment that exhibit phase difference after being taken round the line of charge and recombined is called the Aharonov-Casher (AC) effect [86] (see Fig. 5.1(a)). The main topic of this chapter is a prospective measurement of Aharonov-Casher effect for dark state polaritons (DSPs).

It was already suggested in earlier work concerning Stern-Gerlach experiment for slow light [56] that the DSP possesses an effective non-zero magnetic dipole moment $\vec{\mu}_0$. However, two dark polaritons cannot simply be taken round the line of charge and therefore, a different geometrical configuration is needed. For a detection of the AC effect, it is equivalent having a beam of neutral particles passing through a homogeneous electrostatic field $\vec{E}$ in a straight line [87,88], as shown in Fig. 5.1(b), which was already implemented in the earlier measurements of the AC effect in thallium fluoride molecules [89,90]. Besides this, the Aharonov-Casher effect was also observed for neutrons [91], calcium and rubidium atoms [92,93]. More recently, the AC effect was observed in the ring structures fabricated from quantum wells [94] and for an electron spin in arrays of two-dimensional electron gas rings [95].

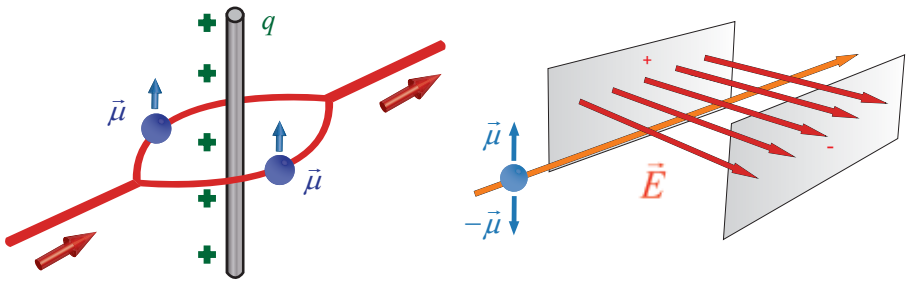

(a) (b)

Figure 5.1: (a) Schematic layout for the interferometric measurement of the Aharonov-Casher effect. Two neutral particles with a magnetic dipole moment are recombined after being traversed round a line of charge. (b) Equivalent geometrical scheme for the detection of Aharonov-Casher effect in a homogeneous electric filed for particles with opposite magnetic dipole moment.

Extensive work on this topic in our group was done in the framework of Leon Karpas PhD thesis, yet with no unambiguous answer on the question whether is possible to achieve the first observation of the topological phase for the quasiparticles [65]. The inconclusive results asked for a somewhat different experimental approach, which is discussed in the following subsections. First, a theory for the AC effect for the dark state polaritons is given, followed by the experimental setup and its scope.

5.1 Theory of the Aharonov-Casher effect for the DSP

One way of experimentally detecting the AC phase is to coherently split the beam of neutral particles in two beams, traverse them round a line of charge and after recombining them, as shown in Fig. 5.1(a), perform the interferometric measurement. The measured phase difference does not depend on the choice of the path enclosing the line of charge and it can be defined as:

$$\Delta\varphi_{\mathrm{AC}} = \frac{1}{\hbar c^2}\oint_C \vec{\mu}_0 \times \vec{E}(\vec{r})\, d\vec{r}. \tag{5.1}$$

If this effect is considered in the rest frame of the particle [96], then the electric field moves producing a magnetic field according to Lorentz transformation. The energy of the particle can then be calculated from:

$$U(\vec{r}) = -\vec{\mu}_0\vec{B}(\vec{r}) = -\frac{1}{c^2}\vec{\mu}_0 \cdot (\vec{v} \times \vec{E}(\vec{r})), \tag{5.2}$$

where $\vec{v}$ is the velocity of the field. In the laboratory reference frame the moving particle now gives rise to the electric dipole moment $\vec{p}_0$ and the potential energy of the particle is:

$$U(\vec{r}) = -\vec{p}_0\vec{E}(\vec{r}) = -\frac{1}{c^2}(\vec{v} \times \vec{\mu}_0) \cdot \vec{E}(\vec{r}). \tag{5.3}$$

By comparing Eq. 5.2 and 5.3, it becomes obvious that the AC phase shift is independent of the velocity of the particle. In the case of DSPs this conclusion does not hold, which imposes particular demands in the later realization of the experimental setup. Before the behavior of the DSP in different reference frames can be analyzed, the effective magnetic dipole moment for the DSP shoud be introduced. It was pointed out by Karpa [56, 65] that the effective magnetic dipole moment of the DSP can be derived from the difference of the spin expectation values $\hat{S}_Z$ of one-polariton state and the polariton vacuum in a following way:

$$\begin{aligned}\vec{\mu}_{pol} &= \vec{e}_x\mu_B\Big({}_p\langle 1|\hat{S}_Z|1\rangle_p - {}_p\langle 0|\hat{S}_Z|0\rangle_p\Big)\\ &= \vec{e}_x\Delta m_F g_F \mu_B \sin^2(\theta),\end{aligned} \tag{5.4}$$

where $\vec{e}_x$ presents the unity vector of the quantization axis, g_F the hyperfine g-factor equal to 1/2 for the used ^{87}Rb transition, and $\sin(\theta)$ is the mixing angle defined in the Eq. 2.8. For a tripod-level scheme, in the case where $v_{gr} \ll c$ and $\sin^2(\theta) \approx 1$, two orthogonal components of the dark states have magnetic dipole moment $\mu_{pol} = \pm\frac{1}{2}\Delta m_F \mu_B$. Now, in the rest frame of the DSP, atoms move with the velocity $-\vec{v}_{gr}$ and acquire besides the magnetic dipole moment also the electric dipole moment. In DSP reference frame the electric dipole moment of DSP is:

$$\vec{p}_{pol} = -\frac{1}{c}(\vec{v}_{gr} \times \vec{\mu}_{pol}), \tag{5.5}$$

Also, in the rest frame of the polariton, the electrical field moves creating the magnetic field $\vec{B}(\vec{r}) = -\frac{1}{c^2}\vec{v}_{gr} \times \vec{E}(\vec{r})$. From the previous expressions the potential energy of the

polariton can be calculated:

$$\begin{aligned} U(\vec{r}) &= -\vec{\mu}_{pol}\vec{B}(\vec{r}) - \vec{p}_{pol}\vec{E}(\vec{r}) \\ &= -\frac{1}{c}\vec{\mu}_{pol}\cdot(\vec{v}_{gr}\times\vec{E}(\vec{r})) + \frac{1}{c}(\vec{v}_{gr}\times\vec{\mu}_{pol})\cdot\vec{E}(\vec{r}) = 0. \end{aligned} \tag{5.6}$$

Evidently, for the non-moving medium contributions from the magnetic and electric dipole moments neutralize themselves in the electrostatic field leading to the non-existing Aharonov-Casher phase. This implies that the spin component of the DSP has to be moving to detect the AC phase.

In the case where atoms of the ensemble move with the velocity $\vec{v}_{at} = -\vec{v}_{gr}$, the rest frame of DSP and the laboratory frame would coincide and the polariton potential energy would in turn become $U(\vec{r}) = -\vec{p}_{pol}\vec{E}(\vec{r})$. The acquired phase difference is then:

$$\begin{aligned} \Delta\varphi(-\vec{v}_{gr}) &= \frac{1}{\hbar}\int U(\vec{r})\,dt = \frac{1}{\hbar c^2}\int(\vec{v}_{gr}\times\vec{\mu}_{pol})\cdot\vec{E}(\vec{r})\,dt \\ &= \frac{1}{\hbar c^2}\oint_C\left(\vec{\mu}_{pol}\times\vec{E}(\vec{r})\right)\cdot d\vec{r}, \end{aligned} \tag{5.7}$$

which is identical to the Eq. 5.1. This proves that in order to detect Aharonov-Casher phase for DSP, it is necessary to work with a moving medium.

The expected phase difference between the signal fields traversing the glass cell of the length L, placed in the homogeneous electric field $\vec{E}$, can be defined as [97]:

$$|\Delta\varphi_{AC}| = \frac{1}{\hbar c^2}\mu_B|\vec{E}|L\Big(\frac{v_{at}}{v_{gr}}\Big), \tag{5.8}$$

where factor $\left(\frac{v_{at}}{v_g}\right)$ is added to account for the general case of the atoms moving with the velocity different from the velocity of the polations.

5.2 Experimental setup for the Aharonov-Casher effect

As mentioned earlier, the geometrical configuration used in a search for the AC phase differs from the one proposed originally by Aharonov and Casher (see Fig. 5.1(b)). This approach requires particles with the linear superposition of antiparallel magnetic dipole moments, which is here realized in the tripod-level configuration (Fig. 5.2) by creating a quasiparticle with two orthogonal internal states (see section 4.1). After passing through the homogeneous electric field (Fig. 5.1(b)), the dark polaritons should acquire certain phase difference that is imprinted on the signal fields Ω_{S1} and Ω_{S2}. Since optical signal fields carry the phase information, a detection of their phase is going to be here the main measurement tool.

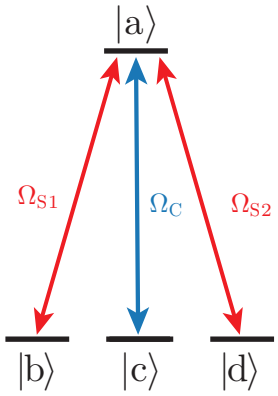

Figure 5.2: Simplified tripod level scheme consisting of three ground states $|b\rangle$, $|c\rangle$, $|d\rangle$ coupled to excited state $|a\rangle$ with optical fields Ω_{S1}, Ω_C, and Ω_{S2}.

Nevertheless, an important issue has to be solved first concerning the design of the AC experimental setup. Namely, the setup has to allow for the existence of the moving medium. Since hot atomic rubidium gas is used as a working medium, one cannot move the atoms in a particular direction to achieve the desired medium velocity. Thus, a way to select particular atomic velocity classes that are close to the polariton group velocity $\vec{v}_{gr}$ has to be found. One possible way of choosing a different atomic velocity class is to simultaneously vary the one-photon detuning Δ of all participating optical couplings and select the atoms with the velocity $v_{at} = \frac{\Delta}{\nu_C} c$. This is the method applied in [65], with the downside that detunings of only several tens of MHz were achievable, limiting the selectivity of the velocity classes to $\pm$ 50 m/s. For larger detunings, one would leave the EIT transparency window and consequently, the dark resonances would vanish. In the framework of this thesis, different approaches were investigated in order to achieve selectivity of the velocity classes. One of the first ideas was to select velocity classes by working in the EIT environment with counterpropagating control and signal beams [98]. Although the control beam with several tens of mW of optical power generated by tapered amplifier was applied, the EIT operating conditions could not be reached and this method was abandoned.

The selectivity of the atomic velocity classes is obtained eventually by adding a repumping

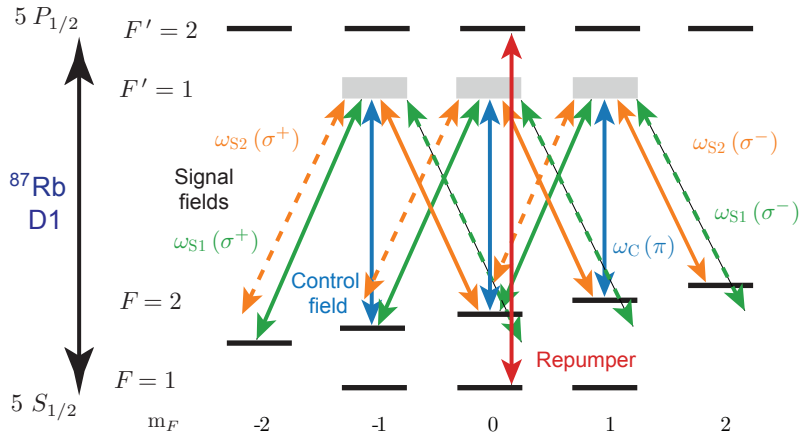

Figure 5.3: Experimentally used energy level scheme on rubidium D1 transition. The tripod-level scheme is realized with the σ^+-polarization component of the signal field 1 (green solid lines), the π-polarized control field (blue solid lines), and the σ^--polarization component of the signal field 2 (orange solid lines). The dashed orange and green lines represent the off-resonant components of the two signal fields.

laser beam to a tripod-level scheme. For the experimental realization of the tripod-level scheme, transition $5S_{1/2}$ $F = 2 \rightarrow 5P_{1/2}$ $F' = 1$ is used (see Fig. 5.3). Adding the repumping beam on the hyperfine transition $5S_{1/2}$ $F = 1 \rightarrow 5P_{1/2}$ $F' = 2$ increases the number of atoms of a particular velocity class, which interact with the laser fields without increasing the atomic density (Fig. 5.4(a)). The black solid line in Fig. 5.4(a) shows the transmission of the signal field without the presence of the repumper beam. In the system with the laser repumper, the group velocity of a slow light pulse and the EIT linewidth are reduced with the trade-off of a diminished EIT contrast [99]. Without repumping the signal light pulse is slowed down to approximately 22 kms^{-1} (blue line Fig. 5.4(b)), whereas with the repumper the group velocity becomes 16 kms^{-1} (orange line Fig. 5.4(b)).

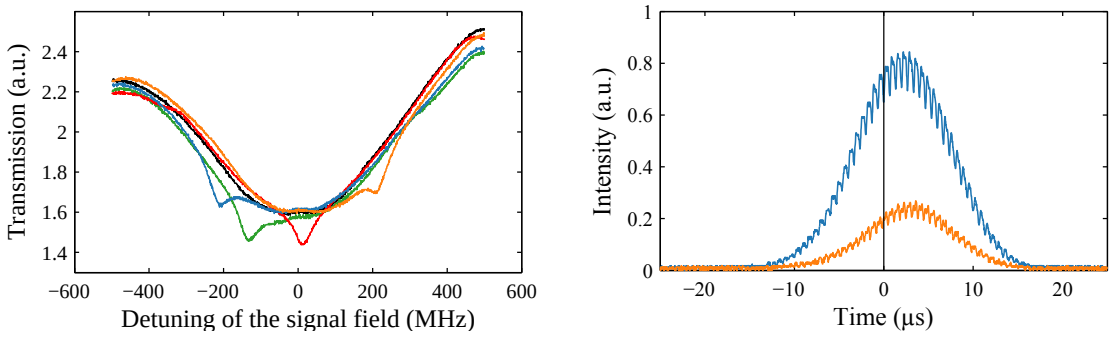

(a) (b)

Figure 5.4: (a) Transmission of the signal field without the repumper beam (black solid line) and with the repumper beam frequency locked at different positions. (b) The time delay of a slow light pulse is increased with repumping from 2.2 μs (blue line) to 3 μs (orange line).

With more available repumped atoms the transmission drops and therefore the operating temperature of the rubidium apparatus is set to 50°C.

The rubidium atomic vapour apparatus and the optical setup differ in several points from the setup described in the subsections 3.3 and 3.1. Firstly, due to the constant change of the atomic impulse in the rubidium buffer gas cells and therefore the lack of the ability to select distinct velocity class, one needs to work with the glass cells filled only with rubidium, i.e. no buffer gas can be used. The rubidium cell needed to be placed inside the electrostatic field in such a way, that the relation $(\vec{\mu}_{pol} \times \vec{E}(\vec{r})) \cdot d\vec{r} = (\vec{\mu}_{pol} \times \vec{E}(\vec{r})) \cdot \vec{v}_{gr} dt \neq 0$ is satisfied, realizing that the maximal measurable phase difference is accomplished when the vectors $\vec{\mu}_{pol}, \vec{E}$ and $\vec{v}_{gr}$ are orthogonal to each other. This is done by placing the cell between two aluminum plates mimicking the plate capacitor (Fig. 5.5). To each aluminum plate a voltage up to ± 8 kV is applied using a high voltage power supply (Heinziger PNC 10000 - 20).

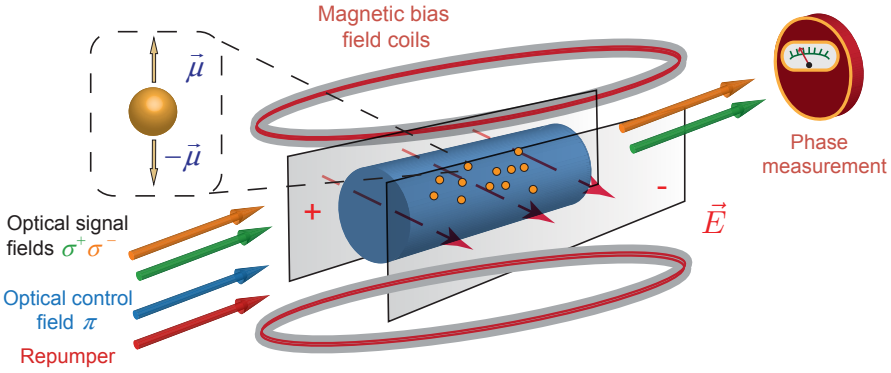

Figure 5.5: Scheme of the experimental setup used for investigating the Aharonov-Casher effect for dark state polaritons. Co-propagating optical fields traverse the rubidium cell, which is placed inside a capacitor. A pair of coils produces a transversal magnetic bias field.

The π-polarized optical control field, together with the two signal fields, forms the tripod-like level scheme in the Zeeman configuration (see Fig. 5.3). To prepare two optical signal fields ω_{S1} and ω_{S2} for the tripod interaction scheme, the same acousto-optic modulator is driven with two different carrier frequencies. In this way, the optical signal beam contains two frequency components, shifted for the corresponding value of the Zeeman splitting $\pm\Delta\omega = g_F \mu_B B_0$. The signal beam is polarized orthogonally to the applied transversal magnetic bias field $\vec{B}_0$ and its polarization can bee seen as a linear combination of two orthogonal circular polarizations σ^+ and σ^-. With the right choice of the modulation frequencies, only the σ^+ component of the signal field with the frequency ω_{S1} is resonant with the tripod-level scheme (green solid lines in Fig. 5.3). Correspondingly, only the σ^- component of the signal field with the frequency ω_{S2} is resonant with the created level scheme (orange solid lines in Fig. 5.3).

Obviously, both signal fields possess non-resonant polarization components. The resonant components of the signal fields participate in the creation of the DSP with two internal

dark states, whereas the off-resonant components become absorbed by the medium. This non-resonant interaction contributes to the rise of decoherence processes and to the decrease of the EIT contrast. It has to be noted here that for this, the atoms are prepared in a state that strictly speaking cannot be called a pure dark state. In order to strongly suppress the influence of the off-resonant mechanisms one could work with the higher optical densities by increasing the temperature of the rubidium system. Unfortunately, this is not applicable here, due to the usage of the repumping as an atomic velocity selection tool and the accompanying vanishing of the EIT resonances for the high temperatures.

The experimental setup presented here, compared with the one used in [65], enables the selection of the atomic velocity classes across the whole Doppler broadened profile without detuning any of the optical couplings contributing to the creation of the dark state polaritons. Also the magnetic field defining the quantization axis in the system is produced with the help of the low noise current source and the available intensity of the electric field is increased several times.

5.3 Detection of the Aharonov-Casher effect

In the detection of the phase difference between two signal fields and with that the Aharonov-Casher phase, a beat note detection procedure is used (Sec. 3.4). Two different methods are available experimentally, a detection of the absolute and the relative optical phase. With the heterodyne beat detection, two signal fields ω_{S1} and ω_{S2} can be isolated in the frequency space and then their absolute phases can be compared on a phase detector (PD). To this end, a home-build spectrum analyzer is constructed (Fig. 5.6), whose output is fed to the phase detector and then averaged on a lock-in amplifier. The drawback of this method is that the noise of the reference oscillator (here the zeroth AOM order) obviously influences the final sensitivity of the phase measurement. This can be avoided in the relative phase detection, where the phase of the beat note between the two signal fields is compared with the phase of a stable reference oscillating on the beat frequency. However, for this method one cannot gauge the local oscillator.

Several fingerprints are expected in the experimental AC phase detection. For instance, to prove the existence of the Aharonov-Casher effect for the DSP, one needs to show the linear dependence of the measured phase difference with the applied electric field according to the relation 5.8. It is also expected that the AC phase changes its sign for the atomic velocity classes of the opposite sign. Hence, scanning of the repumper frequency across the Doppler profile should give the linear behavior of the AC phase with the velocity of the atoms. For the experimentally available parameters, the maximal achievable Aharonov-Casher phase delay can be estimated from the Eq. 5.8. In the atomic ensemble heated to 50°C, the group velocity of 15 km/s can be achieved and the maximal experimentally observable phase difference can then be estimated to be $\Delta\varphi_{AC} \approx 2 \times 10^{-5}$ rad.

The absolute phase detection method makes use of the beating between the signal fields ω_{S1} and ω_{S2} and the unmodulated beam passing through the AOM used for the creation of the signal fields. The beat note signal obtained on a fast photodiode contains modulation

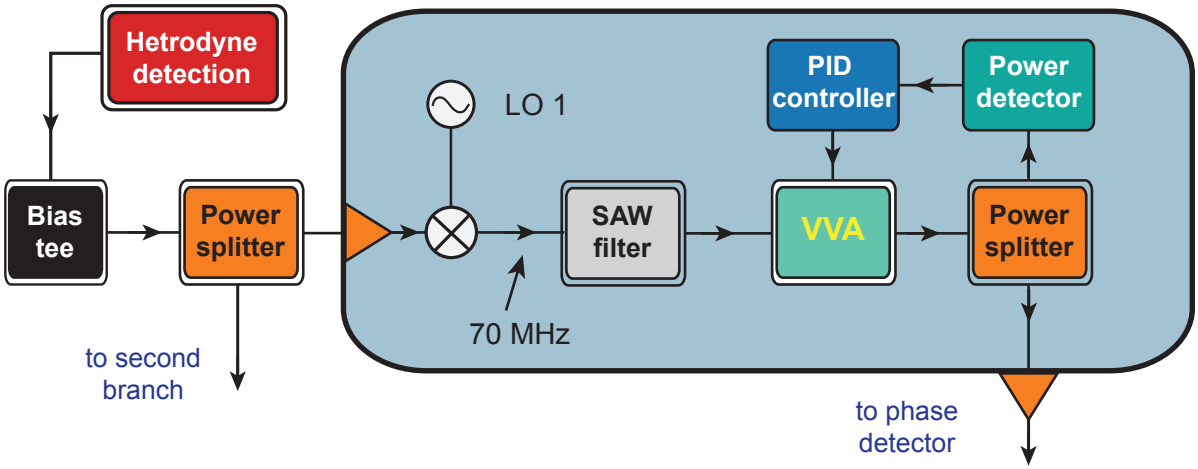

Figure 5.6: Block diagram of absolute phase detection of a single field. The detected beat signal is sent to the RF mixer, after being split in two parts. A local oscillator is used to mix down only one signal field component to the operating frequency of the narrow SAW filter. The signal is then actively stabilized and passed to phase detector.

frequencies of the two signal fields at 196.5 MHz and 199.5 MHz. Their difference of 3 MHz is chosen to match the double value of the corresponding Zeeman splitting. The RF signal is then isolated with a bias tee and after being amplified (Mini-Circuits ZFL-500LN), split in two parts on an RF power spitter (ZSC-2-1+) (see Fig. 5.6). The two outputs are fed to an RF input of separate RF mixers in order to shift the beat frequencies of the two signal fields to the same intermediate frequency of 70 MHz. Both signals are then passed through narrow bandpass filters with a FWHM of 30 kHz (Tai-Saw Technology TB0505). Since the evaluated AC phase is very small and the output of the PD sensitive on the signal power changes, the RF power of each branch has to be actively stabilized by feeding the signal to a voltage variable attenuator (VVA) and controlling its output (Fig. 5.7(a)). For example, the influence on the PD output of an amplitude modulation of 1% of one of the

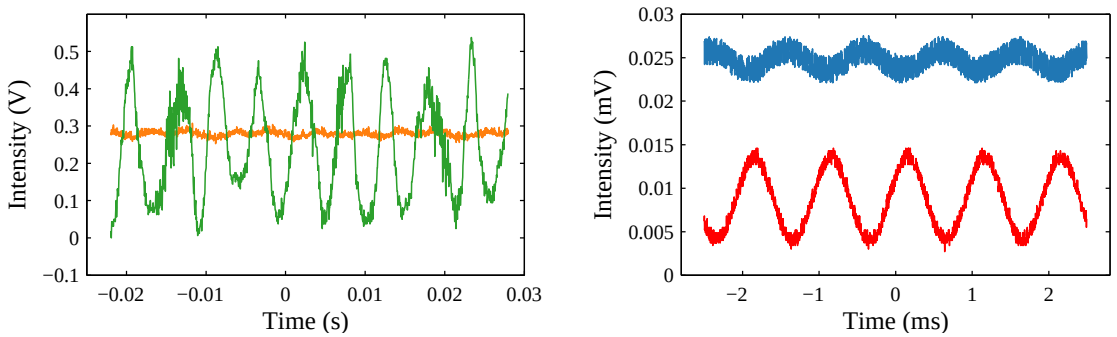

(a) (b)

Figure 5.7: (a) Intensity fluctuations of the RF signal with (orange line) and without (green line) active RF power stabilization. (b) Intensity fluctuations of the phase detector output for a 1% amplitude modulation (red line) and a 1° phase modulation (blue line) of the signal field.

signal fields (red line Fig. 5.7(b)) is comparable to the 1° phase modulation of the signal field (blue line Fig. 5.7(b)), with both modulations performed by frequency generator. Hence, part of the RF power is detected on an RF power detector (ZX47-60+) and from it passed to the PI-controller that modulates the output of the VVA (ZX73-2500). Such signals are then amplified and its phases are compared on the phase detector.

In both absolute and relative phase detection, two types of the phase detectors are used (Mini-Circuits ZRPD and Analog Devices AD-8302). Their DC output is filtered out and detected with the lock-in amplifier (Signal Recovery DSP 7265). The lock-in amplifier averages only the frequency components of the input signal that match its reference oscillator, which here corresponds to the switching of the polarity of the high voltage applied to the aluminum plates at the frequency $f_{HV} = 200$ Hz. The polarity on the capacitor plates is exchanged with the rectangular pulses fed to the high voltage switch (Behlke HTS 151-03-GSM) ensuring that for the duration of the pulse, plates have high voltage of a different sign.

Calibration measurements with two different phase detection methods are performed and compared. The calibration measurements for the relative phase detection, where only the beat note signal is compared with the reference signal without the EIT conditions, reveal the phase resolution of the 10^{-5} rad. Although this represents the necessary phase resolution for the measurement of the estimated AC phase, coupling the control and the repumper beam into the system introduces substantial intensity fluctuations in the detected signal reducing the signal-to-noise ratio. Therefore, no measurable phase changes are observable, either for the scan of the repumper frequency or for the scan of the electric field. For the comparison of the absolute phases of the two separate signal fields, the phase of one of them is modulated with the function generator. The detected signal on the lock-in amplifier corresponded to the phase sensitivity of only 10^{-4} rad. Despite the previously described efforts to increase the stability of the system and the usage of a linear current supply for all electronic devices, the intensity-to-phase noise conversion could not be reduced. For both detection methods, the separation of the optical control and the repumper fields from the signal fields before their detection on the photo-diode could increase the signal-to-noise ratio. It should be noted that with the careful optimization of the detection setup and the lock-in amplifier averaging, the detected phase changes are well below the operating threshold of the phase detectors.

Nevertheless, the calibration measurements set the upper boundary on the Aharonov-Casher phase for the dark state polaritons in the ensemble of the hot rubidium atoms. Following the calibration results, one can conclude that for the measurement of the AC phase the relative phase detection method is more favorable since it counteracts for the systematic phase noise disturbances.

The particle-like properties of the dark state polaritons have been investigated, particularly the behavior of the attributed effective magnetic dipole moment of the DSP in the presence of the homogeneous electric field. More precisely, the experimental evidence of the existence of the Aharonov-Casher phase effect for the polariton systems is searched for. The results, coming from the calibration measurements, determine the upper boundary for the experimentally detectable AC phase difference for the atomic rubidium gas system.

The experimental setup and the detection system give a method of determining the phase difference between two optical fields with the sensitivity of 10^{-5} rad, which is comparable to previous work [65]. Another possible way of detecting such phase delays could be achieved with a polarimetry measurements based on auto-balanced photodetection. Since the experimentally used interaction scheme does not provide the existence of the pure dark states, using the hyperfine level configuration with the two phase locked lasers in the future investigations of the AC phase for DSP is advisable.

6 Resonance Retrieval of Stored Coherence

In the following sections of this chapter, the eigenfrequency of the retrieved atomic coherence following initial storage of coherence is examined, inspired by light storage experiments in dark state media [29]. In previous works using light storage it was demonstrated that the difference frequency of the regenerated signal beam to the control beam used for storage oscillated at an atomic eigenfrequency [100, 101]. Apart from the described EIT systems, it is well known that atomic ground state coherences can be created also in an optical-radiofrequency double resonance configuration [102]. Here, a resonance retrieval of atomic coherence in an optical-radiofrequency double resonance experiment is going to be demonstrated. The experiment uses an atomic three-level system, and the setup is based on hot atomic rubidium vapour used for the storage. After the retrieval of the stored coherence, a beating that matches the energy difference between the two ground levels was observed. Within the experimental uncertainty, the observed beat frequency is insensitive to a wide range of variations of both the drive frequency ω_{RF} and the amplitude of the radiofrequency (RF) field. The observed effect is robust with respect to variations of the Rabi frequencies of both optical control and RF fields.

6.1 Theoretical and experimental results

For a simple model of the experimental method, an ensemble of three-level atoms is considered (as depicted in Fig. 6.1) with two stable ground states $|g_1\rangle$, $|g_2\rangle$ and one electronically excited state $|e\rangle$, which is spontaneously decaying. The transition between the states $|g_2\rangle$ and $|e\rangle$ is coupled coherently via the optical control laser field with Rabi frequency Ω_{C}, while the RF field at frequency ω_{RF} couples the ground levels $|g_1\rangle$ and $|g_2\rangle$. Without the presence of the RF coupling, the system is pumped into the ground state $|g_1\rangle$. Adding of the RF field coupling creates a coherence among ground levels and together with the simultaneous driving of the optical transition induces coherence between levels $|g_1\rangle$ and $|e\rangle$, that in turn produces a coherent optical signal field collinear with the control laser beam. During the RF excitation of the system, the generated signal field beats with the transmitted laser field at the frequency $\omega_{\mathrm{beat}} = \omega_{\mathrm{S}} - \omega_{\mathrm{C}} = \omega_{\mathrm{RF}}$. After the simultaneous switching off of the optical and RF excitation fields, and the later resonant retrieval of the stored coherence, the retrieved light beats at the difference frequency of the ground state levels $\omega_{\mathrm{beat}} = \omega_{\mathrm{S}} - \omega_{\mathrm{C}} = \omega_{g_1 e} - \omega_{g_2 e}$.

In the experimental apparatus (see Fig. 6.2), a grating stabilized diode laser is used as a source of the optical control beam. The diode laser is locked with dichroic atomic vapor laser lock procedure to the $5S_{1/2}\ F = 1 \rightarrow 5P_{1/2}\ F' = 1$ (see Fig. 6.3) hyperfine component of the rubidium D1 line near 795 nm. Its emission passes an acousto-optic modulator, is spatially filtered by a fiber, and then with linear polarization sent to a magnetically shielded 50 mm long rubidium buffer gas cell (see Sec. 3.1). The cell itself contains 1 Torr of xenon buffer gas and is heated up to 80°C, resulting in a rubidium atom number density of around $10^{12}\mathrm{cm}^{-3}$. To lift the degeneracy of the Zeeman sublevels of the $F = 1$ ground state, a magnetic bias field is applied in a direction parallel to the

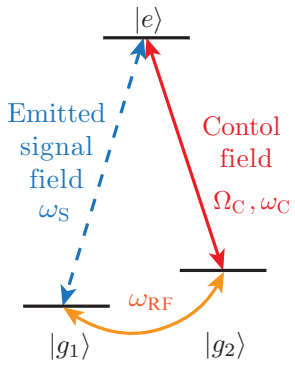

Figure 6.1: Simplified three-level scheme used for resonant retrieval of stored coherence. The levels $|g_2\rangle$ and $|e\rangle$ are coupled by a control field with the Rabi frequency Ω_C, while a RF field at frequency ω_{RF} couples the ground levels $|g_1\rangle$ and $|g_2\rangle$. After storage of the ground state coherence, an optical signal field can be generated with the difference of the optical fields oscillating at the (Raman) transition frequency between ground states $|g_1\rangle$ and $|g_2\rangle$.

control beam polarization.

The splitting between the adjacent Zeeman sublevels of the ground state is $g_F \mu_B B$, where μ_B is the Bohr magneton, and the hyperfine g_F factor equals 1/2. In the experimentally used level scheme, the ground state sublevels $|F = 1, m_F = 0\rangle$ and $|F = 1, m_F = \pm 1\rangle$ correspond to the states $|g_1\rangle$ and $|g_2\rangle$ of the three-level model presented in the Fig. 6.1 respectively, and $|F' = 1, m_F = \pm 1\rangle$ of the electromagnetically excited state to $|e\rangle$. The π-polarized optical field drives the transition $|F = 1, m_F = \pm 1\rangle$ to $|F' = 1, m_F = \pm 1\rangle$, whereas the generated signal beam is $\sigma^+ - \sigma^-$ polarized and tuned near the $|F' = 1, m_F = \pm 1\rangle$ to $|F = 1, m_F = 0\rangle$ transition. The RF field coherently couples the Zeeman states of the $5S_{1/2}, F = 1$ ground state manifold. This field is generated by a radio-frequency antenna mounted close to the rubidium cell, as explained in section 4.1.2. In the absence of a radiofrequency field, the linearly polarized control field pumps the atomic population into the $|F = 1, m_F = 0\rangle$ ground state sublevel. After leaving the rubidium cell, the control field and the generated signal field are projected onto the same

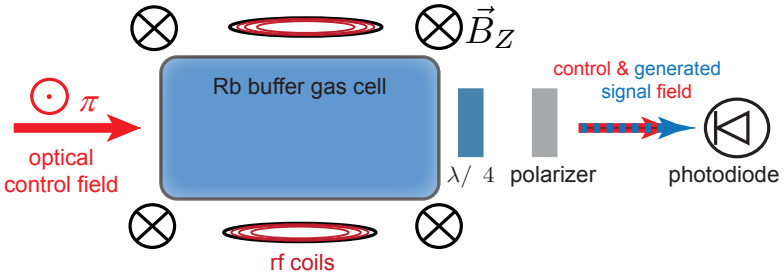

Figure 6.2: Scheme of the experimental setup used for resonant retrieval of stored atomic coherence.

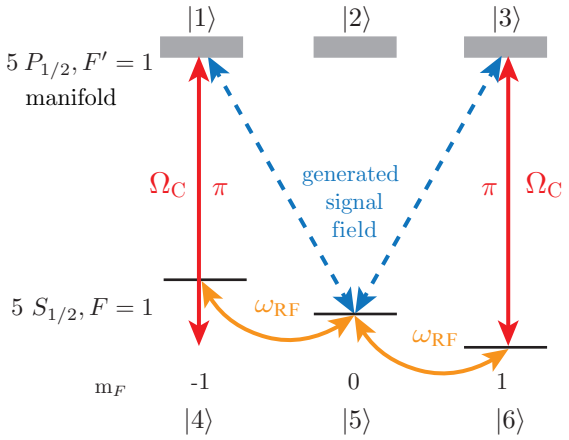

Figure 6.3: Full level scheme of the experimentally investigated Rb^{87} $F = 1 \rightarrow F' = 1$ transition, as also used in the numerical calculations. The solid blue and orange lines represent the transitions driven by the π-polarized optical control field and the RF field respectively. The dashed blue lines represent the coupling of the generated $\sigma^+ - \sigma^-$ polarized optical signal field.

polarization using a polarizer and the resulting beat signal between the two fields is detected using a fast photodiode. The amplitude of the detected beat signal can be adjusted by a $\lambda/4$ mounted wave plate in front of the polarizer.

The control laser power is on a 5 mm beam diameter typically set to 200 μW. The frequency of the applied radiofrequency is tuned to the Zeeman splitting between adjacent Zeeman sublevels near 1.2 MHz at the used level of the magnetic bias field, and the Rabi frequency of the RF field is approximately $\Omega_{RF}/2\pi = 5$ kHz. The experimental cycle, see Fig. 6.4, begins by initially activating the linearly polarized control laser beam, so that population is pumped into the $|F = 1, m_F = 0\rangle$ component of the electronic ground state. In addition, the resonant radiofrequency pulse is activated, which creates an atomic ground state coherence, after which the optical control field and the radiofrequency field are simultaneously turned off. After a 5 μs long period with no external driving fields applied, only the control field is reactivated, which retrieves the stored coherence and causes emission of a signal beam pulse [103]. This beam is generated by the coherence oscillating at the $|g_1\rangle$ to $|e\rangle$ transition of the simplified level scheme of Fig. 6.1, or $|F = 1, m_F = 0\rangle$ to $|F' = 1, m_F = \pm 1\rangle$ of the full level scheme (Fig. 6.3), and upon reactivating the control beam emission of a second optical beam collinear to the control beam is possible.

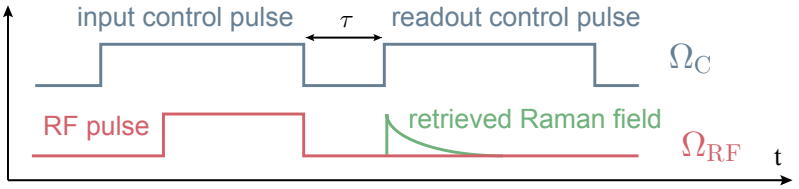

Figure 6.4: Experimentally used pulse sequence for the resonant retrieval of stored coherence.

The blue line in Fig. 6.5 shows typical experimental data for the observed beat signal between the control and the signal beam. Fig. 6.5 shows that a beat signal, as understood from emission of a signal field, is not only present during the retrieval of the coherence, but also during the preparation stage, where both the radiofrequency field and the control beam are active. As in that phase one deals with a driven system, it is expected that before the storage, the beat frequency will be determined by the frequency of the RF field, which in the presence of a finite detuning differs from the atomic eigenfrequency. The frequency of the detected beat, both during the RF pulse and after the coherent retrieval, is determined by fitting the signal with a sinusoidal function.

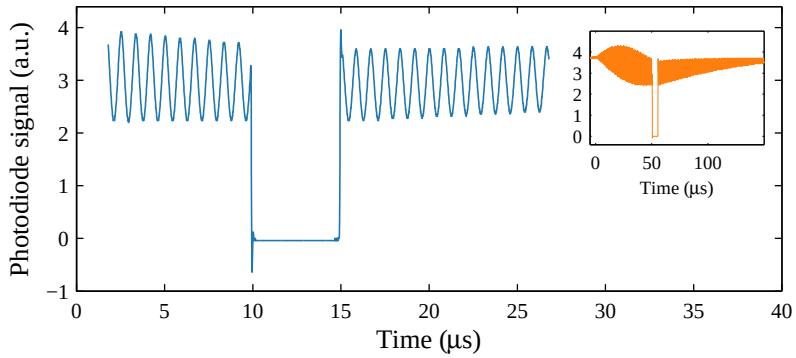

Figure 6.5: Photo-diode beat signal between the optical control field and the coherent generated signal field for a 50 μs long RF pulse and the storage period of 5 μs. The inset shows a photo-diode beat signal for a longer time span.

To allow for a comparison with expected results, numerical simulations of the system are carried out, using time-dependent density matrix calculations. In the simulations, a 6 level system, corresponding to the ground and excited states of the experimentally used $F = 1 \rightarrow F' = 1$ transition, is considered. The time evolution of the density matrix ρ is calculated by using the Liouville equation (2.11) and the system of optical Bloch equations (2.12). The Hamiltonian of the system that is used in the calculations includes interactions with the optical control field, the external DC magnetic field and the RF field (see Eq. A.7). All loss mechanisms, like the dephasing rate G and the population relaxation rate $\gamma \approx 2\pi \times 6$ MHz are introduced in a phenomenological way. For the decoherence rate G of our Rb buffer gas system, the experimental value derived from EIT resonance measurements is used, as in [73]. To mimic the experimentally existing population losses from the excited hyperfine level $5P_{1/2}$ $F' = 1$ to the level $5S_{1/2}$ $F = 2$, one additional element of the density matrix ρ is introduced as a loss level. Therefore, for the six-level system, the density matrix has 37 elements and together with the matrices C and D that contain all coupling and decay coefficients, leads to the Liouville equation of the following form:

$$\frac{\partial \rho}{\partial t} = (C + D)\rho, \tag{6.1}$$

where C and D are 37×37 dimensional matrices. As usual, the diagonal elements of the density matrix give the population of the states, while off-diagonal elements can be used to calculate the complex polarization of the medium [27]. In this case, the matrix elements ρ_{ii} correspond to the occupation number of the states $|i\rangle$ (see Fig. 6.3). To test

the theoretical assumptions, the code is checked by simulating the time evolution of the 6-level system interacting resonantly with the optical field Ω_C, where the total population of the system occupies the ground state $|4\rangle$. The result of solving the Eq. 6.1 for the following initial conditions $\rho_{44}(t = 0) = 1$, and $\Omega_C = 0.1\gamma$ is presented in Fig. 6.6 with the time scale given in units of inverse population relaxation rate γ.

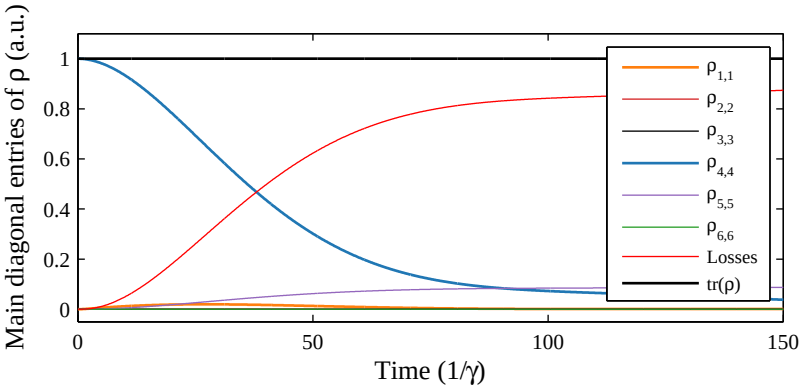

Figure 6.6: Time evolution of the main diagonal elements of the density matrix ρ.

From the time evolution of the matrix element ρ_{44}, one sees that only the part of the entire population of the ground state $|4\rangle$ is pumped to the ground state $|5\rangle$, while the rest of the population is lost. The black solid line in Fig. 6.6 presents the trace of the density matrix ρ and since it includes the lossy channel, it is at all times equal to the total occupation number.

The main goal of this calculations is to simulate the response of the system, interacting simultaneously with the resonant optical and radio-frequency fields. A typical result is shown in Fig. 6.7, for parameters corresponding to the experimental settings.

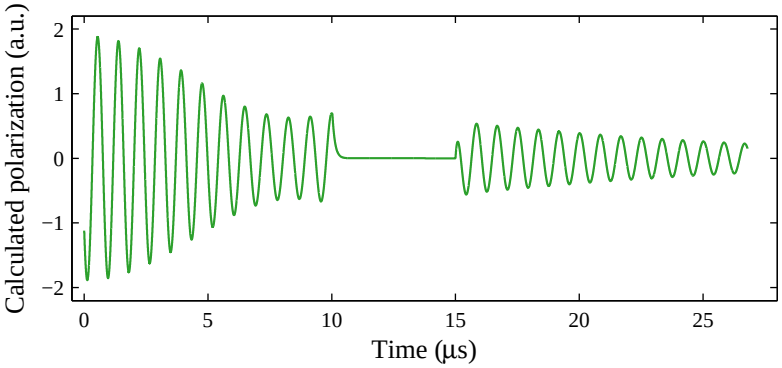

Figure 6.7: Calculated medium polarization on the transition between levels $|F = 1, m_F = 0\rangle \rightarrow |F' = 1, m_F = 1\rangle$ (see Fig. 6.3), where the eigenfrequency is measured with the respect to the control field frequency. Parameters used in the calculation correspond to the estimated experimental parameters ($\Omega_C = 0.02\gamma$, $\Omega_{RF} = 0.0005\gamma$, $g_F\mu_B B \propto 0.033\gamma$, $G = 0.0001\gamma$, where $\gamma \approx 2\pi \times 6$ MHz).

Compared to the experimentally measured beat signal (Fig. 6.5), the beat note coming

from the oscillation of the calculated polarization has a qualitatively similar behavior. For the same storage time of 5 μs, it is determined that the calculated beat frequency of the retrieved coherence quantitatively matches the measured frequency value of the detected beat signal.

In the experiments, the beat signal of control and generated optical signal beam is detected for different values of both the magnetic bias field and the frequency ω_{RF} of the RF coupling. When the magnetic bias field is varied, the frequency of the RF field is kept constant and vice versa. Typical data for the shift in the beat frequency after the resonance retrieval, as a function of the bias field and the frequency ω_{RF} of the RF field is shown by orange dots and blue squares in Fig. 6.8(a). Here, the variable magnetic bias field is expressed in terms of Zeeman splitting of two neighboring ground states. Both parameters are scanned for the same frequency range, and each shown data point represents the averaged value for ten different measurements. These two data sets are fitted by a linear function, showing the linear dependence of the beat frequency on the size of the Zeeman splitting (Fig. 6.8(a) solid orange line) with a slope of 0.999($\pm$0.003). Within the experimental accuracy, the beat frequency between optical control and generated signal fields thus equals the separation $g_F \mu_B B$ of adjacent Zeeman components of the $F = 1$ hyperfine ground state.

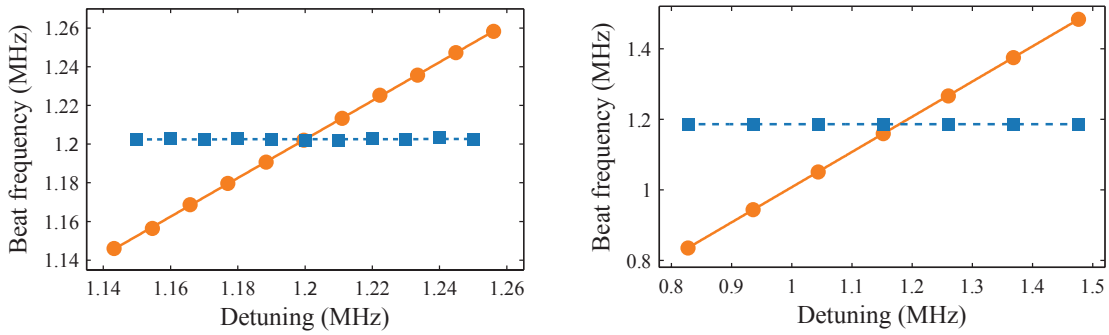

Figure 6.8: (a) Measured beat frequency versus frequency of the radiofrequency field (blue squares) and Zeeman frequency splitting between adjacent Zeeman sublevels (orange dots). When the magnetic bias field is varied the frequency of the RF field is kept constant and vice versa. Each shown data point represents the averaged value of ten measurements. (b) Corresponding calculated results from the numerical simulation.

The data points corresponding to different values of the frequency ω_{RF} of the RF field can be well described by linear behavior (Fig. 6.8(a) blue dashed line) with a slope of 0.002($\pm$0.005) that vanishes within the experimental uncertainty, which is consistent with the assumption that the frequency of the RF coupling does not have a noticeable influence on the value of the retrieved beat frequency. As expected, during the RF excitation, the difference of the detected beat frequency is given by $\omega_S - \omega_C = \omega_{\mathrm{RF}}$ when varying either magnetic bias field or the RF frequency.

Fig. 6.7 shows calculated results for the coherences between the states $|F = 1, m_F = 0\rangle \rightarrow |F' = 1, m_F = 1\rangle$, where the eigenfrequency is measured with respect to the frequency of

the optical control field. The corresponding polarization is responsible for the emission of the signal beam, and the shown oscillation is to serve as a numerical estimation of the expected time-dependence of the experimentally observed beat between signal and control optical fields respectively. Fig 6.8(b) shows the corresponding calculated values of the oscillation frequency of the atomic polarization with respect to the control field frequency, versus the frequency of the RF field (blue squares) and the frequency splitting between adjacent Zeeman sublevels (orange dots). For determination of the corresponding frequency from the numerical values for the polarization, a Fast Fourier transform procedure, implemented in a MATLAB environment, is used. The calculated results are in good agreement with the corresponding experimental observation (Fig. 6.5 and Fig. 6.8(a)). The experimentally measurable beat frequency range is several times smaller than the frequency range acquired by simulations, which is attributed to the experimentally limited detection sensitivity.

The resonance retrieval effect for different storage times of the atomic coherence is also investigated. The green dots in Fig. 6.9 show the measured slope of the observed beat signal upon variation of the Zeeman splitting between adjacent sublevels versus the storage time, and within experimental uncertainties no deviation from the expected value unity is observed. In red, results of the numerically calculated dependence is shown.

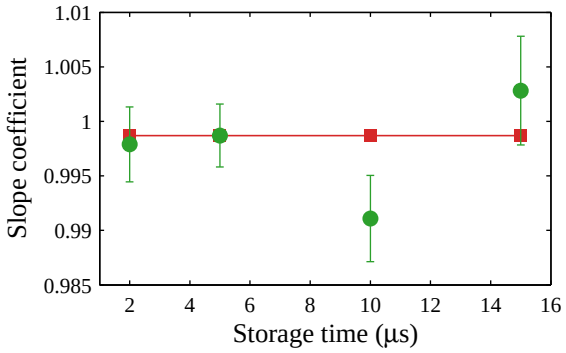

Figure 6.9: Slope of the observed beat frequency upon variation of the Zeeman splitting $g_F \mu_B B$ (green dots) versus the storage time, and corresponding simulated results for the atomic coherence (red squares). The size of the error bars of the simulated data values is within the drawing size of the data points.

Finally, the robustness of the effects is tested by performing measurements for different intensities of the optical control field. Fig. 6.10(a) shows the observed (green dots) slope of the beat frequency upon variation of the Zeeman splitting versus the control field Rabi frequency, and in red, results of a corresponding calculation are shown. For the used parameter range, within experimental uncertainties no frequency shift from the ac Stark shift was observed. Similarly, within experimental uncertainty, no dependence on the retrieved frequency difference is observed when varying the Rabi frequency Ω_{RF} of the RF field up to approximately a level of $\Omega_{\mathrm{RF}}/2\pi = 100$ kHz. However, the simulations for the range of the control field Rabi frequencies, which is experimentally unavailable, show that the beat frequency has quadratic Stark dependence on the Rabi frequency Ω_C of the control field (Fig. 6.10(b)).

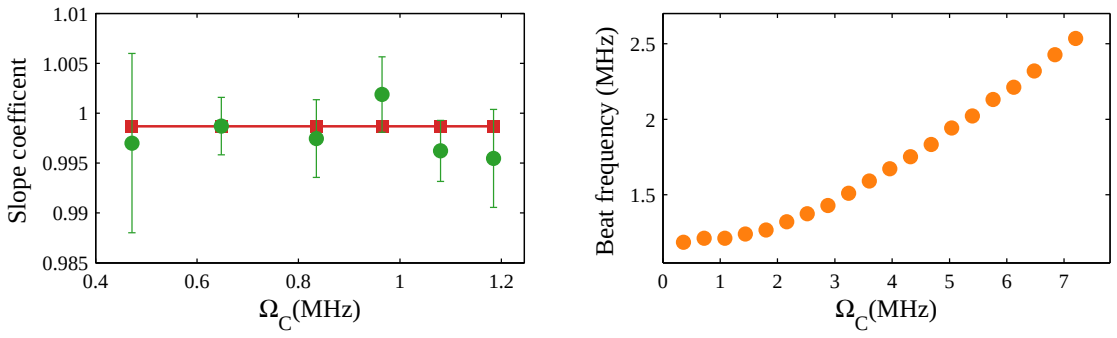

(a) (b)

Figure 6.10: (a) Slope of the observed beat frequency upon variation of the Zeeman splitting $g_F \mu_B B$ (green dots) versus the Rabi frequency of the optical control field Ω_C. (b) Calculated beat frequency for a wide range of the Rabi frequencies Ω_C.

A method of storage and resonance retrieval of the atomic coherence has been presented. The stored atomic coherence is created by RF coupling of the Zeeman ground states and subsequently retrieved with the use of the optical field. Experimental and theoretical investigations reveal that the retrieved signal remains matched to the atomic transition frequency independent of amplitude and frequency variations of the RF field. The experimental uncertainty of the measured atomic eigenfrequency is here limited by a combination of the magnetic bias field coils and the current source, which give the frequency resolution of approximately 1 kHz/mA.

7 Conclusions and Outlook

In this dissertation, quantum coherent effects in a hot rubidium ensemble have been studied. The main result represents the retrieval of stored atomic coherence at the atomic eigenfrequency in a double radiofrequency-optical experiment. Also, the validity of quasi-particle concept of dark state polaritons (DSP) was investigated.

The results from the radiofrequency (RF) spectroscopy of both stationary and moving dark state polartions indicate that a transition between the internal polariton states is possible, which also proves the particle-like nature of the DSP. A two-level dark polariton was prepared in the tripod-linked scheme, realized in the hyperfine configuration in atomic rubidium. The RF field probed the Zeeman sublevels of the hyperfine ground state, allowing for the population transfer between the two internal states. Since the experimentally used Rb hyperfine ground states possess the same g-factor, the RF coupling presumably was partially contributing to a destruction of the dark states. Therefore, for future RF spectroscopic measurements on the DSP, the use of a different atomic system is recommendable. In the tripod configuration one can store two orthogonally polarized light components, making this system potentially applicable as a quantum memory. Obviously, a reliable population transfer between the two tripod dark states could find its application in the quantum information field.

The matter-like nature of the DSP was researched further by studying the behavior of its effective magnetic dipole moment in the presence of the homogeneous electric field. Hence, the existence of the Aharonov-Casher (AC) phase effect for the polariton systems was investigated as well. To this end, a detection system that allows a phase measurement with the sensitivity of 10^{-5} rad was developed. It can be conjectured from the calibration measurements that upper limit of the here experimentally detectable AC phase using hot rubidium gas is 10^{-5} rad.

A resonance retrieval of atomic coherence in an optical-radiofrequency double resonance experiment was demonstrated. The atomic coherence was stored in a thermal vapor of rubidium atoms by an optical control field, and a radiofrequency field. It was shown, both experimentally and theoretically, that after the retrieval of this stored coherence, a beat signal corresponding to the atomic eigenfrequency occurs. This is attributed to the atomic coherence in the absence of driving oscillating at an atomic eigenfrequency, i.e. that only phase (and amplitude), but no frequency information is stored. The detected beat frequency is, within the limits of the experimental uncertainty, insensitive to the amplitude and frequency variations of the driving RF field. It is to be assumed that here presented experimental procedure can be used in measurements of the atomic transition frequencies without precise knowledge of the driving frequencies. The results hold prospects for the development of simple and robust atomic clocks. Prospective applications in atomic magnetometry are also anticipated.

Several technical improvements of the experimental setup could increase the overall sensitivity. An active temperature stabilization of the rubidium apparatus would contribute to the long term stability of the system, which is important for the measurement of the

Aharonov-Casher phase where long averaging time is required. Higher accuracy in the frequency measurements could be achieved with a further improved magnetic shielding, which would reduce influence from stray magnetic fields.

A Derivation of RWA Hamiltonian for the Λ-scheme

To find the Hamiltonian H of the Λ-linked interaction scheme (Fig. 2.1) as given in Eq. 2.1, the Hamiltonian itself has to be transformed from the basis of bare (uncoupled) states into the basis of dressed states. This is achieved by transforming the state vector $|\Psi\rangle$ via rotation operator $\hat{T}$ into the transformed state $|\hat{\Psi}\rangle$, as $|\hat{\Psi}\rangle = \hat{T}\,|\Psi\rangle$. Starting with the Schroedinger equation:

$$i\hbar\partial_t\,|\Psi\rangle = H\,|\Psi\rangle\,, \tag{A.1}$$

and including into it the above the state transformation, the general expression of the transformed Hamiltonian can be found:

$$\hat{H} = \hat{T}H\hat{T}^\dagger - i\hbar\hat{T}(\partial_t\hat{T}^\dagger) \tag{A.2}$$

For the Λ-scheme in Fig. 2.1, the Hamiltonian in the bare-states basis is :

$$H = \hbar\begin{pmatrix} \omega_\mathrm{a} & \Omega_\mathrm{S}\cos\omega_\mathrm{S}t & \Omega_\mathrm{C}\cos\omega_\mathrm{C}t \\ \Omega_\mathrm{S}\cos\omega_\mathrm{S}t & \omega_\mathrm{b} & 0 \\ \Omega_\mathrm{C}\cos\omega_\mathrm{C}t & 0 & \omega_\mathrm{c} \end{pmatrix}, \tag{A.3}$$

while the transformation matrix $\hat{T}$ can be defined as:

$$\hat{T} = \begin{pmatrix} 1 & 0 & 0 \\ 0 & e^{i\omega_\mathrm{S}t} & 0 \\ 0 & 0 & e^{i\omega_\mathrm{S}t} \end{pmatrix}. \tag{A.4}$$

Then, with the use of Eq. A.2, the transformed Hamiltonian is calculated:

$$H = \hbar\begin{pmatrix} \omega_\mathrm{a} & \Omega_\mathrm{S}A_\mathrm{S}^* & \Omega_\mathrm{C}A_\mathrm{C}^* \\ \Omega_\mathrm{S}A_\mathrm{S} & \omega_\mathrm{b}-\omega_\mathrm{S} & 0 \\ \Omega_\mathrm{C}A_\mathrm{C} & 0 & \omega_\mathrm{c}-\omega_\mathrm{C} \end{pmatrix}, \tag{A.5}$$

where $A_\mathrm{S} = \frac{1}{2}e^{i\omega_\mathrm{S}t}\left[e^{-i\omega_\mathrm{S}t} + e^{i\omega_\mathrm{S}t}\right]$, $A_\mathrm{C} = \frac{1}{2}e^{i\omega_\mathrm{C}t}\left[e^{-i\omega_\mathrm{C}t} + e^{i\omega_\mathrm{C}t}\right]$, and the cosine factors $\cos\omega t$ are replaced by $\frac{1}{2}\left(e^{i\omega t} + e^{-i\omega t}\right)$. Applying now the rotating wave approximation (RWA), one neglects the rapidly oscillating terms at $2\omega_\mathrm{S}$ and $2\omega_\mathrm{C}$ since they are far-off resonant. Setting the zero point of the energy to $\hbar\omega_\mathrm{a} = 0$ and introducing the one-photon detunings of the signal and the control field as $\Delta_\mathrm{ab} = \omega_\mathrm{b} - \omega_\mathrm{S}$ and $\Delta_\mathrm{ac} = \omega_\mathrm{c} - \omega_\mathrm{C}$, the Hamiltonian of the Λ-scheme can be defined as:

$$H = \frac{\hbar}{2}\begin{pmatrix} 0 & \Omega_\mathrm{S} & \Omega_\mathrm{C} \\ \Omega_\mathrm{S} & 2\Delta_\mathrm{ab} & 0 \\ \Omega_\mathrm{C} & 0 & 2\Delta_\mathrm{ac} \end{pmatrix}, \tag{A.6}$$

The above approach in finding the Hamiltonian of the atom-light interaction system is used in the calculations performed in this thesis. For example, in chapter 6, a Hamiltonian describing a six-level atomic system interacting with optical and radio-frequency(RF) field

is used and it can be expressed in a following way:

$$H = \frac{\hbar}{2}\begin{pmatrix} 0 & 0 & 0 & -cg_{1,4}\Omega_{\mathrm{C}} & 0 & 0 \\ 0 & \delta & 0 & 0 & 0 & 0 \\ 0 & 0 & 2\delta & 0 & 0 & -cg_{3,6}\Omega_{\mathrm{C}} \\ -cg_{1,4}\Omega_{\mathrm{C}} & 0 & 0 & \Delta + B_{\mathrm{Z}} & -\Omega_{\mathrm{RF}}B^{*} & 0 \\ 0 & 0 & 0 & -\Omega_{\mathrm{RF}}B & \Delta + \delta & -\Omega_{\mathrm{RF}}B^{*} \\ 0 & 0 & -cg_{3,6}\Omega_{\mathrm{C}} & 0 & -\Omega_{\mathrm{RF}}B & 2\delta + \Delta - B_{\mathrm{Z}} \end{pmatrix}, \tag{A.7}$$

where B_{Z} is the size of the Zeeman splitting, Ω_C and Ω_{RF} are the Rabi frequencies of the optical control and RF field. One-photon and two-photon detuning are given by Δ and δ, and $B = \cos\omega_{\mathrm{RF}}t \cdot exp[-i(B_{\mathrm{Z}} + \delta)t]$. Obviously, in the case of RF coupling, the counter-rotating far-off resonance terms cannot be neglected. $cg_{i,j}$ are the dipole matrix elements for specific hyperfine sublevels $|F, m_F\rangle \rightarrow |F', m'_F\rangle$ transitions, which represent the interaction strength between ^{87}Rb and nearly-resonant optical radiation. Here given $cg_{1,4}$ and $cg_{3,6}$ are dipole matrix elements for transitions between the states $|4\rangle \rightarrow |1\rangle$ and $|6\rangle \rightarrow |3\rangle$, as denoted in Fig. 6.3, with values $1/\sqrt{12}$ and $-1/\sqrt{12}$ respectively. A full list of dipole matrix elements for ^{87}Rb D_1 transition can be found in [104].

B Rubidium Spectroscopic Data

This section gives a short list of ^{87}Rb optical properties on D1 line transition (Table B.1) and a scheme of ^{87}Rb D1 transition hyperfine structure with hyperfine splittings (Fig. B.1).

Frequency	$2\pi \cdot 377.107\ 463\ 5(4)$ THz
Wavelength (Vacuum)	794.978 850 9(8) nm
Wavelength (Air)	794.765 69 nm
Wave Number (Vacuum)	12 578.950 985(13) cm^{-1}
Lifetime	27.70(4) ns
Natural Line Width	$2\pi \cdot 5.746(8)$ MHz

Table B.1: ^{87}Rb optical properties on D1 line transition [104].

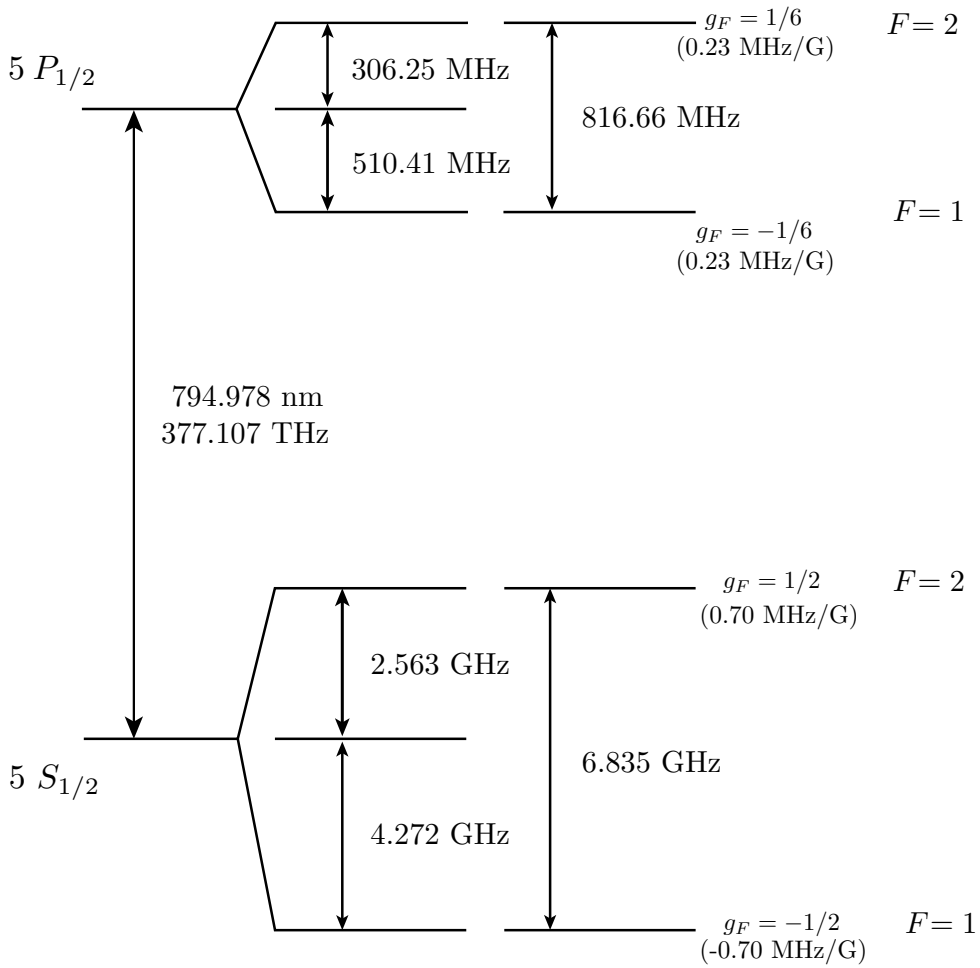

Figure B.1: ^{87}Rb D1 transition hyperfine structure. Scheme adapted from [104].

References

[1] T. H. Maiman, "Stimulated Optical Radiation in Ruby," Nature (London) **187**, 493 (1960).

[2] R. J. Glauber, "The Quantum Theory of Optical Coherence," Phys. Rev. **130**, 2529 (1963).

[3] M. Brune, F. Schmidt-Kaler, A. Maali, J. Dreyer, E. Hagley, J. M. Raimond, and S. Haroche, "Quantum Rabi Oscillation: A Direct Test of Field Quantization in a Cavity," Phys. Rev. Lett. **76**, 1800 (1996).

[4] D. M. Meekhof, C. Monroe, B. E. King, W. M. Itano, and D. J. Wineland, "Generation of Nonclassical Motional States of a Trapped Atom," Phys. Rev. Lett. **76**, 1796 (1996).

[5] T. W. Haensch, S. I. S., and S. A. L., "Optical resolution of the Lamb shift in atomic hydrogen by laser saturation spectroscopy," Nature **235**, 63 (1972).

[6] T. Andreae, W. König, R. Wynands, D. Leibfried, F. Schmidt-Kaler, C. Zimmermann, D. Meschede, and T. W. Haensch, "Absolute frequency measurement of the hydrogen 1 S -2 S transition and a new value of the Rydberg constant," Phys. Rev. Lett. **69**, 1923 (1992).

[7] S. A. Diddams, D. J. Jones, J. Ye, S. T. Cundiff, J. L. Hall, J. K. Ranka, R. S. Windeler, R. Holzwarth, T. Udem, and T. W. Haensch, "Direct Link between Microwave and Optical Frequencies with a 300 THz Femtosecond Laser Comb," Phys. Rev. Lett. **84**, 5102 (2000).

[8] J. G. Bohnet, Z. Chen, J. M. Weiner, D. Meiser, M. J. Holland, and J. K. Thompson, "A steady-state superradiant laser with less than one intracavity photon," Nature (London) **484**, 493 (2012).

[9] S. Chu, L. Hollberg, J. E. Bjorkholm, A. Cable, and A. Ashkin, "Three-dimensional viscous confinement and cooling of atoms by resonance radiation pressure," Phys. Rev. Lett. **55**, 48 (1985).

[10] P. D. Lett, R. N. Watts, C. I. Westbrook, W. D. Phillips, P. L. Gould, and H. J. Metcalf, "Observation of Atoms Laser Cooled below the Doppler Limit," Phys. Rev. Lett. **61**, 169 (1988).

[11] A. Aspect, E. Arimondo, R. Kaiser, N. Vansteenkiste, and C. Cohen-Tannoudji, "Laser Cooling below the One-Photon Recoil Energy by Velocity-Selective Coherent Population Trapping," Phys. Rev. Lett. **61**, 826 (1988).

[12] M. H. Anderson, J. R. Ensher, M. R. Matthews, C. E. Wieman, and E. A. Cornell, "Observation of Bose-Einstein Condensation in a Dilute Atomic Vapor," Science **269**, 198 (1995).

[13] K. B. Davis, M. O. Mewes, M. R. Andrews, N. J. van Druten, D. S. Durfee, D. M. Kurn, and W. Ketterle, "Bose-Einstein Condensation in a Gas of Sodium Atoms," Phys. Rev. Lett. **75**, 3969 (1995).

[14] R. Wynands and S. Weyers, "Atomic fountain clocks," Metrologia **42**, S64 (2005).

[15] L.-A. Wu, H. J. Kimble, J. L. Hall, and H. Wu, "Generation of Squeezed States by Parametric Down Conversion," Phys. Rev. Lett. **57**, 2520 (1986).

[16] P. G. Kwiat, K. Mattle, H. Weinfurter, A. Zeilinger, A. V. Sergienko, and Y. Shih, "New High-Intensity Source of Polarization-Entangled Photon Pairs," Phys. Rev. Lett. **75**, 4337 (1995).

[17] J. Klaers, J. Schmitt, F. Vewinger, and M. Weitz, "Bose-Einstein condensation of photons in an optical microcavity," Nature (London) **468**, 493 (2010).

[18] G. Alzetta, A. Gozzini, L. Moi, and G. Orriols, "An experimental method for the observation of r.f. transitions and laser beat resonances in oriented Na vapour," Il Nuovo Cimento B (1971-1996) **36**, 5 (1976).

[19] S. E. Harris, "Electromagnetically induced transparency," Physics Today **50**, 36 (1997).

[20] K.-J. Boller, A. Imamoğlu, and S. E. Harris, "Observation of electromagnetically induced transparency," Phys. Rev. Lett. **66**, 2593 (1991).

[21] M. M. Kash, V. A. Sautenkov, A. S. Zibrov, L. Hollberg, G. R. Welch, M. D. Lukin, Y. Rostovtsev, E. S. Fry, and M. O. Scully, "Ultraslow Group Velocity and Enhanced Nonlinear Optical Effects in a Coherently Driven Hot Atomic Gas," Phys. Rev. Lett. **82**, 5229 (1999).

[22] S. E. Harris and L. V. Hau, "Nonlinear Optics at Low Light Levels," Phys. Rev. Lett. **82**, 4611 (1999).

[23] M. Weitz, B. C. Young, and S. Chu, "Atomic Interferometer Based on Adiabatic Population Transfer," Phys. Rev. Lett. **73**, 2563 (1994).

[24] S. E. Harris, J. E. Field, and A. Imamoğlu, "Nonlinear optical processes using electromagnetically induced transparency," Phys. Rev. Lett. **64**, 1107 (1990).

[25] L. V. Hau, S. E. Harris, Z. Dutton, and C. H. Behroozi, "Light speed reduction to 17 metres per second in an ultracold atomic gas," Nature (London) **397**, 594 (1999).

[26] L.-M. Duan, M. D. Lukin, J. I. Cirac, and P. Zoller, "Long-distance quantum communication with atomic ensembles and linear optics," Nature (London) **414**, 413 (2001).

[27] M.Fleischhauer, A.Imamoglu, and J. P. Marangos, Rev. Mod.Phys **77**, 633 (2005).

[28] C. Liu, Z. Dutton, C. H. Behroozi, and L. V. Hau, "Observation of coherent optical information storage in an atomic medium using halted light pulses," Nature (London) **409**, 490 (2001).

[29] D. F. Phillips, A. Fleischhauer, A. Mair, R. L. Walsworth, and M. D. Lukin, "Storage of Light in Atomic Vapor," Phys. Rev. Lett. **86**, 783 (2001).

[30] A. Mair, J. Hager, D. F. Phillips, R. L. Walsworth, and M. D. Lukin, "Phase coherence and control of stored photonic information," Phys. Rev. A **65**, 031 802 (2002).

[31] J. Appel, E. Figueroa, D. Korystov, M. Lobino, and A. I. Lvovsky, "Quantum Memory for Squeezed Light," Phys. Rev. Lett. **100**, 093 602 (2008).

[32] M. D. Eisaman, A. Andre, F. Massou, M. Fleischhauer, A. S. Zibrov, and M. D. Lukin, "Electromagnetically induced transparency with tunable single-photon pulses," Nature (London) **438**, 837 (2005).

[33] K. Honda, D. Akamatsu, M. Arikawa, Y. Yokoi, K. Akiba, S. Nagatsuka, T. Tanimura, A. Furusawa, and M. Kozuma, "Storage and Retrieval of a Squeezed Vacuum," Phys. Rev. Lett. **100**, 093 601 (2008).

[34] K. S. Choi, H. Deng, J. Laurat, and H. J. Kimble, "Mapping photonic entanglement into and out of a quantum memory," Nature (London) **452**, 67 (2008).

[35] T. Chaneliere, D. N. Matsukevich, S. D. Jenkins, S.-Y. Lan, T. A. B. Kennedy, and A. Kuzmich, "Storage and retrieval of single photons transmitted between remote quantum memories," Nature (London) **438**, 833 (2005).

[36] F. Vewinger, J. Appel, E. Figueroa, and A. I. Lvovsky, "Adiabatic frequency conversion of optical information in atomic vapor," Opt. Lett. **32**, 2771 (2007).

[37] J. F. Sherson, H. Krauter, R. K. Olsson, B. Julsgaard, K. Hammerer, I. Cirac, and E. S. Polzik, "Quantum teleportation between light and matter," Nature (London) **443**, 557 (2006).

[38] J. Nunn, I. A. Walmsley, M. G. Raymer, K. Surmacz, F. C. Waldermann, Z. Wang, and D. Jaksch, "Mapping broadband single-photon wave packets into an atomic memory," Phys. Rev. A **75**, 011 401 (2007).

[39] A. L. Alexander, J. J. Longdell, M. J. Sellars, and N. B. Manson, "Photon Echoes Produced by Switching Electric Fields," Phys. Rev. Lett. **96**, 043 602 (2006).

[40] J. Nunn, K. Reim, K. C. Lee, V. O. Lorenz, B. J. Sussman, I. A. Walmsley, and D. Jaksch, "Multimode Memories in Atomic Ensembles," Phys. Rev. Lett. **101**, 260 502 (2008).

[41] G. Hétet, M. Hosseini, B. M. Sparkes, D. Oblak, P. K. Lam, and B. C. Buchler, "Photon echoes generated by reversing magnetic field gradients in a rubidium vapor," Opt. Lett. **33**, 2323 (2008).

[42] M. Nilsson and S. Kröll, "Solid state quantum memory using complete absorption and re-emission of photons by tailored and externally controlled inhomogeneous absorption profiles," Optics Communications **247**, 393 (2005).

[43] S. Brandt, A. Nagel, R. Wynands, and D. Meschede, "Buffer-gas-induced linewidth reduction of coherent dark resonances to below 50Hz," Phys. Rev. A **56**, R1063 (1997).

[44] D. Budker, V. Yashchuk, and M. Zolotorev, "Nonlinear Magneto-optic Effects with Ultranarrow Widths," Phys. Rev. Lett. **81**, 5788 (1998).

[45] M. O. Scully and M. Fleischhauer, "High-sensitivity magnetometer based on index-enhanced media," Phys. Rev. Lett. **69**, 1360 (1992).

[46] G. Katsoprinakis, D. Petrosyan, and I. K. Kominis, "High Frequency Atomic Magnetometer by Use of Electromagnetically Induced Transparency," Phys. Rev. Lett. **97**, 230 801 (2006).

[47] V. Shah, S. Knappe, S. D. Jenkins, P. D. D. Schwindt, and J. Kitching, "Subpicotesla atomic magnetometry with a microfabricated vapour cell," Nature Photonics **1**, 649 (2007).

[48] I. K. Kominis, T. W. Kornack, J. C. Allred, and M. V. Romalis, "A subfemtotesla multichannel atomic magnetomete," Nature (London) **422**, 596 (2003).

[49] J. Vanier, "Atomic clocks based on coherent population trapping: a review," Applied Physics B **81**, 421 (2005).

[50] S. Knappe, P. Schwindt, V. Shah, L. Hollberg, J. Kitching, L. Liew, and J. Moreland, "A chip-scale atomic clock based on 87Rb with improved frequency stability," Opt. Express **13**, 1249 (2005).

[51] Z. D. Grujić, P. Koss, G. Bison, and A. Weis, "A sensitive and accurate atomic magnetometer based on free spin precession," The European Physical Journal D **69** (2015).

[52] C. Bolkart, R. Weiss, D. Rostohar, and M. Weitz, "Coherent and BCS-Type Quantum States of Dark Polaritons," Laser Physics **15**, 3 (205).

[53] M. Fleischhauer, J. Otterbach, and R. G. Unanyan, "Bose-Einstein Condensation of Stationary-Light Polaritons," Phys. Rev. Lett. **101**, 163 601 (2008).

[54] R. G. Unanyan, J. Otterbach, M. Fleischhauer, J. Ruseckas, V. Kudriašov, and G. Juzeliūnas, "Spinor Slow-Light and Dirac Particles with Variable Mass," Phys. Rev. Lett. **105**, 173 603 (2010).

[55] J. Ruseckas, V. Kudriašov, G. Juzeliūnas, R. G. Unanyan, J. Otterbach, and M. Fleischhauer, "Photonic-band-gap properties for two-component slow light," Phys. Rev. A **83**, 063 811 (2011).

[56] L. Karpa and M. Weitz, "A Stern-Gerlach experiment for slow light," Nat Phys **2**, 332 (2006).

[57] L. Karpa, F. Vewinger, and M. Weitz, "Resonance Beating of Light Stored Using Atomic Spinor Polaritons," Phys. Rev. Lett. **101**, 170 406 (2008).

[58] E. Arimondo and G. Orriols, "Nonabsorbing atomic coherences by coherent two-photon transitions in a three-level optical pumping," Lettere Al Nuovo Cimento Series 2 **17**, 333 (1976).

[59] M. O. Scully and M. S. Zubairy, *Quantum Optics* (Cambridge University Press, 1997).

[60] C. Cohen-Tannoudji, J. Dupont-Roc, and G. Grynberg, *The Dressed Atom Approach* (Wiley-VCH Verlag GmbH, 2008), p. 407.

[61] M. Fleischhauer and M. D. Lukin, "Dark-State Polaritons in Electromagnetically Induced Transparency," Phys. Rev. Lett. **84**, 5094 (2000).

[62] S. E. Harris, J. E. Field, and A. Kasapi, "Dispersive properties of electromagnetically induced transparency," Phys. Rev. A **46**, R29 (1992).

[63] I. Mazets and B. Matisov, "Adiabatic Raman polariton in a Bose condensate," Journal of Experimental and Theoretical Physics Letters **64**, 515 (1996).

[64] W. Demtröder, "Optical Pumping and Double-Resonance Techniques," in *Laser Spectroscopy* (2008).

[65] L. Karpa, *Quanteneffekte von Dunkelzustandspolaritonen*, Ph.D. thesis, Rheinische Friedrich-Wilhelms-Universität Bonn (2010).

[66] L. Ricci, M. Weidemüller, T. Esslinger, A. Hemmerich, C. Zimmermann, V. Vuletic, W. König, and T. Haensch, "A compact grating-stabilized diode laser system for atomic physics," Optics Communications **117**, 541 (1995).

[67] V. V. Yashchuk, D. Budker, and J. R. Davis, "Laser frequency stabilization using linear magneto-optics," Review of Scientific Instruments **71** (2000).

[68] L. Cacciapuoti, M. de Angelis, M. Fattori, G. Lamporesi, T. Petelski, M. Prevedelli, J. Stuhler, and G. M. Tino, "Analog+digital phase and frequency detector for phase locking of diode lasers," Review of Scientific Instruments **76**, 053 111 (2005).

[69] M. Prevedelli, T. Freegarde, and T. Haensch, "Phase locking of grating-tuned diode lasers," Applied Physics B Lasers and Optics **60**, 3 (1995).

[70] M. Zhu and J. L. Hall, "Stabilization of optical phase/frequency of a laser system: application to a commercial dye laser with an external stabilizer," J. Opt. Soc. Am. B **10**, 802 (1993).

[71] G. Enzian, *Radio-frequency spectroscopy of dark-state polaritons in the rubidium system*, Master's thesis, Rheinische Friedrich-Wilhelms-Universität Bonn (2014).

[72] J. Appel, A. MacRae, and A. I. Lvovsky, "A versatile digital GHz phase lock for external cavity diode lasers," Measurement Science and Technology **20**, 055 302 (2009).

[73] E. Figueroa, F. Vewinger, J. Appel, and A. I. Lvovsky, "Decoherence of electromagnetically induced transparency in atomic vapor," Opt. Lett. **31**, 2625 (2006).

[74] D. Budker, D. F. Kimball, S. M. Rochester, and V. V. Yashchuk, "Nonlinear Magneto-optics and Reduced Group Velocity of Light in Atomic Vapor with Slow Ground State Relaxation," Phys. Rev. Lett. **83**, 1767 (1999).

[75] R. Unanyan, M. Fleischhauer, B. Shore, and K. Bergmann, "Robust creation and phase-sensitive probing of superposition states via stimulated Raman adiabatic passage (STIRAP) with degenerate dark states," Optics Communications **155**, 144 (1998).

[76] R. G. Unanyan, B. W. Shore, and K. Bergmann, "Laser-driven population transfer in four-level atoms: Consequences of non-Abelian geometrical adiabatic phase factors," Phys. Rev. A **59**, 2910 (1999).

[77] J. Martin, B. W. Shore, and K. Bergmann, "Coherent population transfer in multilevel systems with magnetic sublevels. III. Experimental results," Phys. Rev. A **54**, 1556 (1996).

[78] F. Vewinger, M. Heinz, R. Garcia Fernandez, N. V. Vitanov, and K. Bergmann, "Creation and Measurement of a Coherent Superposition of Quantum States," Phys. Rev. Lett. **91**, 213 001 (2003).

[79] D. Petrosyan and Y. P. Malakyan, "Magneto-optical rotation and cross-phase modulation via coherently driven four-level atoms in a tripod configuration," Phys. Rev. A **70**, 023 822 (2004).

[80] S. Rebić, D. Vitali, C. Ottaviani, P. Tombesi, M. Artoni, F. Cataliotti, and R. Corbalán, "Polarization phase gate with a tripod atomic system," Phys. Rev. A **70**, 032 317 (2004).

[81] F. Caruso, *Storing Quantum Information via Atomic Dark Resonances*, Master's thesis, Università degli Studi di Catania, Scuola Superiore di Catania (2005).

[82] M. Fleischhauer and M. D. Lukin, "Quantum memory for photons: Dark-state polaritons," Phys. Rev. A **65**, 022 314 (2002).

[83] N. Vitanov, M. Fleischhauer, B. Shore, and K. Bergmann, "Coherent Manipulation of Atoms Molecules By Sequential Laser Pulses," (Academic Press, 2001), Vol. 46 of Advances In Atomic, Molecular, and Optical Physics, p. 55.

[84] S. Hüwe, *Radiofrequency spectroscopy of dark state polaritons*, Master's thesis, Rheinische Friedrich-Wilhelms-Universität Bonn (2012).

[85] Y. Aharonov and D. Bohm, "Significance of Electromagnetic Potentials in the Quantum Theory," Phys. Rev. **115**, 485 (1959).

[86] Y. Aharonov and A. Casher, "Topological Quantum Effects for Neutral Particles," Phys. Rev. Lett. **53**, 319 (1984).

[87] J. Anandan, "Electromagnetic effects in the quantum interference of dipoles," Physics Letters A **138**, 347 (1989).

[88] R. C. Casella, "Nonlocal phase shifts induced by static electric fields in neutron interferometers when the path-enclosed charge vanishes," Phys. Rev. Lett. **65**, 2217 (1990).

[89] K. Sangster, E. A. Hinds, S. M. Barnett, and E. Riis, "Measurement of the Aharonov-Casher phase in an atomic system," Phys. Rev. Lett. **71**, 3641 (1993).

[90] K. Sangster, E. A. Hinds, S. M. Barnett, E. Riis, and A. G. Sinclair, "Aharonov-Casher phase in an atomic system," Phys. Rev. A **51**, 1776 (1995).

[91] A. Cimmino, G. I. Opat, A. G. Klein, H. Kaiser, S. A. Werner, M. Arif, and R. Clothier, "Observation of the topological Aharonov-Casher phase shift by neutron interferometry," Phys. Rev. Lett. **63**, 380 (1989).

[92] K. Zeiske, G. Zinner, F. Riehle, and J. Helmcke, "Atom interferometry in a static electric field: Measurement of the Aharonov-Casher phase," Applied Physics B **60**, 205 (1995).

[93] A. Görlitz, B. Schuh, and A. Weis, "Measurement of the Aharonov-Casher phase of aligned Rb atoms," Phys. Rev. A **51**, R4305 (1995).

[94] M. König, A. Tschetschetkin, E. M. Hankiewicz, J. Sinova, V. Hock, V. Daumer, M. Schäfer, C. R. Becker, H. Buhmann, and L. W. Molenkamp, "Direct Observation of the Aharonov-Casher Phase," Phys. Rev. Lett. **96**, 076 804 (2006).

[95] F. Nagasawa, J. Takagi, Y. Kunihashi, M. Kohda, and J. Nitta, "Experimental Demonstration of Spin Geometric Phase: Radius Dependence of Time-Reversal Aharonov-Casher Oscillations," Phys. Rev. Lett. **108**, 086 801 (2012).

[96] T. H. Boyer, "Proposed Aharonov-Casher effect: Another example of an Aharonov-Bohm effect arising from a classical lag," Phys. Rev. A **36**, 5083 (1987).

[97] G. Nikoghosyan, "Private Communication," Technische Universität Kaiserslautern (2008).

[98] P. S. Light, F. Benabid, G. J. Pearce, F. Couny, and D. M. Bird, "Electromagnetically induced transparency in acetylene molecules with counterpropagating beams in V and Λ schemes," Applied Physics Letters **94**, 141 103 (2009).

[99] M. Klein, I. Novikova, D. F. Phillips, and R. L. Walsworth, "Slow light in paraffin-coated Rb vapur cells," Journal of Modern Optics **53**, 2583 (2006).

[100] L. Karpa, F. Vewinger, and M. Weitz, "Resonance Beating of Light Stored Using Atomic Spinor Polaritons," Phys. Rev. Lett. **101**, 170 406 (2008).

[101] L. Karpa, G. Nikoghosyan, F. Vewinger, M. Fleischhauer, and M. Weitz, "Frequency Matching in Light-Storage Spectroscopy of Atomic Raman Transitions," Phys. Rev. Lett. **103**, 093 601 (2009).

[102] X.-F. He, P. T. Fisk, and N. B. Manson, "Zeeman quantum beat in nuclear quadrupole resonance probed by Raman heterodyne spectroscopy," Journal of Luminescence **53**, 68 (1992).

[103] M. Oberst, F. Vewinger, and A. I. Lvovsky, "Time-resolved probing of the ground state coherence in rubidium," Opt. Lett. **32**, 1755 (2007).

[104] D. A. Steck, "Rubidium 87 D Line Data," Version **2.1.4**.
http://steck.us/alkalidata/rubidium87numbers.pdf